High-order Harmonic Spectroscopy of Cyclic Organic Molecules

by

Abdullah F. Alharbi

Thesis submitted to the

Faculty of Graduate and Postdoctoral Studies

In partial fulfillment of the requirements

For the Ph.D. degree in

Phyiscs

Department of Physics

Faculty of Science

University of Ottawa

Abstract

Understanding the electronic structure and dynamics of cyclic organic molecules is becoming increasingly the subject of investigations from different perspectives due to their unique chemical and physical properties. Since they are largely involved in the biochemistry of living organisms, studies on this class of compounds are also valuable to understand biologically relevant complex systems. Compared to other techniques, high-order harmonic generation (HHG) has been increasingly considered as a powerful spectroscopic tool with Ångstrom spatial and attosecond temporal resolutions. This thesis demonstrates that high-order harmonic spectroscopy is capable of providing structural and dynamical information on the electronic systems of representative cyclic organic molecules comprising randomly oriented five-membered or six-membered rings.

The first part of this thesis shows that the HHG from these molecules is sensitive to their aromatic character, which results from the de-localized π electrons, and can potentially be a useful qualitative measure of aromaticity. We show that the advantage of utilizing HHG in this direction stems from the result that only π molecular orbitals, associated with aromatcity, are responsible for the HHG emission in aromatic systems.

The capability of HHG to distinguish cyclic isomers is demonstrated in the case of xylene molecules. Supported by numerical calculations, differences in the isomers are attributed to both tunnel ionization and photorecombination, the first and last steps of HHG. These results enable further HHG-based time-resolved studies of the dynamics associated with isomeric effects that these molecules exhibit.

The present work also challenges the well-established prediction that strong field ionization from a molecular orbital is suppressed along nodal planes, where the electron density is zero. In fact, our study shows that considerable tunnel ionization in some cyclic molecules can occur near or along nodal planes. This unusual ionization is reported to have its signature on the quantitative and qualitative dependence of harmonic yield on laser ellipticity.

The high symmetry displayed by the cyclic molecule, 1,4 cyclohexadiene, is shown to leave its imprints on the HHG in the form of structural interferences even if the target is randomly oriented. Two-color HHG from this molecule also indicates that hole dynamics could be involved in the generation process.

A general study on high harmonic spectroscopy of the Cooper minimum in molecules is also reported. The presence of this minimum could affect the interpretation of harmonics spectra in any molecule containing S or Cl atoms. The molecular environment is shown to influence the position of this spectral modulation.

Acknowledgements

First of all, I would like to thank my academic advisor, Prof. Ravi Bhardwaj for generous support and guidance. He always managed to make himself available to provide invaluable input on the analysis of my results, discussion and brilliant tips to improve my writing. I would also like to extend my thanks to Dr. Andrey Boguslavskiy, for help and inspiring discussions. Special thanks to Dr. Michael Wong, my previous colleague in the research group, for support during the beginning of my PhD.

Along the way I have worked with a number of great researchers whom I wish to thank. These include Michael Spanner, A.-T. Le, T. Brabec, I. Lopez-Quintas, J.-P. Brichta, Amit Bagga, A. D. Bandrauk, N. Thiré, B. E. Schmidt and F. Légaré. Many thanks to F. Poitras and A. Laramrée from ALLS labs for their valuable technical assistance. I would like to give special mention to my colleague in the group, Ali Alshehri for the fruitful discussions we had together during our PhD journeys. I also owe thanks to the rest of the group members for productive discussions and for providing a good working atmosphere.

Above all, I praise Allah, the almighty, for providing me this opportunity and granting me the capability to proceed successfully. Most of all my appreciation goes to my parents, Fahhad and Hessah, for their enormous support and care. Words cannot express how grateful I am to my wife Nowayer for her patience and encouragement during my PhD journey. Finally, special thanks to my beloved daughters and son for all my happy moments with you.

List of publications

The following publications are included as chapters in this thesis.

1. **A. F. Alharbi**, A. E. Boguslavskiy, N. Thiré, S. Patchkovskii, B. E. Schmidt, F. Légaré, T. Brabec, V. R. Bhardwaj and M. Spanner, Sensitivity of high-order-harmonic generation to aromaticity, Physical Review A, 92, 041801 (2015).

2. M. C. H. Wong, A.-T. Le, **A. F. Alharbi**, A. E. Boguslavskiy, R. R. Lucchese, J.-P. Brichta, C. D. Lin, and V. R. Bhardwaj, *High Harmonic Spectroscopy of the Cooper Minimum in Molecules*, Physical Review Letters, 110, 033006 (2013).

3. **A. F. Alharbi**, A. E. Boguslavskiy, N. Thiré, G. S. Thekkadath, S. Patchkovskii, B. E. Schmidt, F. Légaré, T. Brabec, V. R. Bhardwaj and M. Spanner, *Effects of nodal planes on strong-field ionization and high-harmonic generation in ring-type molecules*, submitted to Physical Review Letters.

   The following publication is not included in this thesis

4. R. Cireasa, A. E. Boguslavskiy, B. Pons, M. C. H. Wong, D. Descamps, S. Petit, H. Ruf, N. Thiré, A. Ferré, J. Suarez, J. Higuet, B. E. Schmidt, **A. F. Alharbi**, F. Légaré, V. Blanchet, B. Fabre, S. Patchkovskii, O. Smirnova, Y. Mairesse and V. R. Bhardwaj, *Probing molecular chirality on a sub-femtosecond timescale*, Nature Physics, 11,654658 (2015).

Table of Contents

List of Figures

List of Abbreviations and Symbols

Abbreviations

ADK	Ionization model, developed by Ammosov, Delone and Krainov
ASE	Aromatic stabilization energy
BBO	Beta barium borate crystal
CHD	Cyclohexadiene molecule
CM	Cooper minimum
GAMESS	The General Atomic and molecular electronic structure system
HHG	High-order harmonic generation
HOMA	Harmonic oscillator model of aromaticity
HOMO	Highest occupied molecular orbital
LCAO	linear combination of atomic orbitals
LIED	Laser-induced electron diffraction
MAE	Active multiple electrons
MCP	Microchannel plate
MO-ADK	ADK-based model to calculate ionization from molecules
MPI	Multiphoton ionization
NICS	Nucleus independent chemical shift
NSDI	Non-sequential double ionization
PICS	Photoionization cross section
SAE	Single active electron approximation
SFA	Strong field approximation
SFI	Strong field ionization
TD-RIS	time-dependent resolution in ionic states method
TDDFT	Time-dependent density functional theory
TDSE	The time-dependent Schrödinger equation
TOF	Time of flight
XUV	Extreme ultra-violet radiation

Mathematical Symbols

χ_G	Diamagnetic susceptibility measure of aromaticity
$\Delta\varphi$	The initial phase difference between two ionizing channels
ϵ	Laser field ellipticity
Γ	Instantaneous ionization rate
γ	Keldysh parameter
$\hbar$	Planck constant divided by 2π
λ	Laser wavelength
$\mathbf{A}$	Vector potential
$\mathbf{d}$	Dipole transition matrix element
$\mathbf{E}$	Electric field
$\mathbf{p}_\perp$	Transverse momentum
$\mathbf{p}_c$	Canonical momentum
$\mathcal{A}$	Fourier transform of the integrated HHG dipole acceleration
Φ	The phase between the two waves
π	A molecular orbital formed by atomic orbitals (often p atomic orbitals)
ψ	Schrödinger wave function
ρ	Gas density
σ	A molecular orbital formed by atomic orbitals (often s atomic orbitals)
σ	Photo-recombination cross-section
$\tilde{S}_N^{(i)}$	The intensity of the N^{th}-order harmonic from two ionizing channel in two-colour HHG
a_0	Bohr radius
$a_{ion}(t)$	Probability amplitude for ionization
$a_{pr}(t)$	Probability amplitude for propagation
$a_{rec}(t)$	Probability amplitude for recombination
E_0	Electric field amplitude
E_k	Eigenvalues corresponding to the energies of the k^{th} π orbital
E_{sat}	Saturation pulse energy for ionizaton
$G_N^{(i)}$	The two-colour gate
$I(t)$	Laser intensity
I_p	Ionization potential
I_{sat}	Saturation intensity for ionizaton
k	The wave vector
L_{abs}	absorption length

L_{coh}	Coherence length
L_{med}	medium length
m_e	Electron mass
N	Number of neutral atoms
n	Refractive index
P	Gas pressure
q	high harmonic order (chapter 2)
q	ion charge (chapter 3 and 5)
R_j	Molecular bond length
R_{opt}	Optimal molecular bond length
S	Classical action
S_N	The intensity of the N^{th}-order harmonic from two ionizing channel in one-colour HHG
U_p	Ponderomotive energy
$Y(\epsilon)$	Harmonic yield dependence on laser ellipticity

Chapter 1

Introduction

1.1 Overview

Organic molecules with cyclic structures play an exceptionally key role in various areas of contemporary science and technology. Their structural units are present in many biochemical substances which are essential to life. They are also known to be building blocks for numerous agrochemical and pharmaceutical compounds and new materials in several growing applications including conducting polymers. Many of these ring-type molecules are aromatic, and therefore have unique chemical and physical properties. For example, aromatic five-membered and six-membered ring molecules are all planar resulting in global symmetry features in highest orbitals such as nodal planes that extend along and perpendicular to the whole ring structure. The aromatic character of these compounds can be quantified. However, approaches towards this quantification are still far from being conclusive. Because of the cyclic structure, the number of cyclic molecules is large. Many of

them share the same atomic structure leading to the existence of unique classes of molecular isomers. Identifying some of these isomers is a challenging task due to the fact that they are connected to the same type of ring that dominates the molecular physical and chemical properties. Besides its applied uses, distinction of isomers is a primary requirement for further time-resolved studies of some interesting light-induced interactions in cyclic isomers.

Our main source of information about atoms and molecules comes primarily from their interaction with radiation. This great tool of knowledge known as spectroscopy was central to the early developments of quantum mechanics, the laws governing atomic and molecular systems. For example, the spectroscopic discoveries of black body radiation and emission lines were used by Max Planck and Niels Bohr as cornerstones to propose the quantization of radiation and atomic energies. Since the first working laser was reported in 1960, spectroscopy has evolved exponentially. Further developments especially in pulsed laser technology have offered new spectroscopic methods to expand our knowledge of matter.

High-order harmonics are a unique light source that can be produced by exposing atoms and molecules to intense femtosecond laser pulses. The underlying physics for the generation process enables these harmonics to provide structural and dynamical information on the generating target with high spatial and temporal resolutions. The spectroscopic capability of high-order harmonic generation (HHG) has been demonstrated intensively in atoms and small molecules [1][2][3]. Moreover, recently there has been a growing interest in extending this tool to polyatomic molecules [4][5]. This thesis brings the important class of cyclic organic molecules to the focus of HHG studies to gain further understanding of

their molecular and electronic structures and dynamics.

1.2 Outline of the thesis

Chapter 2 presents an overview of strong laser field interaction with molecules with an emphasis on high-order harmonic generation. Experimental setup and techniques are covered in Chapter 3. The key question that underlies Chapter 4 is as follows: What is the connection between high-order harmonic generation and the aromatic nature of cyclic molecules? We examine the effect of this relation on the harmonic yield. A major task of spectroscopy is to utilize information obtained by light spectra to distinguish between different emitters. Chapter 5 focuses on how harmonic generation could be different from one cyclic isomer to another. Our target for this study is xylene molecules which are known to be difficult to identify using many spectroscopic techniques. In Chapter 6, we turn our attention to the effect of the electronic and geometric structure of aromatic molecules on the high harmonics dependence on laser ellipticity. The observed results are shown to be due to enhanced ionization along nodal planes, in sharp contrast with what is expected from the current understanding of ionization suppression along these planes. Cyclohexadiene molecules are the subject of Chapter 7 where signatures of molecular structure and dynamics are shown to be imprinted in the HHG process. We also discuss in Appendix A how the presence of Cooper minimum alters the harmonic signal from molecules in general and how this could vary depending on the structure of the molecular system.

1.3 Author contribution

All work presented here resulted from the author's efforts under supervision of V. R. Bhardwaj, and collaborative work from several researchers. In the following, detailed information is provided on the contributions of each participant in the five research projects whose results are outlined in this thesis.

High-harmonic generation experiments were conducted at the Advanced Laser Light Source at INRS EMT, Varennes, QC. This advanced laser system was run and maintained mainly by N. Thiré, B. E. Schmidt and F. Légaré. Photoinization experiments were carried out at the University of Ottawa.

Chapter 4: A. F. Alharbi and A. E. Boguslavskiy, a former post doctoral fellow in the group, performed the experiments at ALLS. A. F. Alharbi conducted the analysis of the experimental results. Ionization calculations were performed by M. Spanner from National Research Council, Ottawa. The results of this study were reported in publication #1. A. F. Alharbi wrote the first draft of the manuscript. All authors contributed to the final manuscript.

Chapter 5: The photoionization experiments were performed by A. F. Alharbi. I. Lopez-Quintas, a visiting graduate student from Spanish National Research Council Madrid, Spain, participated in the final phase of the experiments. A. F. Alharbi and A. E. Boguslavskiy performed the HHG experiments at ALLS. A. F. Alharbi conducted the analysis of the experimental results. Numerical calculations were performed by A.-T. Le from Kansas State University, Manhattan, Kansas. The manuscript containing these results is under preparation.

Chapter 6: A. F. Alharbi, A. E. Boguslavskiy and N. Thiré performed the experiments at ALLS. A. F. Alharbi conducted the analysis of the experimental results and performed the calculations for argon. Calculations for molecular systems were performed by M. Spanner from National Research Council, Ottawa. The results of this study were submitted for publication (publication #3). A. F. Alharbi and M. Spanner wrote the first draft of the manuscript. All authors contributed to the final submitted manuscript.

Chapter 7: All experiments reported in this chapter were performed by A. F. Alharbi and A. E. Boguslavskiy at ALLS. M. C. H. Wong, B. E. Schmidt and I. Lopez-Quintas participated in some experimental parts. A. F. Alharbi performed the two-center interference calculations. A. F. Alharbi and A. E. Boguslavskiy conducted the analysis of the experimental results. Ionization calculations were performed by E. F. Penka and A. D. Bandrauk from Université de Sherbrooke. The manuscript containing these results is under preparation.

Appendix: M. C. H. Wong and J.-P. Brichta performed the experiments at ALLS. A. F. Alharbi generated the Mulliken atomic populations for the molecules studied. M. C. H. Wong analysed the experimental data. The results of this study were reported in publication #2 where the contributions to the final manuscript (except for parts related to the theoretical calculations of harmonic spectra) came from M. C. H. Wong, A. F. Alharbi, A. E. Boguslavskiy, and V. R. Bhardwaj.

Chapter 2

Background

The main goal of this chapter is to provide background information on the interaction of intense laser fields with molecules. For simplicity, the chapter first starts with an overview of the influence of strong fields on atoms, the building blocks of molecules. A significant attention in this introductory material is devoted to high-order harmonic generation. There are several basic aspects that need to be considered when the target in the interaction volume becomes a molecular system. Such modifications are discussed in the second part of this chapter.

2.1 Atoms in a strong laser field

2.1.1 Mechanisms of strong laser field ionization

Einstein's explanation of the photoelectric effect shows that atoms and molecules can be ionized if the photon energy of the incident radiation matches or exceeds the ionization

potential of the target I_p (single photon ionization). Subsequent studies showed that a high enough flux of lower-frequency radiation could also lead to ionization if multiple photons are deposited in the system as depicted in Fig. 2.1a. However, the probability of this multi-photon ionization (MPI) process becomes smaller when the number of absorbed photons n, required for ionization, increases. This probability scales with laser intensity I as follows:

$$\Gamma_n = \sigma_n I^n \quad , \tag{2.1}$$

where σ_n is the n-photon ionization cross section and decreases rapidly with increasing n. For most atomic and molecular species, MPI is a major ionizing channel at light intensities ranging from 10^{12} W/cm^2 to 10^{14} W/cm^2 with conventional 800 nm light. Such intensities can be achieved by focusing short laser pulses. MPI associated with relatively low laser intensities can be described well by equation 2.1 and considered as a perturbative process. For quite higher laser intensities, MPI is non-perturbative since the field is high enough to induce Stark shift to the electronic states. This dynamical effect is more pronounced for higher energy states leading to a shift of the continuum states; hence the effective ionization threshold.

When the laser electric field E is comparable to the binding force of outer electrons ($\sim 10^{11}$ V/m) and the frequency is rather low, another ionization channel becomes probable. Fig. 2.1b shows how the combination of a strong linearly polarised field and the atomic Coulomb potential creates a potential barrier where the bound electron can penetrate. This tunnelling ionization process could occur every half-laser cycle. Therefore the lower the laser frequency, where the tunnel survives for a longer time, the higher the tunnelling

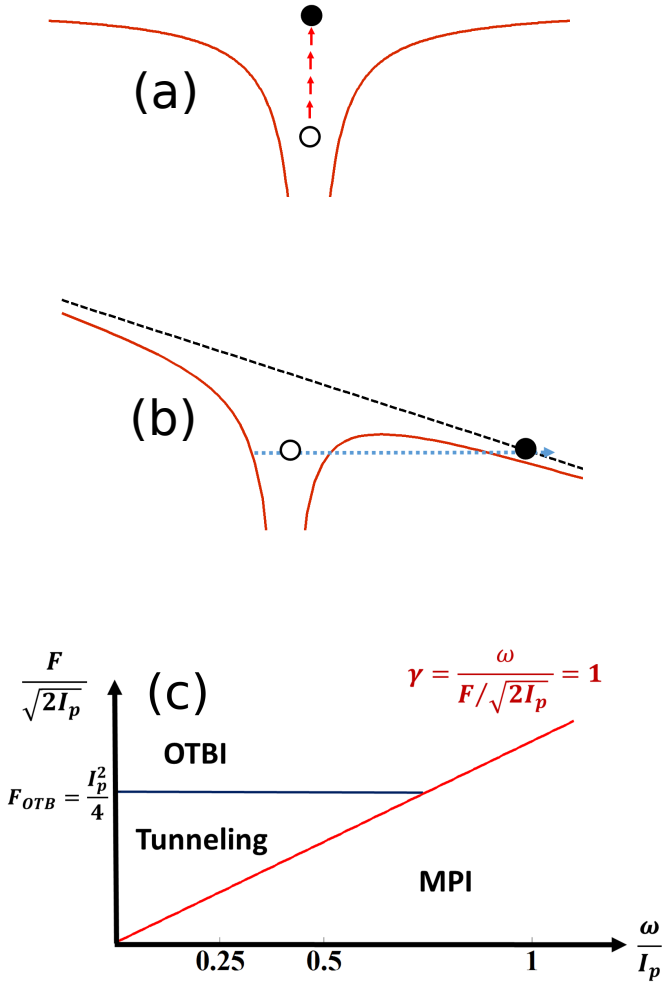

Figure 2.1: a) Multi-photon ionization (MPI). b) The tunnelling of the electron wavefunction under the influence of a strong laser field. c) Basic ionization mechanisms in light of Keldysh parameter γ; MPI, tunnel ionization and over the barrier ionization (OTBI). I and ω are laser intensity and frequency respectively, and I_p is the ionization potential of the target (From [6]).

probability. Ionization by tunnelling is also more probable when the potential barrier is lowered more by applying a higher laser intensity or having a target with a lower I_p. In 1963, Keldysh introduced a dimensionless parameter γ [7] to summarize these facts and categorize the two ionization regimes. Using atomic units ($\hbar = e = m_e = a_0 = 1$, where a_0 is the Bohr radius), this parameter can be expressed as:

$$\gamma = \text{tunneling time}/\frac{1}{2}\,\text{optical period} = \omega\sqrt{2I_p/I} = \sqrt{I_p/2U_p} \quad , \tag{2.2}$$

where ω is the laser frequency and $U_p = E^2/4\omega^2$ is the ponderomotive energy defined as the cycle averaged energy obtained by a free electron in an electromagnetic field. This energy is an important quantity in strong laser physics and commonly expressed in electron Volts as

$$U_p(eV) = 9.33 \times 10^{-14}\, I(W/cm^2)\, \lambda^2(\mu m) \quad , \tag{2.3}$$

Tunnelling ionization occurs when $\gamma << 1$ while MPI occurs for $\gamma >> 1$. The intermediate region features a competition between the two processes with no sharp transition. Fig. 2.1c outlines schematically the basic photoionization domains as a function of electric field and photon energy. This figure also shows the limiting process of tunnelling ionization referred to as over the barrier ionization OTBI (barrier-suppression ionization) [8] where the intensity becomes high enough to completely suppress the Coulomb potential ($I_{OTBI} = I_p^4/16$), therefore the ionization probability becomes one.

It is necessary to exploit laser pulses with a sufficiently short time duration (on the order of tens of femtoseconds) to observe tunnelling ionization. Otherwise the atomic or

molecular target could be depleted by the rising edge of the long pulse before experiencing the peak intensity of the oscillating electric field.

2.1.2 Characteristics of tunnel ionization

2.1.2.1 Tunnelling rate

ADK model, developed by Ammosov, Delone and Krainov [9], is commonly used to calculate tunnelling ionization rates from atoms and atomic ions as a function of laser and atomic parameters. In atomic units, the ADK rate is expressed in the following form:

$$w_{ADK} = |C_{n^*l^*}|^2 G_{lm} I_p (2F_0/E)^{2n^*-|m|-1} e^{(2F_0/3E)} \quad , \tag{2.4}$$

where $F_0 = (2I_p)^{3/2}$ and the two coefficients $C_{n^*l^*}$ and G_{lm} are atomic parameters that depend on the quantum numbers l and m and effective quantum numbers $n^* = Z/\sqrt{(2I_p)}$ and $l^* = n^* - 1$, where Z is the ion charge. The fraction of ionized atoms can be calculated from:

$$\eta = N(1 - e^{-\int_{-\infty}^{t} w_{ADK}(t')dt'}) \quad , \tag{2.5}$$

where N is the number of neutral atoms in the medium.

2.1.2.2 Electron momentum

At the tunnelling exit, the wavefunction of the tunnelled electron occupies a finite width in space. As a quantum object, the wavefunction consequently has a finite momentum distribution. In other words, we can describe the tunnelling process as a partial transfer

of the electron population from the ground state to a certain superposition of momentum eigenstates in the continuum. As discussed in the following section, the liberated electron can make its way back to the parent ion. Thus, the distribution of transverse momentum of the tunnelled electron is more relevant to subsequent strong field processes and can be expressed for simple systems as [10]:

$$\Psi(p_\perp) = \Psi(p_\perp = 0)e^{-p_\perp^2\sqrt{2I_p}/E} \quad , \tag{2.6}$$

where $p_\perp$ is the initial transverse momentum of the electron.

2.1.3 Following the electron after tunnel ionization

Tunnelling is a highly significant process since it acts as the doorway to several interesting phenomena in strong field laser physics. In addition to directly ionized electrons, there is a portion of electrons that can travel back to the parent ion when the oscillating field changes sign. The dynamics of these electrons can essentially be captured by a classical model introduced by Corkum in 1993[11]. In this treatment known as the three-step model, the effect of the Coulomb potential is neglected. Therefore, the motion of the electron in an oscillating electric field ($E = E_0\cos(\omega t)$), where E_0 is the amplitude of the field, is governed by the following equations:

$$\begin{aligned} \ddot{x} &= -E_0\cos(\omega t) \\ \dot{x} &= (E_0/\omega)\left(\sin(\omega t) - \sin(\omega t_i)\right) \\ x &= -(E_0/\omega^2)\left(\cos(\omega t) - \cos(\omega t_i)\right) - E_0/\omega\sin(\omega t_i)(t - ti) \quad . \end{aligned} \tag{2.7}$$

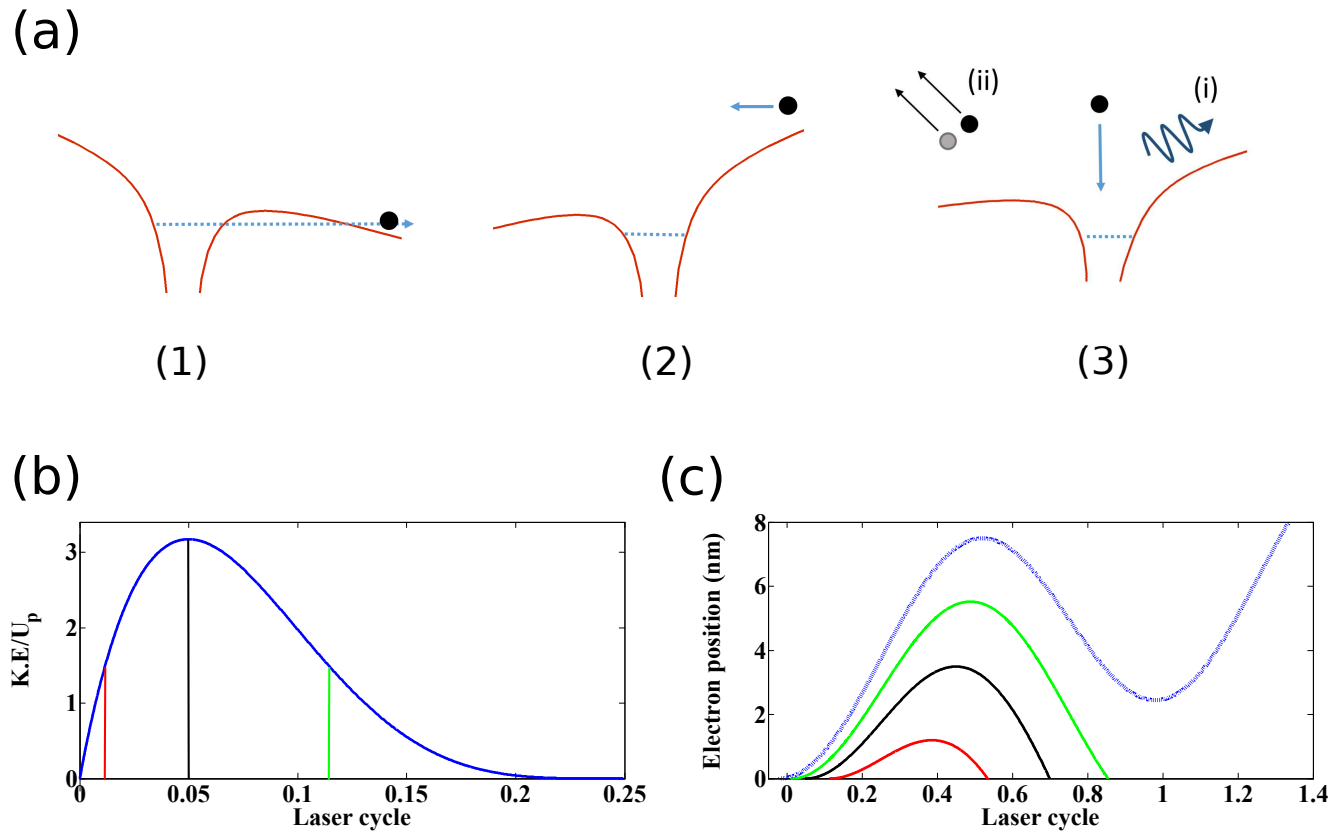

Figure 2.2: a) Examples of three-step (1-tunnelling 2-propagation and 3-recollision) processes that can occur upon electron recollision: i) recombination resulting in the emission of XUV light ii) inelastic scattering leading to non-sequential double ionization. b) The Kinetic energy of the electron upon return (in units of ponderomotive energy) as a function of the phase at ionization expressed in a fraction of laser cycle. c)Classical electronic trajectories as a function of laser cycle at 1800 nm and intensity of $5{\times}10^{13}$ W/cm^2. Recollision is possible when the path intersects with the x-axis. In both figures, the most energetic trajectory (black) and both trajectories short (red) and long (green) leading to the same kinetic energy (1.5 U_p) are shown. The blue curve in (c) indicates a path that never leads to recollision since it corresponds to an electron released before field maximum

.

In these equations, the motion starts at time t_i from $x = 0$, the centre of the atom, with zero initial velocity. The kinetic energy of the electron is given by:

$$K.E = 2\,U_p\,(\sin(\omega t_r + \omega t_i) - \sin(\omega t_i)))^2 \quad . \tag{2.8}$$

The electron re-encounters the parent ion when $x(t_r) \approx 0$, where t_r is the time of return. Under this condition, eq. 2.8 can be solved numerically for $t = t_r$. Upon recollision, several interesting processes can be initiated. For example;

1. High-order harmonic generation (HHG) [12] [11]: the ionized electron recombines with its parent ion leading to the emission of a photon with an energy equal to the ionization potential plus the electron kinetic energy at the time of recombination.

2. Non-sequential double ionization (NSDI) [11] The freed electron inelastically recollides with a second bound electron. The rescattering event results in an instantaneous ionization of both electrons. For this to occur, the kinetic energy of the recolliding electron must exceed the second ionization of the parent ion. If the electron kinetic energy is less, then there is a possibility that the ion is excited by the first electron recollision. In this case, the ionization of the second electron becomes easier later in the pulse since the I_p is lower.

3. Laser-induced electron diffraction (LIED) [13][14]: the returning electron may scatter off the parent ion elastically. The information obtained from this process can be used to image the ion structure with unprecedented time-resolution compared to conventional diffraction techniques.

The first two processes are schematically sketched in Fig. 2.2a. They occur within one laser cycle in three steps: 1) tunnel ionization, 2) propagation in the continuum, and 3) recollision. Fig. 2.2b shows the electron kinetic energy at the time of recollision as a function of the laser phase at which it is released. Only electrons ionized between t_i=0

(field maximum) and t_i=0.25T_0 will re-encounter the parent ion, where T_0 is the laser period. The maximum energy is equal to $E(t_f) = 3.17U_p$ and occurs when the electron is ionized at t_i=0.05T_0. This process repeats itself every half cycle. There are two types of trajectories that the electron can follow starting from two different phases and ending with the same energy. These are called long and short trajectories. Fig. 2.2c shows the paths of these two trajectories corresponding to a final kinetic energy of 1.5 U_p: short (red) and long (green). Electrons following short (long) trajectory are released later (earlier) in time and return earlier (later) in time. This figure also shows the paths for i) an electron with the maximum kinetic energy that returns at t_i=0.7T_0, and ii) an electron that never returns back to origin because it is born before the field maximum.

2.1.4 High-order harmonic generation

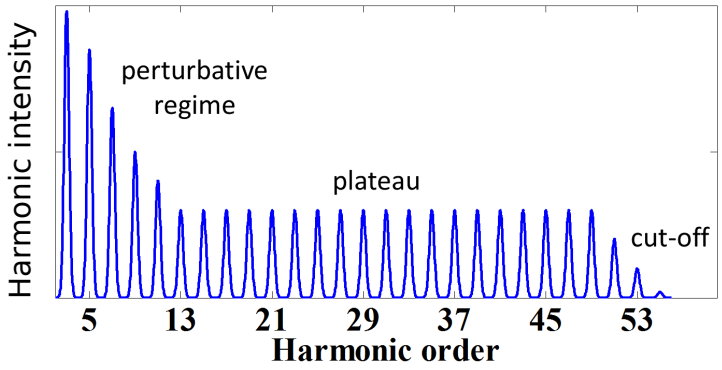

Figure 2.3: A typical spectrum of HHG. The three distinct regions of the spectrum are labelled.

HHG has acquired its vital importance because: i) it provides a coherent light source at the extreme ultraviolet (XUV) and soft X-ray range. ii) the generation process itself serves as a probe of fundamental atomic and molecular processes on Ångstrom spatial-scale with sub-femtosecond time-scale resolution. A typical HHG spectrum is shown in

Fig. 2.3. We can observe two main features from this spectrum. First, the spectrum has three distinct regions. The intensity of the first few harmonics decreases drastically with the harmonic order as expected for a perturbative process. However, the plateau harmonics have similar intensity. This trend stops at the cut-off region where the radiation intensity decreases rapidly until the spectrum ends. Immediately after the first observation of the HHG emission in 1987 by McPherson *et al.* [12] and driven essentially by the astonishing behaviour of the plateau harmonics, the community of strong field laser was looking for an explanation for this process beyond any perturbative treatment. The three-step model described earlier was successful in explaining some of the basic features of the process. A major achievement of this basic model is the prediction of the energy of the harmonic cutoff (the highest frequency produced), emitted by the electron with maximum return energy (Fig. 2.2), to be:

$$E_{cutoff} = I_p + 3.17U_p \tag{2.9}$$

Another feature of the harmonic spectrum is that it contains only odd multiples of the fundamental frequency. This observation can be attributed to the symmetry inversion of the gas medium and the half-cycle symmetry of the field. The harmonic signal generated during a half laser cycle $\mathcal{S}_T(t)$ may be written in the time domain as:

$$\mathcal{S}_T(t) = \begin{cases} \mathcal{S}(t) & 0 < t < \frac{T_0}{2} \\ \mathcal{S}(t - T/2)e^{i\pi} & \frac{T_0}{2} < t < T_0 \end{cases} . \tag{2.10}$$

The phase term is added to account for the sign change in the emission. The Fourier

transform of this expression is given by:

$$A_n(\omega) = \int_0^{T_0} \mathcal{S}_T(t) e^{-in\omega t} dt = \begin{cases} 0 & \omega \text{ even} \\ 2\int_0^{\frac{T_0}{2}} \mathcal{S}_T(t) e^{-in\omega t} dt & \omega \text{ odd} \end{cases} . \tag{2.11}$$

Although it provides an intuitive description of HHG, the three-step model cannot reproduce the HHG spectra or predict the wavelength scaling of the HHG yield for example. A more rigorous picture based on the time-dependent Schrödinger equation (TDSE) is, therefore, required.

2.1.4.1 Quantum mechanical description of HHG

The TSDE for an electron in potential $V(\mathbf{r})$ and experiencing a strong laser field $\mathbf{E}(t)$ can be written under the electric dipole approximation in atomic units as:

$$\frac{\partial}{\partial t} |\psi(\mathbf{r}, t)\rangle = [-\Delta^2/2 + V(\mathbf{r}) - \mathbf{E}(t).\mathbf{r}] |\psi(\mathbf{r}, t)\rangle \quad . \tag{2.12}$$

In this equation, only single electron wavefunction is considered and no electron correlations are involved (single active electron approximation SAE). In principle, a complete solution of equation 2.12 can be achieved numerically. However, this requires large computational capacities which might not be accessible for big systems. Thus, there are several practical limitations on adopting this approach. Alternatively, a further series of assumptions and approximations are made to make the problem computationally more achievable and physically more understandable. In 1994, Lewenstein *et al.* [15] introduced a quantum-mechanical-based model to treat the HHG process from an atomic system under

the following approximations:

1. **Strong field approximation (SFA):** After tunnelling, the electron is subject only to the influence of the strong laser field.

2. **The presence of any bound state other than the ground state is ignored:** In other words, there are no internal resonances.

3. **No depletion of the ground state:** This is true for laser intensities below saturation intensity that lead to full ionization of atoms in the focal volume.

In this model, the first step of the HHG process can be viewed as a portion of the bound wavefunction in the ground state being pulled away from the potential by the strong laser field. Due to the SFA approximation, the liberated electron wavefunction in the continuum is represented by a plane wave with momentum $\mathbf{p}$. On the other hand, the recombination step is nothing but an interference between the freed and the bound portions of the wavefunction. The time-dependent dipole moment of this interference is responsible for the HHG emission and can be obtained analytically by the following integral:

$$\begin{aligned}\langle \mathbf{p}| \, x(t) \, |\psi(\mathbf{r},t)\rangle &= i \int_0^\infty d\tau \int_0^\infty d^3\mathbf{p}_c \, \mathbf{E}(t-\tau)\mathbf{d}(\mathbf{p}-\mathbf{A}(t-\tau) \times e^{(iS(\mathbf{p}_c,t,\tau))} \, \mathbf{d}^*(\mathbf{p}_c-\mathbf{A}(t)) + c.c \\ &\approx i \int_0^\infty a_{ion}(t,\tau) \, a_{prop}(t,\tau,\mathbf{p}_c) \, a_{recom}(t,\mathbf{p}_c) d\tau + c.c \quad .\end{aligned} \tag{2.13}$$

Here τ is the excursion time, $\mathbf{A}(t) = -\int_{-\infty}^{t} \mathbf{E}(t) \, dt$ is the vector potential of the laser field, $\mathbf{p}_c = \mathbf{p} + \mathbf{A}(t)$ is the canonical momentum, $\mathbf{d}$ is the atomic dipole matrix element

between the bound state and the continuum state and S is the semiclassical action of the freed electron. The above expression shows that the dipole moment can be expanded as a product of three factors in the integrand $a_{ion}(t,\tau)$, $a_{prop}(t,\tau)$ and $a_{recom}(t,\tau)$ recovering the three steps in Corkum's model; tunnel ionization, propagation and recombination respectively. The spectrum of the emitted high harmonics can be obtained by a Fourier transform of the second derivative of the dipole:

$$I(\omega) \propto \left| \int \frac{\partial^2 \langle \mathbf{p}| \, x(t) \, |\psi(\mathbf{r},t)\rangle}{\partial t^2} e^{i\omega t} dt \right|^2 \quad . \tag{2.14}$$

2.1.4.2 HHG in orthogonally polarized fields

2.1.4.2.1 Elliptically polarized field

Consider the harmonic generation process in elliptically polarized field given by:

$$\mathbf{E}(t) = \frac{E_0}{\sqrt{1+\epsilon^2}} (cos(\omega t) e_x + \epsilon \, sin(\omega t) e_y) \quad , \tag{2.15}$$

where e_x and e_y are the unit vectors perpendicular to the laser field propagation and ϵ is the ellipticity defined as the ratio of the electric field components. According to the semiclassical model, a laser field with a non-zero ellipticity ϵ causes a lateral displacement Δy to the returning electrons. This displacement can be compensated if the returning electrons are launched with a transverse momentum $p_\perp$ (a quantum-mechanical feature) equal to:

$$p_\perp(t_i) = \Delta y / (t_r - t_i) \quad . \tag{2.16}$$

Only these electrons can contribute to the HHG emission. The dependence of the normalized harmonic yield on the driving field can, therefore, be simplified in the following form:

$$\frac{I_{XUV}(\epsilon)}{I_{XUV}(\epsilon=0)} \approx \frac{\text{The probabilty that the electron tunnels with} \quad p_\perp : w(p_\perp)}{\text{The probabilty that the electron tunnels with} \quad p_\perp = 0 : w(p_\perp = 0)} \quad . \tag{2.17}$$

The Gaussian dependence of the ionization probability on $p_\perp$ given in eq. 2.6 explains qualitatively the observed Gaussian dependence of high-order-harmonic yield on ellipticity ϵ [16]. It also shows that this dependence is different for short and long electron trajectories. To obtain a better quantitative expression for the modulation of the measured yield of harmonics with ellipticity in simple systems, Strelkov [17] treated the electron trajectory classically along the major axis of the ellipse whereas the perpendicular motion of the wave packet was treated quantum mechanically. Consequently, an analytic form of the ellipticity width $\Delta\epsilon$, defined as, the ellipticity value at which the harmonic yield drops to 50% compared to the value at linear polarization, was derived to be:

$$\Delta\epsilon = \frac{\omega}{2\sqrt{\sqrt{2I_p}E\cos(\omega t_i)}} \quad . \tag{2.18}$$

It is possible to approach this problem with a full quantum mechanical treatment based on numerical solution of the time-dependent Schrodinger equation (TDSE). However, an alternative and simpler method using quantum-orbit analysis [18] can provide results with comparable accuracy and more physical insight into the process. Unlike the classical trajectories, the quantum orbits are trajectories that evolve in complex time with complex

parameters including; canonical momenta, velocities, and displacements. These complex trajectories can be found by obtaining the stationary points of the action S. The dependence of the harmonic yield Y on ellipticity following this approach is given by

$$Y(\epsilon) \sim \exp[2\mathrm{Im}(S(\epsilon))] \quad . \tag{2.19}$$

2.1.4.2.2 Two-colour field

When a second harmonic $E_{2\omega}cos(2\omega t + \Phi)e_y$, where Φ is a constant phase, is added orthogonally to the fundamental driving field $E_{\omega}cos(\omega t)e_x$ to generate high-order harmonics, the mirror symmetry of the field in the two successive half-cycles of the main field is broken, thus even order harmonics can be generated. Controlling the relative phase Φ between the perpendicularly polarized bichromatic fields has been demonstrated, for example, to enhance the HHG efficiency, generate shorter attosecond pulses [19] and to select trajectory type (short/long) [20]. The presence of even harmonics in two-colour HHG was also shown to provide an extra observable to probe the symmetry of the atomic wavefunction in neon[21].

2.1.4.3 Propagation effects

High harmonic generation suffers from low conversion efficiency. For example, efficiency rates as low as 10^{-5} have been reported at 800 nm light [22]. This inefficiency can be attributed partly to the weak atomic response. Moreover, since the recorded HHG spectra are composed of the coherent sum of radiation generated by all atoms in the medium in the forward direction, the conversion efficiency also depends on the propagation of the HHG

emission. This propagation of the harmonic field is mainly governed by phase matching and reabsorption.

2.1.4.3.1 Phase matching

In any nonlinear optics process, phase matching of the generated harmonic and the fundamental laser is required to obtain a considerable amount of the output signal. To achieve perfect phase matching, the phase mismatch Δk, defined as the difference between the wave vectors of the fundamental driving laser k_0 and the qth order harmonic k_q, must vanish:

$$\Delta k = qk_0 - k_q \tag{2.20}$$

In this case, the intensity of the generated radiation rises quadratically with propagation distance. If the above phase matching condition is not satisfied, then the harmonic signal oscillates sinusoidally over a propagation distance, known as the coherence length, $L_{coh} = \pi/\Delta k$.

Several sources contribute to the phase mismatch Δk in a medium:

1. **Trajectory-type dependent phase:** For a single emitter, the phase of a single harmonic has two components. The first component depends on the laser phase at the time of recombination whereas the second represents the phase accumulated by the electron wavefunction during the propagation in the continuum. Thus, the total microscopic phase can be written as:

$$k_{microscopic} = \omega t_r - S(t_i, t_r)/\hbar \quad . \tag{2.21}$$

where t_i and t_r are the ionization and recombination times respectively and S is the quasi-classical action. Since both parts depend on time, a given harmonic order can have different phases depending on whether the type of the associated trajectory is short or long. The fact that the microscopic phase depends on the action implies that it is intensity-dependent. Long trajectories are more sensitive to this dependence. Due to the radial variation of the laser intensity, the phase fronts for harmonics corresponding to long trajectories are significantly curved. As a consequence, long trajectories lead to the emission of more divergent harmonics compared to short trajectories [23].

2. **Target dispersion:** The speed of the light inside a medium is determined by its refractive index. In general, this parameter is frequency-dependent and thus the laser and each harmonic travel at different speeds. This variation causes the harmonics generated at different points in space to be out of phase with each other. There are two main sources of dispersion in the interaction medium, neutral atoms and free electrons formed by the HHG process. Ion-produced dispersion is relatively small and usually neglected. The dispersion caused by the gaseous medium as a function of wavelength λ can, therefore, be expressed as [24]:

$$\begin{aligned} n(\lambda) = &\quad n_{atom}(\lambda) + n_e(\lambda) \\ = &\quad 1 + (1-\eta)P\delta(\lambda) - \eta P N_{atom} r_e \lambda^2/2\pi \quad , \end{aligned} \tag{2.22}$$

where η is the ionization fraction, P is the pressure in atmospheres, $\delta(\lambda)$ is the gas dispersion function, N_{atm} and r_e are the molecular number density at 1 atm and the

classical electron radius respectively. The nonlinear refractive index is not included in the above expression since it plays a negligible role at laser intensities used in typical HHG experiments [24]. The total phase mismatching caused by a dispersive medium is:

$$\Delta k_{meduim} = -\frac{2\pi(1-\eta)P}{\lambda_q}[\delta(\lambda_0) - \delta(\lambda_q)] + \eta P N_{atom} r_e(q\lambda_0 - \lambda_q) \quad , \tag{2.23}$$

where λ_0 and λ_q are the wavelengths of the fundamental field and the qth harmonic respectively.

3. **Gouy phase mismatch:** All focused Gaussian beams experience a phase variation of π across the focal region. This change in the phase of the electric field is known as Gouy phase shift. This source of phase mismatching can be eliminated by placing the focus after or before the region with the highest gas densities.

Since the gas medium is isotropic, traditional phase matching techniques, (often used for low-order harmonic generation such as second harmonic generation), can not be applied. However, considerable phase matching can be achieved through minimizing the phase mismatch Δk by balancing various contributing terms. In all experimental conditions reported in this thesis, short trajectories were preferentially phase matched. In practice this can be confirmed by observing, for example, that i) the harmonics are spectrally narrow and spatially collimated and ii) the harmonic yield depends on laser ellipticity as predicted for short trajectories.

2.1.4.3.2 Reabsorption

In addition to coherence length L_{coh}, generating medium length L_{med} and absorption length L_{abs} are two other length parameters which control the efficiency of high harmonics. The latter is defined as the length over which the intensity of the harmonic radiation decreases by a factor of exp(0.5) due to absorption by the generation medium. This length is expressed as $L_{abs} = 1/(\sigma\rho)$, where σ and ρ are the photoionization cross section and gas density in the interaction region, respectively. From a simplified 1D model developed by Constant *et al.* [25], the following results were reported:

1. For $L_{abs} \to \infty$, no re-absorption, the signal grows quadratically as a function of L_{med}.
2. In the presence of absorption, the yield saturates once L_{med} is longer than L_{abs} by a few times even at infinite coherence length L_{coh}.
3. The optimal efficiency can be found for $L_{coh} > 5L_{abs}$ and $L_{med} > 3L_{abs}$.

In general, higher atomic density and longer medium length do not always result in an increase of harmonic emission. The management of the interplay between the three length parameters is important for achieving large conversion efficiencies.

For comparative measurements of harmonic emissions from different atomic (molecular) sources, it is important that they are performed at the same pressures and away from pressure saturation. Also the results need not be sensitive to pressure variations in order to be attributed to single atomic (molecular) responses.

2.2 Molecules in a strong laser field

Molecules are more complex systems than atoms, with lower ionization potentials, a higher density of quantum states and more degrees of freedom. The extension of strong laser field physics from atoms to molecules is, therefore, difficult and leads to richer structural and dynamical information. To understand the main aspects of such an extension, a brief background is first presented on the basic characteristics of molecular orbitals and how they can be constructed from atomic orbitals, followed by an overview of some high-field phenomena in molecules.

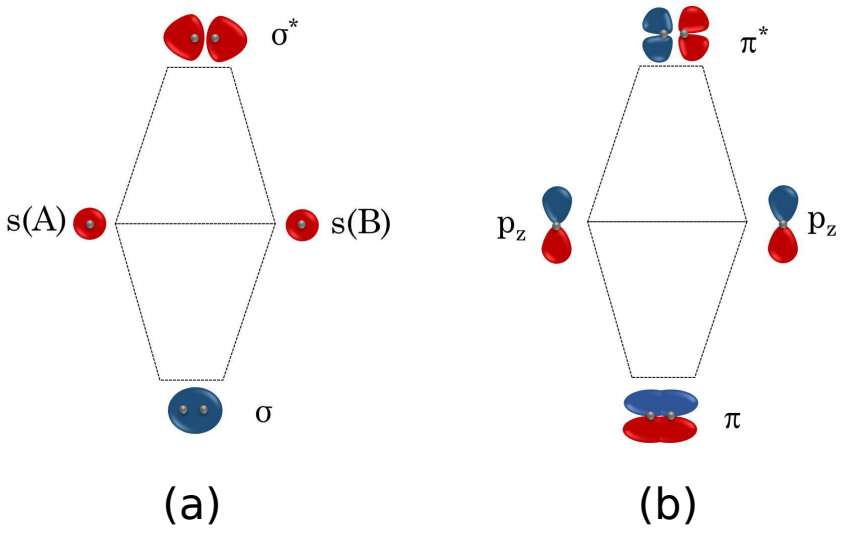

Figure 2.4: Formation of molecular orbitals in diatomic molecules from linear combinations of (a) s and (b) p_z atomic orbitals. The capital letters A and B denote atomic nuclei. Different phases of the electron wavefunction are represented by different colours.

2.2.1 Molecular orbitals

As a first approximation, molecular orbitals can be constructed by a linear combination of atomic orbitals (LCAO). As with most quantum chemical approaches, the Born-

Oppenheimer approximation is inherently assumed, where nuclei are considered to be frozen. As an example of the LCAO method, consider two s orbitals for two separate Hydrogen atoms, A and B. When the separating distance R between the two atoms is sufficiently short, a diatomic molecule (H_2) is formed. In this case, the resulting electronic wavefunction is simply a quantum superposition of the two s-atomic wavefunctions:

$$\psi(r) = C_A\psi_s^A(r - R/2) \pm C_B\psi_s^B(r + R/2) \quad , \tag{2.24}$$

where ψ_A and ψ_B are the two atomic wavefunctions and C_A and C_B are amplitude coefficients. The two possible molecular orbitals are shown in Fig. 2.4a. The wavefunction constructed from the sum of the two atomic wavefunctions is called σ. This orbital is bonding because it has a nonzero electron probability between the two nuclei. On the other hand, destructive interference of the two atomic wavefunctions results in an anti-bonding orbital σ^*. Both molecular orbitals are depicted in Fig. 2.4a. The opposite signs of the wavefunction phases are indicated by dark and light colouring of the lobes. Since each orbital can accommodate two electrons, the σ orbital is considered the highest occupied molecular orbital (HOMO) in H_2. In terms of energy, the HOMO has a lower energy than that of the original two atomic orbitals; hence the molecule is stable.

Similarly, if we superimpose two p_z atomic orbitals, π and π^* molecular orbitals are formed (Fig. 2.4b). In contrast to π-type orbitals, σ-type orbitals are symmetric with respect to rotation around the internuclear axis. In some orbitals shown in Fig. 2.4, there are regions with zero electron density between the nuclei known as nodal planes and created due to cancellation of the two wave functions.

More advanced and complex approaches are generally adopted to treat quantum-chemistry problems. Based on these methods, a software package such as GAMESS [26] can be employed to perform *ab initio* calculations of molecular orbitals at a satisfactory level. However, the LCAO method remains a powerful pictorial tool to capture the main characteristics of the electronic structure of a molecule. This basic treatment provides the following general features of the electronic structures in molecules compared to atoms: 1) stable molecules have a lower ionization potential , 2) the energy spacing between molecular orbitals is lower, and 3) molecular orbitals have generally a complex symmetry.

2.2.2 Molecular alignment

In contrast to atoms, molecular systems have a rotational degree of freedom that can interact with an external field. When the duration of a strong, non-resonant and non-ionizing laser pulse is significantly shorter than the rotational period of a molecule, then the molecule cannot align adiabatically with respect to the polarization direction of the field. Instead, many rotational states of the molecule can be excited, thus forming a rotational wave packet. After the interaction with the laser pulse, the different components of this wave packet remain constant but the phases evolve over time. Therefore, the molecule periodically aligns (anti-aligns) along (perpendicular to) the polarization direction of the laser pulse at characteristic times. An intensity on the order of 10^{13} W/cm^2 is typically employed to considerably align a molecular gas with a rotational temperature of 100s of Kelvin.

Many strong laser field processes in molecules are sensitive to molecular orientation

with respect to laser field. Developing field-free alignment techniques has allowed for the observation of these process in a molecular frame and has enabled HHG, for example, to image molecular orbitals in N_2 and probe hole dynamics in CO_2. Although extending this technique to complex molecules is difficult, the work presented in this thesis and other similar studies show that HHG is capable of deciphering structural and dynamical information from complex molecular systems even in a randomly-oriented sample.

2.2.3 Molecular ionization

Tunnel ionization has an exponential dependence on the ionization potential of the target. Therefore electrons generally escape only from the orbital with the lowest nuclear binding energy in an atom. However, since molecular orbitals are energetically closely spaced, ionization from several lower lying orbitals besides the HOMO can be significant. In fact, there is experimental and theoretical evidence, including parts of this thesis, that the SFI contribution from HOMO, compared to lower-lying orbitals, could be less significant over

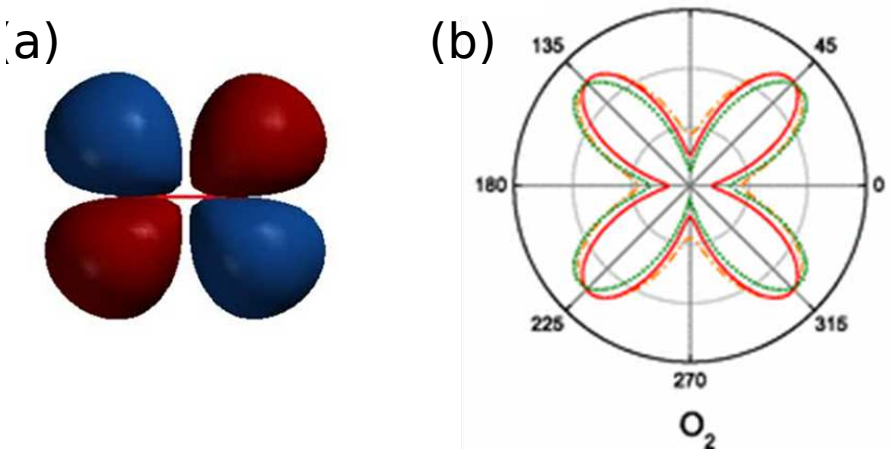

Figure 2.5: The highest occupied molecular orbital (HOMO) in O_2. b) Measured (red solid line) and calculated (green dotted line) angular ionization signal from the HOMO in O_2. From [27]

all orientations or along certain directions.

In general, molecular orbitals display complex symmetries with multiple nodal planes. Therefore, an appropriate method for calculating the orientational ionization rates from molecules must be used. The ADK model was extended further to model the ionization rates from molecules and is now known as the MO-ADK theory [28]. As an example of applying this method, the HOMO in O_2 has two perpendicular nodal planes as shown in Fig. 2.5a. MO-ADK-based calculations predict that ionization peaks when the laser polarization makes an angle of 40° with respect to the molecular axis. On the other hand, very little yield is expected at 0 and 90° where the two nodal planes are oriented. This prediction is in a good agreement with the measured angular ionization dependence [27] shown in Fig. 2.5b. A part of this thesis (chapter 6) shows that the orientational dependence of ionization rates from some polyatomic molecules cannot follow a description based on MO-ADK theory.

The single active electron approximation (SAE) is a central approximation for the description of strong field processes. In principle, and to a high extent, SAE represents an exact solution for systems with an electron occupying an orbital outside a closed shell [29]. In other types of systems, the probability that multiple active electrons (MAE) could interact simultaneously with a strong laser field is relatively higher. Including this fact is still challenging. However, the possibility of such excitations can be neglected. This is supported by the fact that theoretical SAE-based approaches can explain many strong laser field experiments in a variety of molecular systems, particularly those of sizes similar to (or smaller than) the sizes of molecules investigated in this thesis.

Although the Keldysh parameter is a fair approximate guideline for atoms, applying this concept to molecules is questionable. The major shortcoming of this indicator is that ionization potential is the only molecular parameter that is accounted for. To have a better prediction of the transition between ionization regimes, DeWitt *et al.*[30] proposed a modified parameter in which electronic orbital shape and size are incorporated.

2.2.4 Molecular dissociation

In addition to electronic excitation and ionization, an intense laser field can excite the nuclear degrees of freedom in molecules. As a result, the excited molecule could decay into smaller products, for example:

$$H_2 + n\hbar\nu \longrightarrow H^+ + H + e \quad .$$

An extreme fragmentation process is called Coulomb explosion where the strong field removes the electrons from H_2 for example, and leaves behind two protons, which repel each other:

$$H_2 + n\hbar\nu \longrightarrow H_2^+ + n\hbar\nu \longrightarrow H^+ + H^+ + e \quad .$$

Avoiding extensive fragmentation is necessary for better phase matched harmonics which are produced from the parent molecule and not from the dissociation products [31]. This can be achieved by exploiting sufficiently short pulses and quite low laser intensities.

2.2.5 Electron recombination to a molecular ion

During the recombination step, the incoming wavefunction could be influenced by different aspects of molecular structure and dynamics including:

1. **Coulomb potential:** In molecules, the structure of the Coulomb potential could distort the initial shape of the continuum wavefunction and perturb the incoming wavefunction during the recombination step. Both cases question the validity of applying the SFA approximation to some molecular systems since it inherently treats the ionizing electron quantum state as a plane wave.

2. **Multi-centre effect:** Molecular orbitals usually have a multi-centre structure that is related to the positions of the atoms that make up the molecule. Due to the fact that this structure is on the scale of the de Broglie wavelength of the recolliding electron, interference effects could occur during the third step of the HHG process [32]. For example, for the HOMO of H_2 described in equation 2.24, the incoming wavefunction sees two probable centres for recombination. To analyse this effect, we assume that the molecular potential has a short range. In this case and following Lein *et al.*[32], we can treat the recombination step for each nucleus separately. Consequently, the Fourier transform of the dipole acceleration can be written as:

$$\mathcal{A}(\omega) = \mathcal{A}_1(\omega) + \mathcal{A}_2(\omega) \quad . \tag{2.25}$$

Here $\mathcal{A}_1(\omega)$ and $\mathcal{A}_2(\omega)$ are the Fourier transform of the integrated HHG dipole acceleration of the two nuclei. The regions of integration are chosen to be small and

centred at each nuclei. For simplicity, the incoming wavefunction can be represented as a plane wave given by:

$$\psi_{el} = e^{ik.r - iE_k/\hbar t} \quad . \tag{2.26}$$

Consequently $\mathcal{A}(\omega)$ becomes proportional to:

$$\mathcal{A}(\omega) \propto e^{ik.r_1} + e^{ik.r_2} \quad . \tag{2.27}$$

The two contributions to the recombination amplitude can interfere destructively or constructively depending on their phase difference:

$$\Delta\Phi = k.\Delta r = 2\pi/\lambda_{dB} R\cos\theta \quad . \tag{2.28}$$

Here θ is the angle between the laser polarization vector and the internuclear axis. We can write the interference condition as:

$$Rcos\theta = \begin{cases} n\lambda_{dB} & \text{constructive} \\ (n+1/2)\lambda_{dB} & \text{destructive} \quad , \end{cases} \tag{2.29}$$

where n is an integer. For an anti-bonding (asymmetric) orbital, the condition is reversed.

3. **Hole dynamics:** Since molecular ionization can result from multiple channels, the state of hole left behind during the propagation step can be considered as a superposition of the ionizing channels [33]. Probing hole dynamics is a powerful HHG

spectroscopic tool that provides attosecond time-resolved measurement. Assuming that there are two active ionization channels A and B, the time evolution of the hole can be written as:

$$\psi_H(t) = \alpha_A \psi_A + \alpha_B e^{i(\Delta\varphi + \Delta I_p t)} \psi_B \quad , \tag{2.30}$$

where $\Delta\varphi$ is an initial phase difference between the two channels and α_A and α_B are the ionization rates of channels A and B respectively. When these two weighting coefficients are comparable, there is a certain moment where the two channels interfere destructively. If this time corresponds to the returning time for a specific harmonic, then a dip in the harmonic spectra is usually observed. This correspondence makes the observed spectral modulation sensitive to laser parameters that affect the excursion time of the electron.

For two-colour HHG, it was shown that the dynamical interference in CO_2 is associated with a special signature in the maximum harmonic signal as a function of the phase between the two colours Φ [34]. At around the spectral minimum, this phase was observed to be shifted by $\sim \pi/2$ as indicated by the white curve in Fig. 2.6. This phase jump can be understood from the following theoretical analysis [34]. In the presence of two active channels, labelled $i = 1, 2$, the intensity of the N^{th}-order harmonic S_N in the absence of the second colour can be written as the coherent sum of the harmonic intensity associated with each channel $S_N^{(i)}$:

$$S_N = S_N^{(1)} + S_N^{(2)} + 2\sqrt{S_N^{(1)} S_N^{(2)}} \cos(\Delta\varphi_N) \quad , \tag{2.31}$$

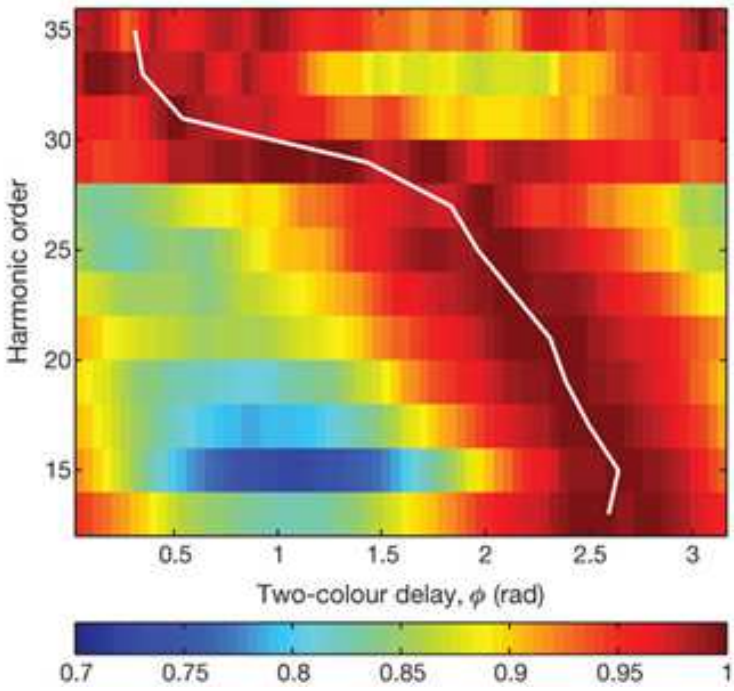

Figure 2.6: Normalized high-harmonic spectra (colour scale) from CO_2 molecules aligned parallel to laser polarization as a function of the delay between 800 nm laser beam (40 fs and 1.3×10^{14} W/cm^2) and its second harmonic. The maximum signal is indicated by the white curve. From [34].

where $\Delta\varphi_N$ is the relative phase between the two channels mentioned earlier. In two-colour HHG, the signal corresponding to each channel varies with the relative phase between the two colours Φ as:

$$\tilde{S}_N^{(i)}(\Phi) = S_N^{(i)}\,[G_N^{(i)}(\Phi)]^2 \quad . \tag{2.32}$$

Here $G_N^{(i)}(\Phi)$ is called the two-colour gate and describes the modulation of the harmonic amplitude as a function of Φ. The values of $G_N^{(i)}(\Phi)$ are very close to each other for channels with comparable ionization potentials. As a result, the total signal in

equation 2.31 can be linearized as follows:

$$\tilde{S}_N(\Phi) \approx G_N^2(\Phi)\, S_N\, (1 + \frac{\Delta G_N(\Phi)\, \Delta S_N}{G_N(\Phi)\, S_N}) \quad , \tag{2.33}$$

where $G_N = (G_N^{(1)} + G_N^{(2)})/2$, $\Delta G_N = G_N^{(1)} + G_N^{(2)}$ denotes the differential gate and $\Delta S_N = S_N^{(1)} - S_N^{(2)}$. In general, the differential gate has no noticeable effect on the total signal $\tilde{S}_N^{(i)}(\Phi)$ since $\Delta G_N \ll G_N$ and $\Delta S_N \ll S_N$. However, when a destructive interference occurs between the two channels, the second term in equation 2.33 dominates where:

$$\begin{aligned} & S_N^{(1)} \approx S_N^{(2)} \quad \text{and} \quad \cos(\Delta\varphi_N) = -1 \\ \Rightarrow \quad & \Delta S/S = (\sqrt{S^{(1)}} - \sqrt{S^{(2)}})\,(\sqrt{S^{(1)}} + \sqrt{S^{(2)}})/(\sqrt{S^{(1)}} - \sqrt{S^{(2)}})^2 \\ & = (\sqrt{S^{(1)}} + \sqrt{S^{(2)}})/(\sqrt{S^{(1)}} - \sqrt{S^{(2)}}) \gg 1 \quad . \end{aligned} \tag{2.34}$$

Consequently, the differential gate $\Delta G_N(\Phi)$ controls the response of $\tilde{S}_N^{(i)}(\Phi)$ to the variation of the relative phase between the two colours. Compared to the single channel gate $G_N(\Phi)$, the differential gate $\Delta G_N(\Phi)$ is shifted by $\sim \pi/2$. This explains the observed abrupt change of phase Φ corresponding to the maximum harmonic signal in Fig. 2.6.

The above description of hole dynamics is for free evolution. Another interesting aspect of hole dynamics occurs when the hole interacts with the strong laser field. This effect was utilized recently by our group to probe chirality in molecules [35].

4. **Nuclear motion:** When the electron exits the tunnelling barrier, the ground vi-

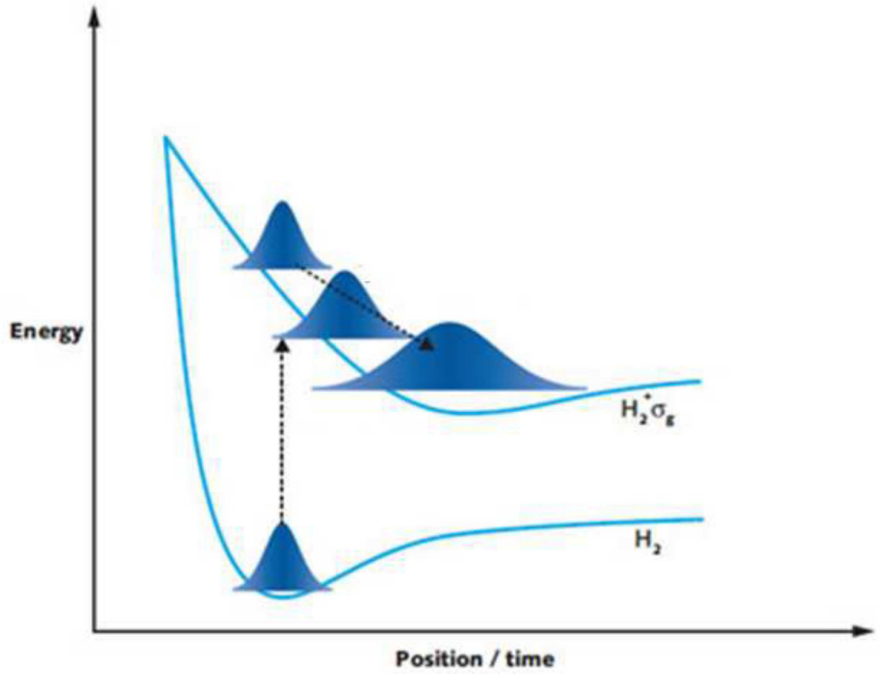

Figure 2.7: The evolution of the vibrational wavepacket during the recombination step in H_2^+. From [3]

brational state of the molecule is not an eigenstate of the cation but instead is a superposition of cation vibrational eigenstates. This vibrational state evolves during the time of recombination which is on a femtosecond scale and its effects can be appreciated more for light nuclei as in H_2 (Fig. 2.7). For example, Lein [36] showed that the harmonic ratio of D_2/H_2 generally increases as the harmonic order increases. This can be understood given that the higher the harmonic order, the longer the time the vibrational state takes to evolve to different states. However, for a full account of this isotopic effect, one needs to consider other factors like the differences in ionization probability and system dimensionality [37].

Molecular high-order harmonic generation particularly in poly-atomic molecules is a complex process and involves the interplay of several effects. However, HHG spectroscopy

of such systems can lead to a wealth of molecular and electronic information especially with the availability of high energy mid-infrared light sources in the 1.4-2 μm wavelength region. Longer wavelength of the laser field is desirable to generate HHG in molecules having a low ionization potential in the 8-11 eV range as it (a) ensures adiabatic ionization (b) extends the cutoff harmonic to capture signatures of electronic structure and dynamics [38, 39], (c) increases sensitivity to laser ellipticity, and (d) favors better phase matching at higher gas densities [40].

Chapter 3

Experimental Setup

This chapter contains the details of the experimental set up and methods. It includes a description of the femtosecond laser system and the apparatus used to produce and detect ions and high-order harmonics.

3.1 Femtosecond laser system

Photoionization experiments reported in this thesis were performed with a commercial amplified Ti:sapphire laser system at the University of Ottawa. This system starts with a femtosecond oscillator (Tsunami, Spectra-Physics, Santa Clara (USA)) pumped by a 5 W Nd:YVO4 diode solid-state laser (Millenia,Spectra-Physics, 532 nm). The pulses generated by the oscillator have a pulse duration of less than 30 fs with a pulse energy of 8 nJ at 800 nm. The repetition rate of the system is 76 MHz, determined by the length of the laser cavity. The energy of these pulses are amplified by sending them into a regenerative

amplifier (Spitfirepro, Spectra-Physics). Before amplification, the pulses are i) stretched temporally using a grating-based stretcher to prevent damage to the Ti:sapphire crystal and ii) selected by a Pockels cell to lower the repetition rate to 1 kHz. After being amplified by passing through a Ti:sapphire crystal several times, the pulses are i) ejected by a second pockels cell and ii) compressed at the exit by a grating compressor. The amplified beam has an output power of 2.5 W at a pulse duration of 45 fs measured before passing through any additional optics by a home-built single shot autocorrelator.In these experiments, the pulse energy was controlled by a zero order half-wave plate along with a thin film polarizer. The ellipticity of the laser was adjusted using a zero order quarter wave-plate. These dispersive optics plus the entrance window (fused silica) stretched the pulse duration up to 49 fs.

HHG experiments were conducted at the Advanced Laser Light Source (ALLS) facility in Varennes, Quebec, with mid-infrared pulses. These pulses are first produced by an optical parametric amplifier (OPA) pumped by a Ti:Sapphire laser generating 45 fs pulses with an energy of 4.5 mJ and operating at a wavelength of 800 nm and a repetition rate of 100 Hz. The two longer IR wavelengths (signal and idler) are generated in the OPA system through the process of difference frequency generation The output beam (either the signal or idler) is spatially filtered and then amplified by passing through a large BBO crystal pumped by high-energy 800 nm light [41]. The pulse duration of the final output was optimized and measured after passing through all optics in the beam path except for the focusing and the entrance window of the HHG chamber. Both elements are made of calcium fluoride (CaF_2) which has a very low group velocity dispersion compared to other materials in the wavelength range of interest. The pulse duration was found to be in the

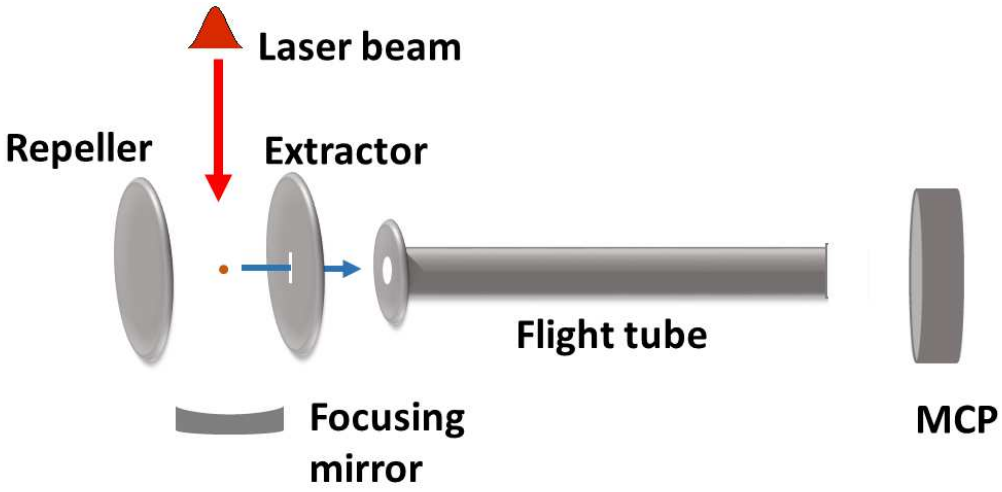

Figure 3.1: Schematic of the time-of-flight mass spectrometer.

range 50-70 fs and was measured by frequency resolved optical gating (FROG) technique.

3.2 Time of flight apparatus

Molecular ionization and ion fragmentation were examined using ultra vacuum chamber equipped with a time of flight (TOF) spectrometer of Wiley-McClaren type [42] as sketched in Fig. 3.1. The primary functions of the TOF system are to: i) extract ions from the interaction region, ii) separate them according to mass to charge ratio m/q, and finally iii) measure their number. The molecular gas was introduced into the system relying on vapor pressure at room temperature. During experiments, the pressure in the TOF chamber was kept at $\sim 10^{-7}$ torr whereas the base pressure of the vacuum system was $\sim 10^{-9}$ torr. Ions were created by focusing the laser beam by a spherical mirror into the center of two plates (the repeller and extractor electrodes). The mirror was mounted on a three dimensional translation manipulator to control the focus.

Two different voltages were applied to the repeller and extractor respectively in order to accelerate the produced ions and were tuned to ensure better mass resolution. Then the ions were sent through a field-free drift tube after passing through a 1 mm $\times$ 9 mm slit in the middle of the extractor plate. The ions reach a microchannel plate (MCP) detector in different times determined by m/q ratio. The MCP is biased to postaccelerate the incoming ions and then send a voltage signal to a time digitizer when an ion impinges on the detector. The digitizer is connected to a computer which records every ion occurence in the software and subsequently generates a spectrum defined by the signals of the MCP and a trigger from the laser source.

The x-axis of the TOF spectra is defined by the time that the ions hit the detector T_{flight}. In order to characterize the mass spectra, arrival time T_{flight} is required to be converted into a mass to charge (m/q) ratio. T_{flight} has a quadratic dependence on m/q and this dependence is determined, in practice, by identifying ion peaks in the mass spectrum with known m/q such as H_2O^+, O_2^+ and N_2^+.

The intensity of the laser beam was calibrated by measuring the ion yield for atomic targets such as Ar or Xe. The ion signal is then plotted as a function of laser pulse energy in a semi-log plot as shown in Fig. 3.2. At higher pulse energies, the atoms are fully ionized in the most intense part of the beam. The linear part of the ion signal curve reflects the asymptotic behaviour of the ionization rate resulting from the expansion of the focal volume as the pulse energy increases. Extrapolating this portion back to the intensity axis defines the saturation energy E_{sat}, where the pulse ionizes 43% of the target. Comparing the measurement with ADK-model based calculations gives the saturation intensity I_{sat}.

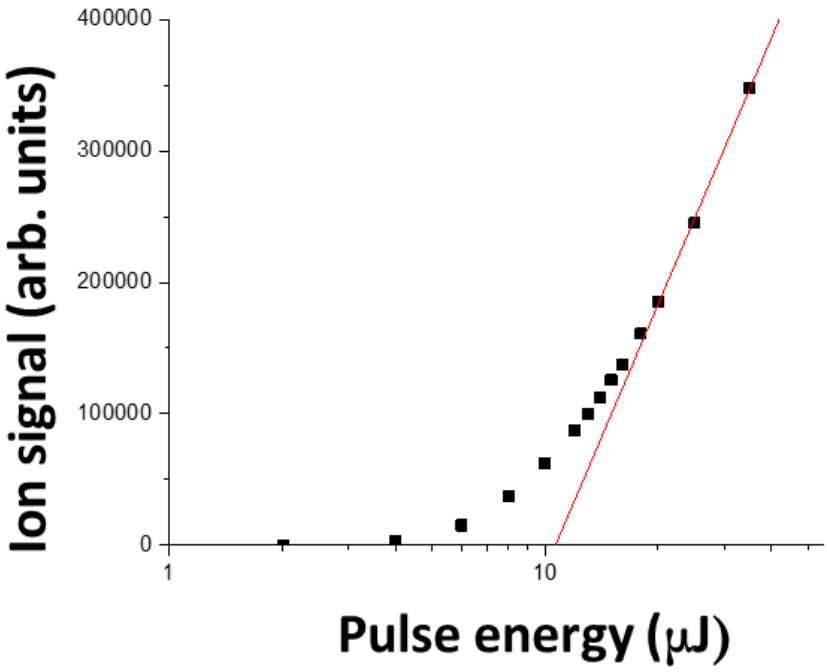

Figure 3.2: A semi-log plot of Xenon yield as a function of pulse energy at 800 nm. The saturation energy is defined by the extrapolation of the linear portion of the ion signal curve to zero.

3.3 High-harmonic generation apparatus

3.3.1 General description

Harmonics were produced by focusing mid infrared pulses using a 50 cm CaF_2 lens into gas target confined in a gas source, which was either a gas cell or pulsed valve. To minimize the absorption of the XUV radiation outside the focus, the gas source was placed in a generating chamber kept under high vacuum ($\sim 10^{-7}$ torr). Then the produced radiation passed into a detection chamber where it was recorded. The energy of the amplified IR beam was varied from 200 μJ to 2mJ by using a half-wave plate placed in front of a germanium plate which works as a polariser by reflection. The ellipticity of the incident

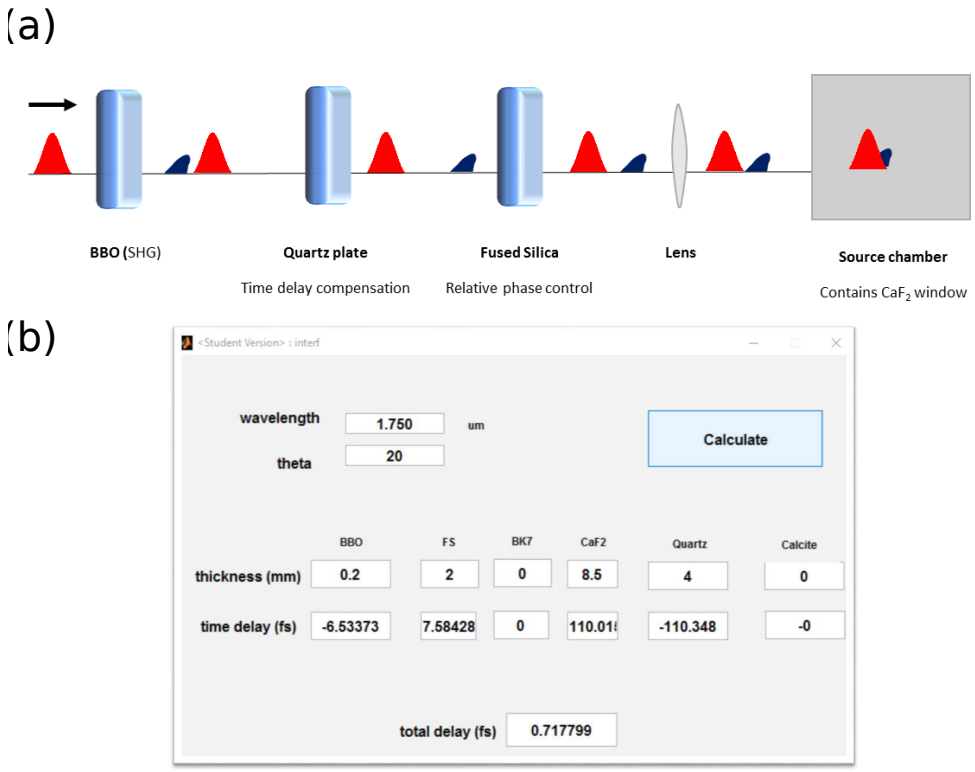

Figure 3.3: (a)Two-colour setup. (b) The time delay introduced between the two pulses by different setup components.

light was controlled by a combination of an adjustable half-wave plate and a fixed quarter-wave plate. This arrangement ensured that the main axis of the ellipse is fixed in space. This is very important since the detection system has some degree of sensitivity to the polarization state of the incident light.

3.3.2 Two-color setup

In chapter 7, HHG with orthogonal two-colour field was used in order to explore multi-orbital dynamics in 1,4 cyclohexadiene. The two-colour setup is sketched in Fig. 3.3a. This process consists of three steps i) generating a second harmonic to be added to the main field. ii) compensating the time delay and iii) controlling the phase between the two

colours.

3.3.2.1 Second harmonic generation SHG

The first part in this setup is the doubling of the fundamental frequency using a nonlinear medium. In addition to its other unique features, β-Barium Borate (BBO) crystal was chosen to serve as a generating medium due to its high nonlinear susceptibility, hence better SHG efficiency. BBO is a negative uniaxial crystal, with $(n_o > n_e)$ where n_o and n_e are the ordinary and extraordinary refractive-indices respectively. We used a fundamental wavelength of $\lambda \sim$1750 nm and applied type I phase matching where:

$$\omega(\mathrm{o}) + \omega(\mathrm{o}) = 2\omega(\mathrm{e}) \quad . \tag{3.1}$$

In this case, the condition for phase-matching the two fields inside the crystal becomes:

$$n_o(\omega) = n_e(2\omega, \theta) \quad . \tag{3.2}$$

Here θ is the angle between the the optic axis of the crystal and the wavevector of the incoming pulse. Since the extraordinary refractive-index depends on θ, this angle can be tuned to satisfy the above condition. Our crystal was pre-cut at the phase-matching angle of 20$^{\mathrm{o}}$.

The thickness of the crystal (L) is a critical parameter. Higher L means higher SHG efficiency. However, it also leads to undesirable consequences such as longer second harmonic pulse. In our application, we required a lower power of the second harmonic (a

maximum conversion efficiency of ∼10%), so a thin crystal with a width of 200 μm was chosen. In this case, the disadvantages associated with thicker crystals have less impact.

3.3.2.2 Delay control

The two pulses (ω, 2ω) travel at different group velocities due to dispersion leading to time delay between the two pulses. Two-colour HHG requires that both fields overlap spatially and temporally at the target. Since both colours propagate collinearly, the spatial overlap is already satisfied. However, this makes the achievement of temporal overlap not possible in an interferometric setup by making the faster (slower) pulse travel longer (shorter) along separate paths. Alternatively, a birefringent crystal can be used to compensate for time delay by sending the faster (slower) pulse along the slower (faster) axis of the crystal. Before reaching the harmonic generating targets, the accumulated time delay between the two pulses is given by:

$$\tau_{delay} = \sum_{i=1}^{n} d_i \left(\frac{1}{v_g(2\omega)} - \frac{1}{v_g(\omega)}\right) \quad . \tag{3.3}$$

The different optical components lead to $\tau_{Delay} \approx 100$ fs (Fig. 3.3b). To compensate this delay, we used a quartz crystal with a total thickness of 4 mm. In practice, tilting the quartz plate was used for tuning the time overlapping between the two pulses. This was verified by using a second BBO crystal to perform third harmonic generation by sum frequency generation of ω and 2ω. To minimize any interference of the dispersion of the second BBO on the optimization process, we selected the second crystal to be thin (200

μm) and employ the following scheme for phase matching:

$$\omega(\mathrm{o}) + 2\omega(\mathrm{e}) = 3\omega(\mathrm{e}) \quad . \tag{3.4}$$

which introduces less time delay compared to the other possible scheme defined by:

$$\omega(\mathrm{e}) + 2\omega(\mathrm{o}) = 3\omega(\mathrm{e}) \quad . \tag{3.5}$$

3.3.2.3 Phase control

The optical path difference between the two colours was controlled with subcycle precision by rotating two 1 mm thick fused silica plates. The advantage of using two plates with the same thickness instead of one plate is that they can be rotated in opposite directions with the same angle, hence the beam path is not deflected during phase change.

3.3.3 Source chamber

The extreme-ultraviolet (XUV) radiation produced by the HHG process is strongly absorbed by almost all materials. It, therefore, requires a relatively high gas density near the focus for generation and high vacuum outside the focus for propagation. Two types of HHG sources were used for the experiments reported in this thesis:

1. **Pulsed valve:** gas is emitted from a pulsed gas jet at a repetition rate of 100 Hz. It has a 500 μm orifice with a typical interaction length of 1 mm. It is mounted on

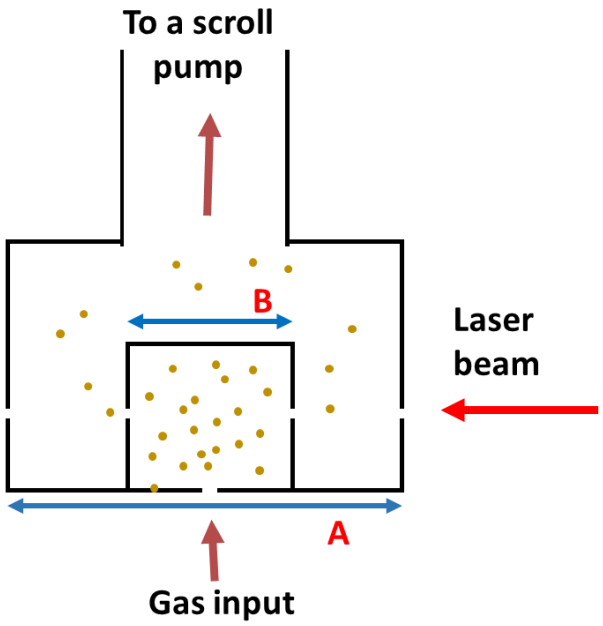

Dimension	A(mm)	B(mm)
Gas cell 1	30	11
Gas cell 2	25.4	4

Figure 3.4: A schematic description of finite gas cells used in HHG experiments

an XYZ manipulator for better precision alignment with respect to the focused laser beam. This source was used for experiments described in chapter 6.

2. **Gas cell:** Compared to a pulsed valve, gas in a cell has a static flow with a higher density and a longer interaction length. As a result, gas cells have better conversion efficiency. On the other hand, pulsed valves are desirable for applications that require molecular alignment since the molecules in this source are rotationally cold. Fig. 3.4 shows a schematic description of two versions of gas cells used in experiments for this thesis. Gas cell #1 was employed for experiments in chapter 7 while gas cell #2 was used in experiments described in chapter 4, 5 and the two-colour experiment in

chapter 7. Both sources have two concentric cylinders where inner and outer cylinders have 600 μm inline pinholes to allow for the passage of the focused beam. Similar to a pulse valve, the positions of the gas cells were controlled by a three-dimensional manipulator. A 10 cm Teflon tube is employed to transfer gas into the inner cylinder. The gas pressure in the tube is kept at a few Torr and is measured with a Baratron gauge. A rough pump (500 L min^1) was used to pump the outer cylinder. This differential pumping geometry reduces the flow of gas into the surrounding vacuum systems where they are placed. In general, both gas cells have similar characteristics. However, the latter one had a better performance in keeping the source chamber at a high vacuum.

3.3.4 Detection chamber

After being produced in the generation chamber, the XUV light passes through a 5 cm differential pumping tube with a 3 mm aperture towards the detection chamber. Then the harmonics were spectrally dispersed by a flat-field concave grating (1200 lines mm^{-1}) at grazing incidence onto a microchannel plate (15 mm $\times$ 75 mm) detector coupled to a phosphor screen, where the image was captured by a charge-coupled device camera. The spectrometer and detection system were designed to capture high harmonics from about 17 eV onwards. Also, since the sensitivity of high harmonic spectroscopy is in general high in the plateau and cut-off region of the harmonic spectrum we do not record the low photon energy region. The spectrometer was calibrated by measuring the transmitted spectrum after an aluminum filter and the position of the Cooper minimum in Argon (appendix A).

The intensity of the laser beam was calibrated by monitoring the cutoff harmonics from harmonic emission in Ar and Xe. This calibration was validated by measuring saturation intensities of gas using a fast ionization gauge similar to that discussed in section 3.2 and shown in Fig. 3.2.

Chapter 4

Sensitivity of High-order Harmonic Generation to Aromaticity

Aromaticity is one of the most important concepts in chemistry and was first introduced to account for the special stability exhibited by benzene. This stability and other unique aspects observed in a large class of cyclic organic molecules can be considered to be a manifestation of cyclic electron delocalization. Approaching this concept from a quantitative perspective is still elusive because electron delocalization is not observable, hence it cannot be measured directly. This explains the enormous efforts in recent years to quantify aromaticity from different standpoints. In order to push this long-standing problem further, it is necessary to explore it from new dimensions.

In this chapter, HHG efficiency is connected with the aromatic character in organic cyclic molecules. The chapter begins with a survey of aromaticity and its measures in the first two sections.Then, it is shown in section 4.3 that aromatic molecules compared to

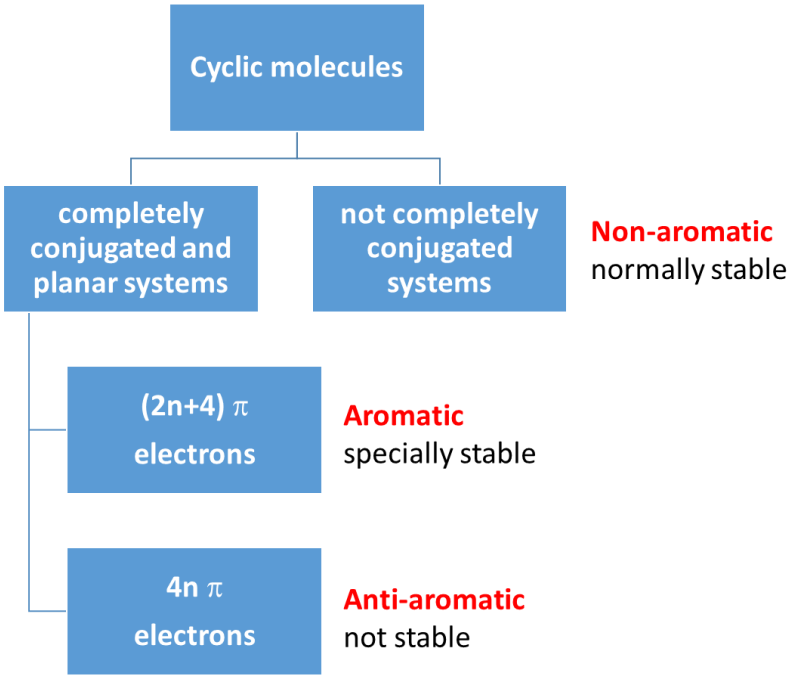

Figure 4.1: A basic classification of cyclic organic molecules with respect to aromaticity.

nonaromatic compounds produce higher HHG yield when interacting with (1825 nm, 50 fs) pulses. Finally, the degree of aromaticity reported by many aromaticity measures is shown to be reflected in the relative yields of plateau harmonics in a chosen set of exemplary aromatic systems. Our numerical calculations show that the highest π molecular orbitals are mainly responsible for the HHG enhancement in aromatic compounds. These results are significant because the HHG yield is a measurable quantity and is directly related to electron delocalization, which arises from π electrons.

4.1 Aromaticity

With respect to aromaticity, cyclic organic molecules fall into three classes: nonaromatic, aromatic, and anti-aromatic (Fig. 4.1). Nonaromatic molecules lack continuous conju-

gation, with no alternation between single and multiple bonds, so their highest orbitals have σ character. On the other hand, the highest occupied orbitals in aromatic and antiaromatic compounds are π orbitals. To understand the origin of this classification, two characteristics of π orbitals need to be recalled:

1. Compared to σ orbitals, π orbitals are bound less strongly to the nucleus, therefore, there is only a slight interaction between π and σ orbitals.

2. In planar cyclic molecules, π orbitals have global symmetry, particularly with respect to the reflection in the plane of the ring.

Given points 1 and 2, Hückel (1930)[43] realized that π orbitals can be treated separately from σ orbitals. As a result, π orbitals are the highest energy orbitals in a completely conjugated cyclic molecule. In this case, the π electrons are not localized in a particular bond, but are delocalized across the whole system. Both aromatic and antiaromatic compounds are delocalized systems but the delocalization in the former leads to stability whereas it results in instability in the latter. The structural stability is determined by the number of π electrons in a molecule. For aromatic molecules, there are $(2n + 4)$ π electrons whereas the number of π electrons in antiaromatic molecules is equal to $4n$ where n is an integer. In Hückel's theory, π orbitals are obtained by considering them as combinations of all participating p_z orbitals (z is the axis normal to the ring plane) in a conjugated system [44]:

$$\psi_i = \sum_{j=1}^{n} c_j \, p_z^j \quad . \tag{4.1}$$

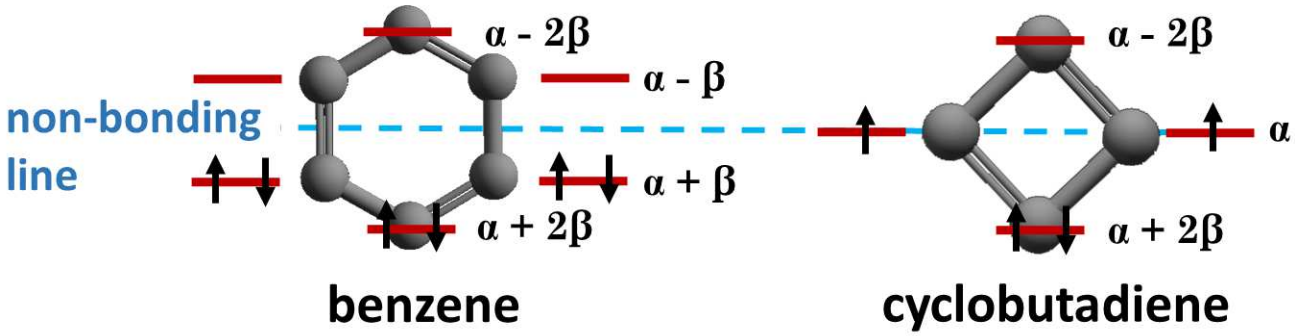

Figure 4.2: Hückel molecular orbitals for benzene and cyclobutadiene.

Eigenvalues corresponding to the energies of the k^{th} π orbital, can be obtained as [44]:

$$E_k = 2\alpha + 2\beta \cos(k\pi/(n+1)) \quad , \tag{4.2}$$

where both α and β are negative parameters. For example, in benzene, there are 6 p_z atomic orbitals that superimpose to form a π electronic system. The number of π electrons in benzene follows Hückel's rule for an aromatic system where ($2\times n+4=6$) with $n = 1$. All the six electrons occupy the lowest three resultant molecular orbitals which are below the non-bonding line (Fig. 4.2), thus benzene is energetically stable. This stability is calculated to be higher than expected for a hypothetical benzene molecule with three unconjugated double bonds. On the other hand, cyclobutadiene has ($4\times n=4$) π electrons, where $n = 1$. These electrons occupy three orbitals, two of which are on the non-bonding line as shown in Fig. 4.2. As a result, cyclobutadiene is unstable and is considered antiaromatic.

Although the Hückel treatment presents a useful qualitative picture of aromaticity in the context of monocyclic organic molecules, it is too approximate to accommodate aromatic polyclic molecules and emerging concepts such as σ aromaticity, three dimensional

aromaticity, Mobius aromaticity and all-metal aromaticity. A recent and increasingly acceptable definition of aromaticity introduced in [45] states: "Aromaticity is a manifestation of electron delocalization in closed circuits, either in two or in three dimensions. This results in energy lowering, often quite substantial, and a variety of unusual chemical and physical properties".

Most known aromatic molecules, including all those studied in this thesis, can be identified through the following unique features: (1) they are cyclic and planar, (2) they follow Hückels rule for the number of π electrons, and (3) each atom in the molecule is sp^2 hybridized, which means that the atomic p orbitals have a certain s character.

4.2 Aromaticity measures

While aromaticity is widely used as a qualitative concept in chemistry to understand the behaviour and structure of cyclic molecules, quantifying the degree of aromaticity of a molecule is challenging due to the lack of direct evaluation methods [46]. Measures introduced in the literature to quantify aromaticity are based on energetic, structural, magnetic and electronic properties, such as:

1. **Nucleus independent chemical shift (NICS)** [47, 48] is the most widely utilized computational measure of aromaticity. It calculates the absolute magnetic shielding at some point near or at the center of the ring. There are several versions of this index such as NICS(0), NICS(0.5) and NICS(1), where the numerical parameters denote the position of the point of interest in Ångstroms above the center of the ring. The

more negative the NICS values, the more aromatic the system.

2. **Ring-current diamagnetic susceptibility (χ_G):** In the presence of an external uniform magnetic field, the ring can sustain induced diamagnetic current which is related to cyclic delocalization of the π electrons. This response is quantified by employing the diamagnetic susceptibility (χ_G) measure [49]. An aromatic compound displays a larger diamagnetic susceptibility compared to a reference model with localized bonds.

3. **Harmonic oscillator model of aromaticity (HOMA)** [50][51] is the most common geometric measure of aromaticity which focuses on the tendency of aromatic molecules to display bond-length equalization. The HOMA value for a system with n bonds can be expressed as:

$$\text{HOMA} = 1 - (\alpha/n) \sum_{j=1}^{n} (R_{opt} - R_j)^2 \quad , \tag{4.3}$$

where α is an empirical constant evaluated to give HOMA=0 for a model nonaromatic system, and HOMA=1 for a system with each bond length R_j is equal to an optimal value R_{opt}. The higher the HOMA value the more aromatic the molecule.

4. **Aromatic stabilization energy (ASE):** This energy-based measure of aromaticity relies on the stability of the π electron systems [52]. From a historic perceptive, this stability is the cornerstone of the notion of aromaticity. The ASE is evaluated as the reaction energy in equations known as homodesmotic schemes. Other energetic measures, such as the enhanced resonance energies, can be calculated using different

reaction schemes.

There are also other interesting schemes that link aromaticity to measurable observables based on molecular response properties, such as electric polarizabilities and hyperpolarizabilities and nuclear magnetic shieldings [53]. Different computational and experimental approaches to measure aromaticity can lead to a different ordering of aromatic molecules [54, 55]. This disagreement is due to the presence of competing effects beside electron delocalization that can influence the results of these methods. Moreover, the same measure could lead to different predictions depending on the computational methods employed. It is therefore essential to analyze aromaticity from different perspectives and extend it to newly explored dimensions for a better understanding of this subject.

4.3 Relative enhancement of HHG in aromatic molecules

Here we address the question: what is the influence of cyclic electron delocalization on HHG?. Using short pulses and longer driving wavelengths, we produce and compare high harmonics in aromatic and nonaromatic molecules that have the same ring size and a similar atomic structure. We limited our comparative study to molecules sharing the same ring size in order to minimize any geometrical effects. Also most measures of aromaticity are affected by the molecular size making it difficult to compare molecules with different ring sizes [56]. In both six- and five-membered ring molecules we show that the HHG yield in aromatic molecules is up to an order of magnitude higher than in non-aromatic molecules.

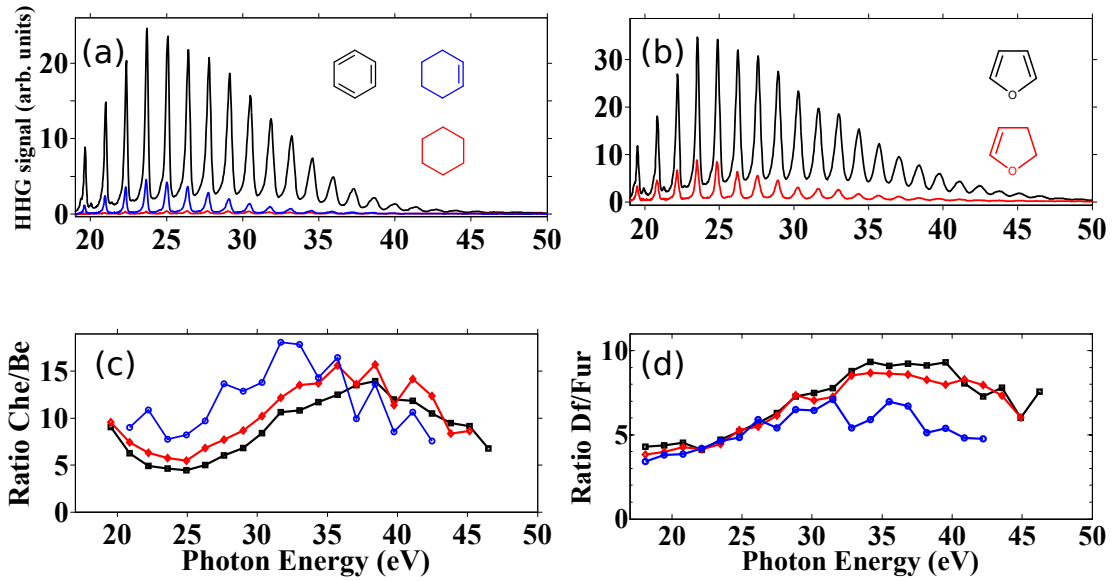

Figure 4.3: HHG spectra for (a)benzene (black), cyclohexene (blue) and cyclohexane (red) obtained using 1825 nm light at an intensity of 6.5×10^{13} W/cm^2. (b) For furan (black) and 2,3-dihydrofuran (red) obtained using 1825 nm light at an intensity of 4.5×10^{13} W/cm^2. (c), (d) cyclohexene-to-benzene signal and 2,3-dihydrofuran-to-furan signal at three different intensities; 4.5 (blue circle), 6.5 (red diamond) and 8.6 (black square) in units of 10^{13} W/cm^2.

Benzene is emblematic of an aromatic system and is ranked as the most aromatic molecule according to most measures. For example, the HOMA value of benzene is unity which indicates that all bonds are equal in length. So, we compare the harmonic yields of benzene (C_6H_6) with nonaromatic molecules cyclohexene (C_6H_{10}) and cyclohexane (C_6H_{12}) that belong to the same family of six-membered rings, as shown in Fig. 4.3(a). All three molecules have approximately similar ionization potentials (9.25 eV, 8.94 eV and 10.32 eV, respectively [57]) and the harmonics are produced at 1825 nm and an intensity of 6.5x10^{13} W/cm^2 and identical pressures in the gas cell. The harmonic signal from benzene is greater by a factor of 8 and 20 compared to cyclohexene and cyclohexane, respectively. Fig. 4.3(c) shows the ratio of harmonic signal from benzene to that of cyclohexene as a function of harmonic energy for 3 different intensities. Although the ratios are different in magnitude, their dependence on harmonic order is similar, indicating that significant

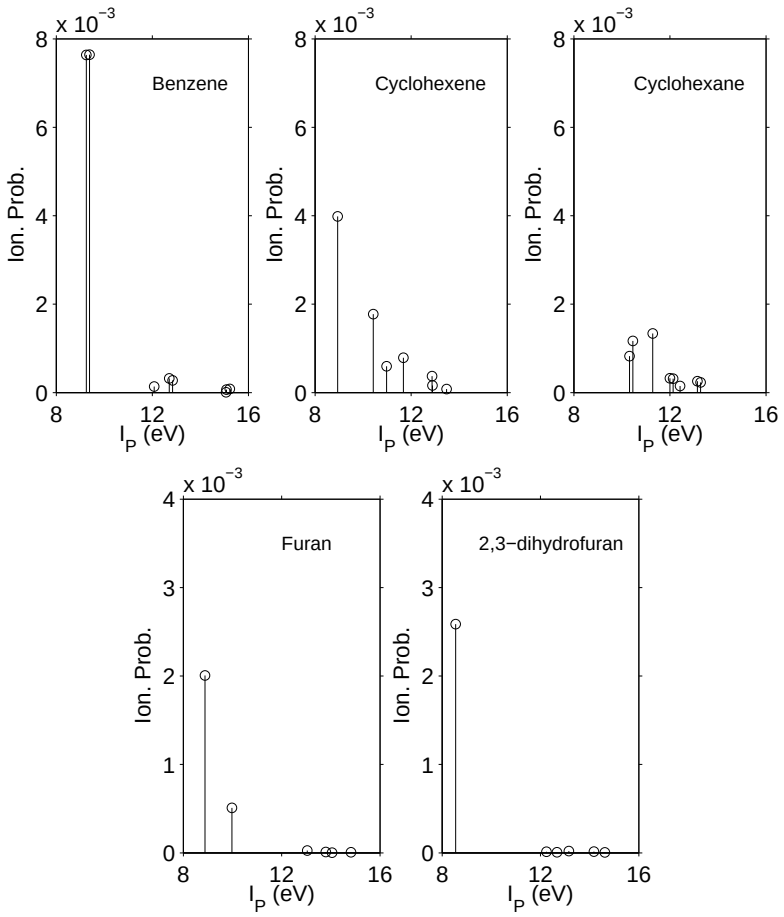

Figure 4.4: Top row: Half-cycle ionization probabilities for the lowest eight cation states of benzene, cyclohexene and cyclohexane at an intensity of 6.5×10^{13} W/cm^2. (Note: A small shift of 0.1 eV was added to one component of the degenerate states in benzene and cyclohexane to help make these states distinguishable in the plots.) Bottom row: Half-cycle ionization probabilities for the lowest few cation states of furan and 2,3-dihydrofuran at an intensity of 4.5×10^{13} W/cm^2. Probabilities were calculated for a laser wavelength of 1825 nm.

differences are present between aromatic and nonaromatic molecules over a large range of laser intensities. While the ratio for lower order harmonics varies with intensity, it is nearly independent for plateau and cut-off harmonics. Previous studies on HHG in benzene and cyclohexane [31] using a 800 nm driving field with 70 fs and 240 fs pulses only produced lower order harmonics with the harmonic yield of benzene higher by a factor of 2-4 than that of cyclohexane.

To ensure that higher high-harmonic yields in aromatic molecules are universal, we

studied HHG in five-membered ring molecules. Fig. 4.3(b) shows the harmonic spectrum for aromatic furan (C_4H_4O) and nonaromatic 2,3-dihydrofuran (C_4H_5O) at 1825 nm and an intensity of 4.5×10^{13} W/cm^2. These two molecules have ionization potentials of 8.88 eV and 8.55 eV respectively [58]. Fig. 4.3(d) shows their ratio for different intensities. The harmonic signal in furan is up to an order of magnitude higher than its nonaromatic counterpart and the ratio is nearly independent of laser intensity over the entire harmonic range except for the lowest intensity where the ratio decreases for high energy photons.

To further understand the origin of the HHG yield enhancement in aromatic molecules, we performed time-dependent numerical calculations of the SFI yields from different molecular orbitals. We calculated the half-cycle SFI, which reflects the sub-cycle SFI yields that are relevant to the first step of the sub-cycle HHG process. Computations are carried out using the time-dependent resolution-in-ionic-states (TD-RIS) method outlined in Ref. [59]. The top row of Fig. 4.4 shows the half-cycle SFI probabilities for ionization to the lowest cationic states of benzene, cyclohexene and cyclohexane. The highest occupied molecular orbital (HOMO) of benzene is a π orbital and is doubly degenerate. The first two channels in benzene corresponding to HOMO ionize significantly compared to other channels and contribute coherently to HHG. In cyclohexene and cyclohexane, ionization is lower than in benzene and occurs from multiple orbitals.

From our calculations, the total ionization yield (summation over the yield for all the cationic channels of each molecule) of benzene is $\sim$2 and $\sim$3.5 times larger than the total yields of cyclohexene and cyclohexane, respectively. This is in agreement with previous observation of saturation intensities (a measure of the ionization efficiency) for benzene

and cyclohexene [60]. Also, the relative photoionization cross section for cyclohexane was found to be 15% of benzene at 780 nm [61]. The observed differences in numerical ionization yields will translate to an even higher difference in the HHG signal when the recombination step and dynamical interferences from multiple orbitals in cyclohexene and cyclohexane are taken into account [33]. This suppression effect in the case of multiple active HHG channels will be common to HHG in all complex molecules involving closely spaced multiple orbitals.

The bottom two panels in Fig. 4.4 show the ionization probability in the five-membered ring molecules furan and 2,3-dihydrofuran. Differences in ionization exist but are not as profound as in six-membered ring molecules. The total ionization probabilities for the two species are essentially equal. In furan, HOMO-1 contributes by about 20% to the total ionization whereas in 2,3-dihydrofuran no orbital other than the HOMO contributes to ionization. However, the fact that experimental harmonic yields in furan are a factor of 4-10 higher than 2,3-dihydrofuran over a range of harmonics suggests that, on a quantitative level, the recombination step plays a significant role in the observed harmonic yields.

4.4 HHG as a measure of aromaticity

We now focus on the differences in the HHG yield among aromatic molecules to see how they could be connected to the degree of aromaticity. To minimize the influence of other factors, we compare the HHG in furan (C_4H_4O), pyrrole (C_4H_4NH) and thiophene (C_4H_4S). These three molecules are considered to be the archetype of five-membered heteroaromatic compounds and they all share similar geometric, atomic and electronic structures. They

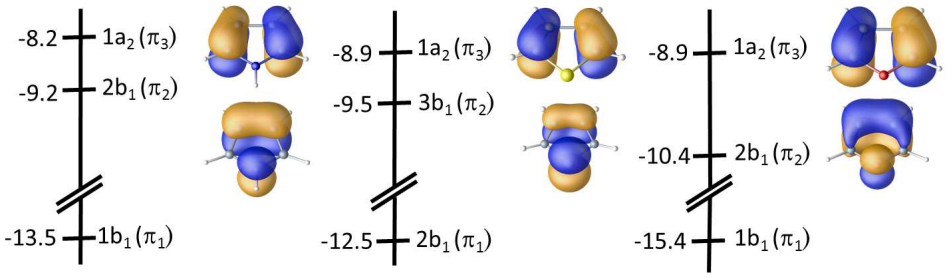

Figure 4.5: Experimental binding energies for π molecular orbitals of pyrrole (left), thiophene (middle) and furan (right) [62]. The Dyson orbitals corresponding to the two highest ionization channels are also shown.

have comparable ionization potentials of 8.88, 8.20 and 8.86 eV [58], respectively. There are six π-electrons in these aromatic molecules, one from each carbon atom and two from the unshared pair on the heteroatom. The first two occupied π orbitals (π_3 and π_2) represent HOMO and HOMO-1 (Fig. 4.5). These orbitals have the same general shape in all three molecules but differ slightly in their localization properties. The lowest lying π_1 orbital represents HOMO-4 in pyrrole, HOMO-3 in thiophene, while it is HOMO-6 in furan. According to most descriptors of aromaticity, furan is least aromatic among the three molecules. However, between thiophene and pyrrole there is no consensus on which of these molecules is more aromatic. ASE and χ_G [55] measures consider pyrrole to be more aromatic than thiophene whereas according to NICS(1)[63] measure thiophene is more aromatic. Other versions of NICS [45, 56] indicate a classification that agrees with ASE and χ_G. On the other hand, the HOMA[55] index gives comparable values for both molecules.

Fig. 4.6(a) shows the ratio of the harmonic signal of pyrrole to furan for three different intensities at 1825 nm. A ratio of unity indicates both molecules have the same harmonic yields. At the lowest intensity of 2.5×10^{13} W/cm^2, the harmonic signal in pyrrole is higher

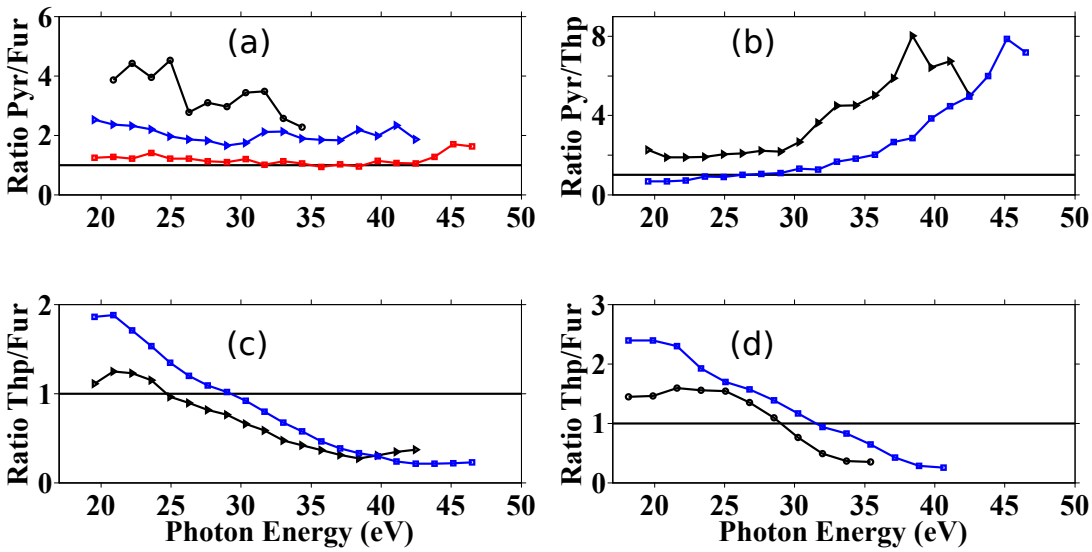

Figure 4.6: Ratio of harmonic signals. (a) Pyrrole to furan using 1825 nm at 3 different laser intensities 2.5 (black circle), 4.5 (blue triangle) and 6.5 (red square) in units of 10^{13} W/cm^2. (b) pyrrole to thiophene, and (c) thiophene to furan using 1825 nm at 2 different laser intensities 4.5 (black triangle) and 6.5 (blue square) in units of 10^{13} W/cm^2. (d) Thiophene to furan using 1430 nm at 2 different laser intensities 4.5 (black diamond) and 6.5 (blue circle) in units of 10^{13} W/cm^2.

by a factor of 3-4. The ratio decreases for higher order harmonics close to the cut-off. The high fluctuations of the ratio are due to the low harmonic signal as a result of low gas densities (restricted by the low vapour pressure of pyrrole) and laser intensity. At higher intensities, the ratio remains nearly constant for both plateau and cutoff harmonics. However, the ratio decreases with intensity since pyrrole ionizes faster and reaches saturation at lower intensities than furan. Saturation in pyrrole occurs at $\sim 6 \times 10^{13}$ W/cm^2 while in furan it occurs at $\sim 10^{14}$ W/cm^2.

Fig. 4.6(b) shows the ratio of the harmonic signal of pyrrole to thiophene for two different intensities at 1825 nm. At an intensity of 4.5×10^{13} W/cm^2, the pyrrole signal is a factor of two higher than thiophene for lower harmonics. At a higher intensity of 6.5×10^{13} W/cm^2, lower-order harmonics in the recorded spectra for both molecules produce a similar

Compound	HHG	ASE	χ_G	NICS(1)	HOMA
Pyrrole	1	1	1	2	1
Thiophene	2	2	2	1	1
Furan	3	3	3	3	3

Figure 4.7: Ranking of pyrrole, thiophene and furan molecules with respect to aromatic character according to HHG, ASE [55], χ_G [55], NICS(1) [63] and HOMA [55]. Rank 1 denotes the most aromatic molecule.

harmonic signal but pyrrole starts to dominate for the rest of plateau harmonics. At both intensities, the ratio increases beyond 30 - 35 eV. A possible explanation for this decline in the thiophene signal can be linked to the presence of a Cooper minimum. In appendix A, we showed that the HHG spectra of molecules containing atoms such as sulfur can exhibit a Cooper minimum at around 42 eV. In thiophene spectra, the minimum cannot be clearly observed because it is close to the cutoff harmonics, which are relatively lower due to a low ionization potential. However, it could significantly weaken the already decaying signal.

Fig. 4.6(c) and (d) show the ratio of the harmonic signal of thiophene to furan at 1825 nm and 1450 nm, respectively, for two different intensities. At 4.5×10^{13} W/cm^2, only the lower plateau harmonics have higher yields in thiophene compared to furan. At a higher intensity (6.5×10^{13} W/cm^2), thiophene domination extends to higher plateau harmonics, however, closer to the potential Cooper minimum the harmonic signal from furan is higher at all intensities. This behaviour is wavelength independent.

Our results on high harmonic yields in five-membered aromatic molecules suggest pyrrole to be more efficient at producing plateau harmonics, followed by thiophene and then furan. This ordering agrees with many aromaticity measures such as ASE and diamagnetic susceptibility χ_G (Fig. 4.7). To confirm our findings, we calculated the ionization

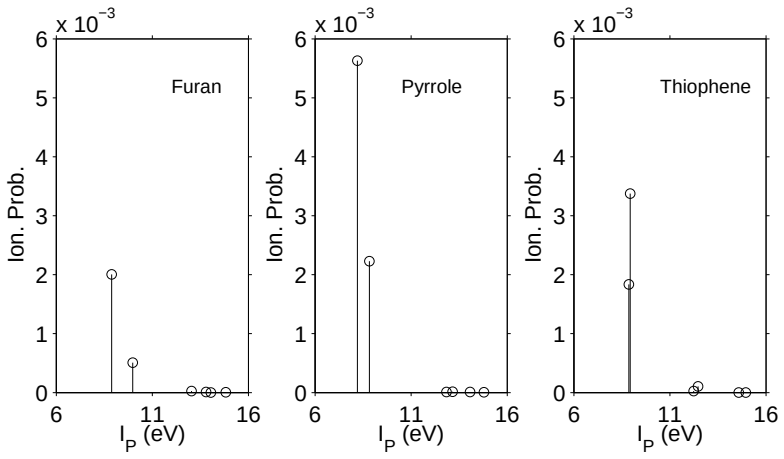

Figure 4.8: Ionization probabilities for the calculated lowest six cation doublet states of furan, pyrrole and thiophene using 1825 nm laser pulses at an intensity of 4.5×10^{13} W/cm^2 over a period of a half laser cycle.

probabilities of the highest orbitals in all three molecules as shown in Fig. 4.8. A common signature of all three aromatic molecules is that essentially all of the sub-cycle ionization comes from the highest two π orbitals. In pyrrole, ionization from HOMO is dominant with about 30% of the total ionization yield coming from HOMO-1. The total ionization of pyrrole is three times that of furan. The observed differences in ionization of pyrrole and furan are in reasonable agreement with the experimental harmonic yields shown in Fig.4a. In thiophene, HOMO-1 is the dominant channel, with HOMO contributing only 35% of the total ionization yield. In furan, ionization from HOMO is a factor of four larger than that of HOMO-1. The total ionization yield for thiophene is two times larger than the total yield for furan which reflects the observed harmonic yields without invoking the recombination step except for the harmonics closer to the cutoff in thiophene as discussed earlier.

4.5 Conclusion

We conclude that the efficiency of producing high harmonics in organic cyclic molecules is sensitive to aromaticity which could add more insight to the understanding of this subject. The observed link between aromaticity and HHG can be understood from the fact that the highest π orbitals are mainly responsible for the enhanced HHG emission in aromatic molecules. This property is remarkable since several existing aromaticity measures cannot decouple the contribution of σ orbitals from the description of aromaticity [45, 64]. However, the HHG process does not probe the entire π molecular orbital system and is influenced by other factors such as multiorbital effects and electronic structure. As a result, it cannot be used to characterize aromaticity conclusively. Similar limitations were also observed in many well-known approaches to study aromaticity, such as HOMA. For example, it was shown that some nonaromatic cyclic compounds and many acyclic systems have bond-length equalized structures[45]. Although this study established the connection between the two subjects, aromaticity and HHG, it is important to examine this relation further by exploring a larger variety of molecular systems, as discussed in chapter 8.

Chapter 5

Femtosecond Laser Spectroscopy of Xylene Isomers

Structural isomers are optimal objects to probe how the interaction of intense femtosecond-laser pulses with molecules could vary with very small changes in the molecular structure. However, many isomers with cyclic structure, especially xylenes, are hard to identify and are known to exhibit virtually indistinguishable mass spectra when interacting with transform-limited femtosecond laser pulses. In this chapter, differences in the electronic response of xylene isomers to transform limited femtosecond pulses are identified by (i) probing doubly charged ions with circularly polarized 800 nm light, and (ii) generating high-order harmonics with 1430 nm and 1850 nm light. First, the yield of doubly charged o-xylene is shown to decrease while doubly charged p-xylene increases over a range of laser intensities when the laser polarization is changed from linear to circular. This opposite behaviour in the two isomers enhances their distinction by a factor of two for circularly po-

larized light. It is also found that the yield of high-order harmonics depends on the specific positioning of the methyl group in xylene isomers (o-,p- and m-xylene). Numerical results attribute the observed differences in the three isomers to the strength of tunnel ionization and the overlap between the angular peaks of ionization and photo-recombination.

5.1 Background

Interaction of intense femtosecond laser pulses with molecules leads to rich and complex dynamics often involving competing phenomena such as ionization, dissociation, molecular alignment, high-order harmonic generation and Coulomb explosion. Fundamental insight into the complex dynamics can be obtained by investigating how the interaction responds to systematic variations in the molecular arrangement. Structural isomers -molecules having same chemical formula but atoms arranged differently in 3D space serve as good targets for such investigations. Moreover, such comparative studies have a fruitful applied role in analytical chemistry where the distinction of isomers is a major task. Besides their temporal and spatial features, femtosecond-laser-pulses based techniques have advantages over most other spectroscopic techniques in identifying isomers due to the ability to control a wide range of pulse characteristics and to observe all subsequent effects on the different products of the interaction.

Xylene isomers, especially p-xylene and o-xylene, are known to produce almost indistinguishable mass spectra when interacting with transform-limited femtosecond pulses (Fig. 5.1a). Therefore they have been exploited in the literature as a benchmark for testing the capability of new femtosecond laser-based spectroscopic methods.

Dela Cruz *et al.* [65] developed a method to identify isomers based on femtosecond laser pulse shaping. In their approach, the frequency spectrum of the pulse was divided into 10 different groups, and a phase retardation equal to 0 or π was assigned to each group. It was found that a certain binary phase can lead to the production of different relative yields of the ion $C_7H_7^+$ from o- and p-xylene molecules.

Another scheme was proposed by Urbasch *et al.* [66] that exploited the time domain of the pulse, instead of the frequency domain. Compared to Dela Cruz's work and the current study, the range of pulse energies employed in Urbasch's study was capable of generating significant yields of small fragments like C^+. It was found that these light ions are produced differently in the two isomers and the differences can be amplified by varying the pulse chirp up to 1000 fs^2.

It is of fundamental interest to explore how purely electronic excitations differ in these molecules by monitoring the production of intact ions or emitted photons by a strong laser field without manipulating the spatio-temporal profile of the femtosecond pulses which makes the understanding of the underlying physics less straightforward.

5.2 Femtosecond-laser mass spectroscopy of xylene isomers

In this section, we show that monitoring the doubly charged parent ion yield enables better differentiation of the o- and p-xylenes instead of singly charged molecular and fragment ions. Fig. 5.1a shows the mass spectrum of o-xylene for linearly polarized 800-nm,49-fs

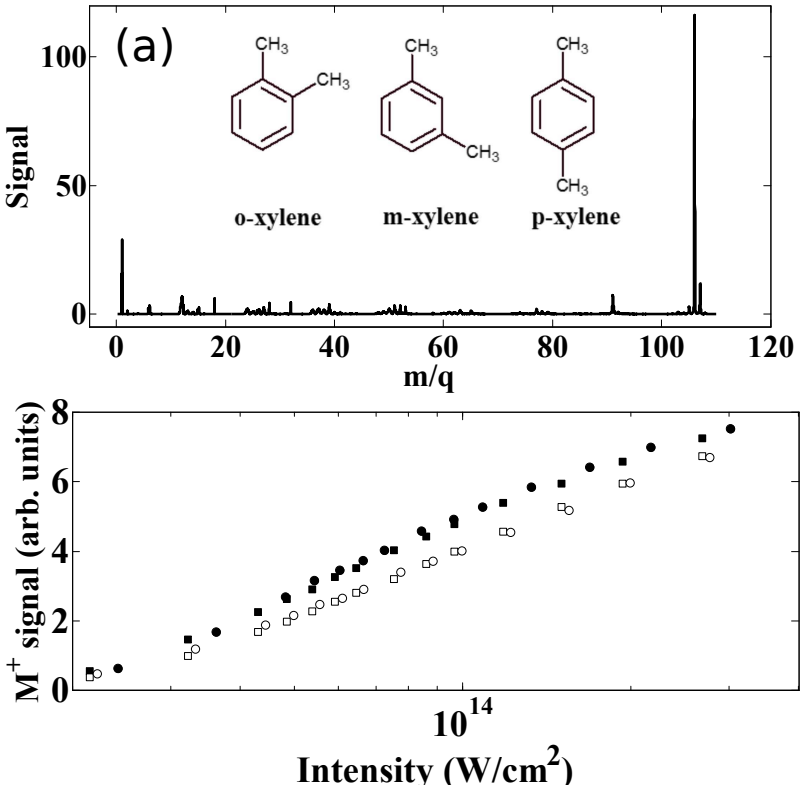

Figure 5.1: a) Time-of-flight mass spectra of o-xylene at 800 nm and laser intensity of 1x10^{14} W/cm^2. The structures of the three xylene isomers are also shown. b) Intensity dependence of singly charged ions: o-xylene (solid symbols) and p-xylene (open symbols) for linear polarization (squares) and circular polarization (circles). The intensity axis of the yields for circular polarization was shifted in both plots by a factor of 0.74 and 0.68 for o-xylene and p-xylene respectively (see discussion).

pulses at an intensity of 10^{14} W/cm^2, dominated by the parent ion. The mass spectrum of p-xylene is nearly identical making it difficult to differentiate (not shown). The inset of Fig. 5.1a is a schematic of the three xylene isomers.

The intensity variation of the singly charged parent ion for both o- and p-xylene is shown in Fig. 5.1b, obtained with linear (squares) and circular (circles) laser polarization and similar concentrations in the interaction volume. For a given intensity, the yields for circular polarization are lower for both molecules. So, to obtain similar yields for both laser polarizations, the intensity scale for circular polarized light was adjusted in Fig. 5.1b by a factor of 0.74 (0.68) for o-xylene (p-xylene) yield.

The scaling factor arises from two opposing effects as as discussed in [67] for an atom. First, the electric field is always on for circularly polarized field leading to a higher cycle-average tunnelling compared to linearly polarized light with the same electric field. On the other hand, the electric field is lower for circular polarization for the same value of the pulse energy by a factor of $1/\sqrt{2}$. We measured the scaling factor in Xe to be 0.65 in good agreement with the published value [67][68]. Higher scaling factors in xylenes compared to Xe highlights the differences in tunnel ionization among different species. The key result of Fig. 5.1b is that the yield of o-xylene is slightly higher than p-xylene. This is in good agreement with the numerical simulation of the total ionization probability discussed later.

We now focus on formation of doubly charged o- and p-xylene and their polarization dependence. Fig. 5.2(a,b) shows the low m/q portion of the mass spectra corresponding to doubly charged o- and p-xylenes for linear and circular polarization, respectively. The peak at m/q=53 corresponds to doubly charged parent ion with some contribution from

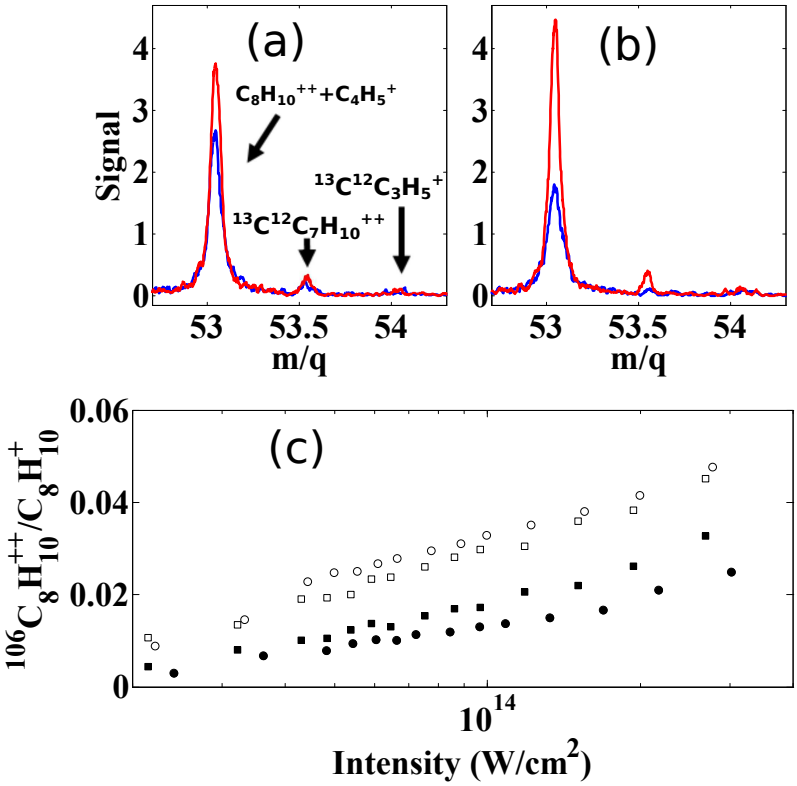

Figure 5.2: Time-of-flight mass spectra of p-xylene (red) and o-xylene (blue) at laser intensity of 1x10^{14} W/cm^2 for (a) linearly and (b) circularly polarized 800 nm light. Only the portion of spectra containing the signals of doubly charged ions are shown. (c) Intensity dependence of doubly charged ions: o-xylene (solid symbols) and p-xylene (open symbols) for linear polarization (squares) and circular polarization (circles). The intensity axis of the yields for circular polarization was shifted in both plots by a factor of 0.74 and 0.68 for o-xylene and p-xylene respectively.

$C_4H_5^+$ fragment. The peak at 53.5 corresponds to the doubly charged molecular isotope $^{13}C^{12}C_7H_{10}$. Comparison of the measured isotopomer ratio with known value of 8.9% suggests there is less than 25% contribution of the molecular fragment at $m/q = 53$. This is further evident from the similar behaviour of ion signals at m/q=53 and 53.5 for linearly and circularly polarized light.

Fig. 5.2(c) shows the intensity variation of doubly charged ions of o-xylene (solid symbols) and p-xylene (open symbols) for linear (squares) and circular (circles) polarizations. The intensity scales for circular polarization were adjusted by the appropriate factors discussed above. The normalized doubly charged ion yields reveal two key features. First, it is enhanced in p-xylene despite the fact that singly charged ion yield is lower compared to o-xylene. Second, when the polarization is changed from linear to circular it is reduced in o-xylene whereas it remains the same or slightly increases in p-xylene. This behaviour can be understood in terms of the relative contribution of sequential and non-sequential double ionizations, which can be differentiated by changing the laser polarization. For linear polarization both processes are present whereas for circular polarization non-sequential double ionization, which is a consequence of the electron recollision process, disappears. The opposite behaviour of the observed results in Fig. 5.2(c) suggest a larger contribution of non-sequential double ionization in o-xylene relative to p-xylene. Also, for circular polarization contribution of sequential double ionization in p-xylene is higher than o-xylene.

The different polarization dependences of the two isomers enables their distinction by using transform-limited pulses. Fig. 5.3 shows the ratio of normalized doubly charged ion

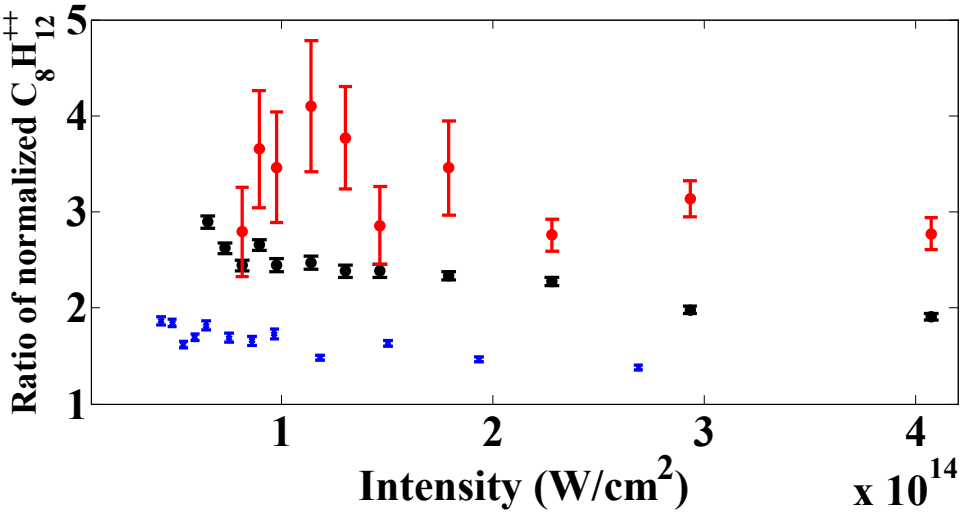

Figure 5.3: The ratio of p-xylene doubly charged signal at m/q=53 to that of o-xylene at 800 nm for linear polarization (blue solid squares) and circular polarization (black solid circles). Also is shown the same ratio for the isotope signal at m/q=53.5 for circularly polarized light (red circles).

yields of p-xylene to that of o-xylene for linear (squares) and circular (circles) polarizations at different intensities without any scaling. For linear polarization, the ratio is ∼1.5 but is enhanced for circular polarization. The differences are more pronounced when isotopes are considered (open circles in Fig. 5.3) due to the absence of fragment contribution.

5.3 HHG in xylene isomers

We now present a second approach that can distinguish isomers by monitoring the emission of light (instead of molecular ions and fragments) through the generation of high-order harmonics (HHG) [11] produced when an ionized electron returns to the parent ion and undergoes recombination. The kinetic energy of the recolliding electron during the recombination process is transformed to photons that carry information on the molecular structure and dynamics. Previously, our group demonstrated that HHG in randomly ori-

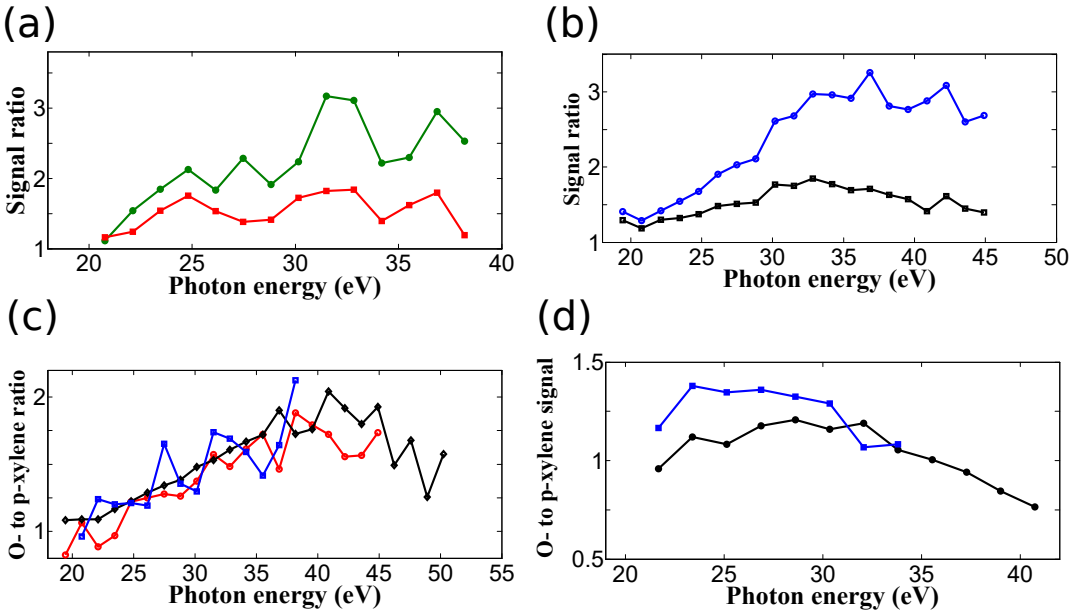

Figure 5.4: HHG yield ratios of o-xylene(green circles) and p-xylene (red sqaures) with respect to m-xylene at 1850 nm and intensities of (a) 6×10^{13} W/cm^2 and (b) 1.1×10^{14} W/cm^2. c) HHG yields ratios of o-xylene to p-xylene at 1850 nm for three laser intensities 6×10^{13} W/cm^2 (red circles), 8×10^{13} W/cm^2 (blue squares) and 1.1×10^{14} W/cm^2 (black diamonds). d) HHG yields ratios of o-xylene to p-xylene at 1430 nm for two laser intensities 5×10^{13} W/cm^2 (blue squares) and 8×10^{13} W/cm^2 (black circles).

ented stereoisomers produced distinctly different harmonic spectra due to differences in ionization and recombination [69, 70]. It is therefore interesting to extend this to structural isomers, especially those with small differences in the position of a functional group like xylenes.

5.3.1 Relative HHG yields in xylene isomers

Fig. 5.4(a-b) shows the relative HHG yield for o-xylene and p-xylene with respect to m-xylene with 1850 nm pulses (transform-limited with a pulse duration of ∼70 fs) at two laser intensities of 6×10^{13} W/cm^2 and 1.1×10^{14} W/cm^2 respectively. First, the harmonics from m-xylene are always lower than o- and p-xylene, as a result the ratios are greater than

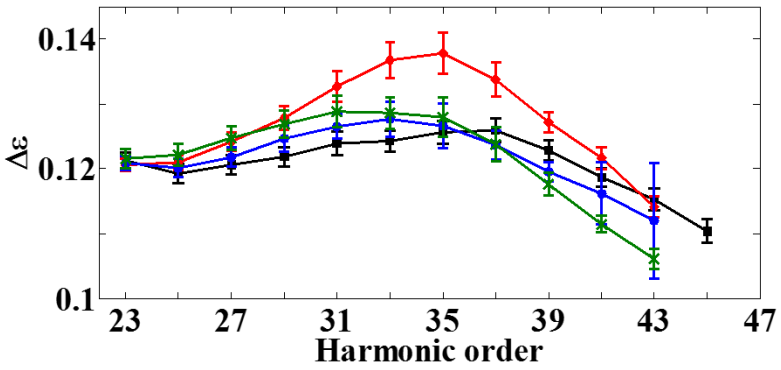

Figure 5.5: The ellipticity width $\Delta\epsilon$ as a function of harmonic order for benzene (black), p-xylene (green), o-xylene (blue) and m-xylene (red) at a laser intensity of 6×10^{13} W/cm^2 and wavelength of 1430 nm.

unity. Results suggest o-xylene can be distinguished from p- and m-xylenes. Although the differences between p-xylene and m-xylene are small, we found they are always present and reproducible at various laser intensities and wavelengths and at different gas pressures. Second, harmonic yield from o-xylene is higher than p-xylene and this difference increases progressively from low to high-order harmonics. Fig. 5.4 (c) shows that this behaviour is the same at three different laser intensities of 6×10^{13} W/cm^2 (blue), 8×10^{13} W/cm^2 (red) and 1.1×10^{13} W/cm^2 (black). The distinction between the two isomers differs by a factor of 1.5 to 2 for higher-order harmonics. Also shown in Fig. 5.4 (d) is the ratio for 1430 nm pulses (transform-limited with a pulse duration of 70 fs) at two laser intensities of 5×10^{13} W/cm^2 (blue) and 8×10^{13} W/cm^2 (black). For both intensities, the signal of the lower order harmonics from o-xylene is higher than p-xylene. At the higher intensity, the opposite behaviour occurs for higher-order harmonics. With the ratio remaining close to unity it therefore makes it more difficult to differentiate the two isomers at 1430 nm compared to the longer wavelength.

To gain further insight into the dependence of the HHG process on the molecular

structure, we studied the dependence of high harmonic yields in Xylene isomers on driving field ellipticity at 1430 nm and compared to benzene as shown in Fig. 5.5. Benzene is the building block of the xylene isomers where two additional methyl groups are attached to the ring in different locations. The experimental data were fitted with Gaussian profiles then we extracted half widths at half maximum and plotted them as a function of harmonic order. The errors represent 95% confidence interval of the Gaussian fits.

The response of m-xylene to elliptically polarized field is weaker compared to other molecules. There are two striking features: (i) Ellipticity dependence is relatively strong for lower and cutoff harmonics and is weak around 35^{th} harmonic. For atoms, $\Delta\epsilon$ is known to decrease (increase) monotonically for short (long) trajectories. Under similar conditions, ellipticity dependence of Xe exhibited (not shown) a decrease in $\Delta\epsilon$ with harmonic order. (ii) Around 35^{th} harmonic, p- and o- xylenes undergo a transition from weaker to stronger ellipticity dependence relative to benzene. There also appears to be a similar transition between p- and o-xylenes with $\Delta\epsilon$ being larger (lower) in p-xylene below (above) 35^{th} harmonic. These observations reflect the complexity of HHG process in complex molecules.

5.3.2 Theoretical simulation of HHG in xylene isomers

Xylene isomers are substituted benzene derivatives by two methyl groups. This substitution removes the degeneracy of the two π HOMO orbitals of benzene and somewhat lowers the ionization potential (I_p of benzene =9.25 eV). Fig. 5.6 shows the two highest occupied molecular orbitals and ionization energies for the three xylene isomers obtained by Gaussian quantum chemistry code [71]. For m- and o-xylene, most of the electron density

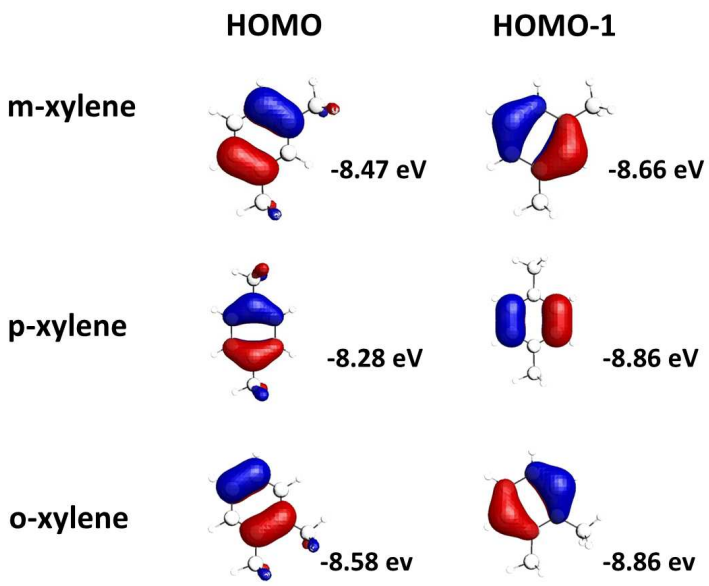

Figure 5.6: Molecular orbitals with corresponding ionization potentials for xylene isomers.

distribution is on the ring and their HOMO's and HOMO-1's have similar shape. In p-xylene, the distribution in the ring for HOMO is similar to the HOMO-1 of m- or o-xylene and vice-versa. Based on the small differences in ionization potential and the shape of these molecular orbitals, one would generally expect ionization and HHG yields from these isomers to be similar. While this expectation is justified for ionization (see Sec.5.2), the experimental HHG ratios, presented in the previous subsection are somewhat unexpected.

Let us first focus on ionization. We have carried out calculations using the strong-field approximation (SFA) [72**?**] within the single-active electron approximation. We used the wavefunctions generated from the Gaussian quantum chemistry code [71] at the Hartree-Fock level with the augmented correlation-consistent polarized valence triple-zeta (aug-cc-pVTZ) basis set. Since the HOMO and HOMO-1 have quite close ionization potentials, well separated from lower molecular orbitals, we only account for these two orbitals in our simulations. Ionization yields from the HOMO and HOMO-1 were added up to obtain the

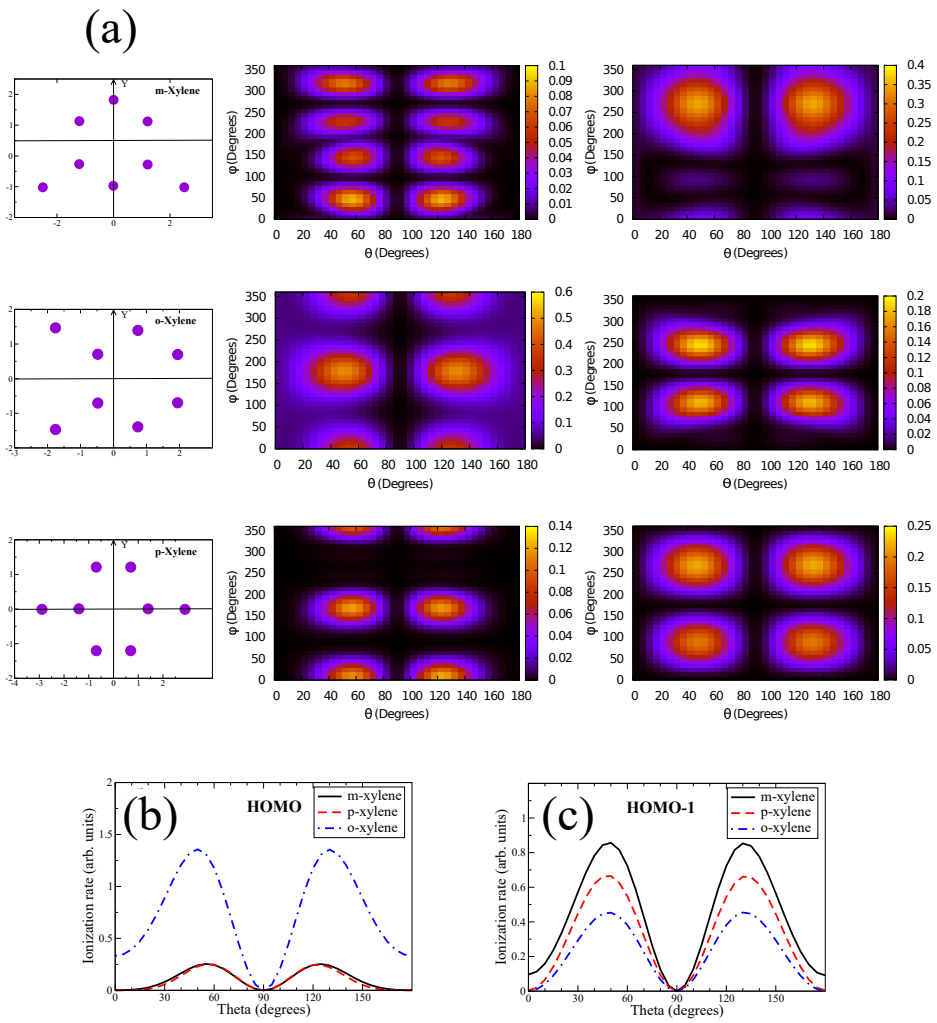

Figure 5.7: (a) Molecular geometry (left panel) angle-dependent ionization from HOMO (middle panel) and HOMO-1 (right panel), for m-xylene (top panel), o-xylene (middle panel) and p-xylene (bottom panel). Here the laser polarization direction is given by polar angle θ and azimuthal angle ϕ, defined in the molecular frames shown in the left column. For clarity, only carbon atoms are shown. (b) and (c): Integrated yield vs polar angle from HOMO and HOMO-1, respectively, for each isomer. All the results here only include electron emission along the laser polarization direction. Light with wavelength of 1850 nm and intensity of 0.8×10^{14} W/cm^2 is used in simulations.

total yield for each isomer, resulting in the ratios of 1 : 0.85 : 0.8 for o-xylene:m-xylene:p-xylene. The calculation were performed with a 3-cycle pulse with the laser intensity of 0.8×10^{14} W/cm^2 and wavelength of 1850 nm. Here we have included the Stark shift correction for the polar molecules (o-xylene and m-xylene), following Refs. [73, 74]. The ratios are virtually unchanged with a half-cycle laser calculation (see below). They only slightly change without the Stark shift correction. Clearly, these results are consistent with the experimental findings in Sec. II. We did not attempt to simulate double ionization here since the calculations are involved.

To understand the origin of our experimental HHG ratios, we calculate high harmonic spectra for these molecules within a single-molecule response approximation using the quantitative rescattering (QRS) theory [75, 76]. Within the QRS, HHG yield for a fixed photon energy and fixed laser direction (or molecular alignment) is proportional to the product of tunneling ionization rate and (differential) photo-recombination cross sections. To compare with experiments, averaging over isotropic molecular alignment distribution has to be carried out. Before presenting calculated HHG results, we now analyze each ingredient that enters the QRS simulations. The actual QRS calculations are done at the level of complex amplitudes. Nevertheless, one can get some qualitative understanding with arguments based on the magnitudes alone (i.e., without the phases), as discussed below.

As stated above, total ionization yields from HOMO and HOMO-1 for xylene isomers differ from one another only by about 20%. However, the angle-dependent ionization yields vary strongly, as shown in Fig. 5.7(a). Here the calculations were performed using the

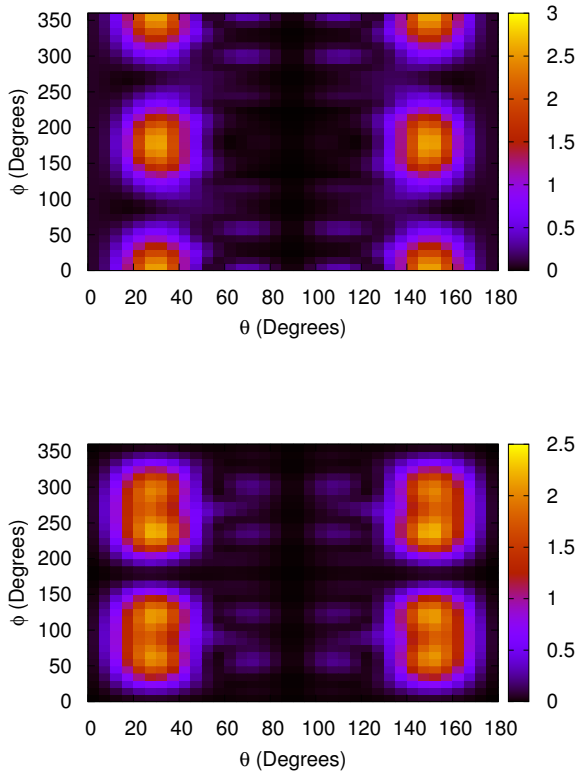

Figure 5.8: O-xylene photoionization cross section vs photon polarization direction at 36 eV for HOMO (a) and HOMO-1 (b). The electron emission is along polarization direction.

Stark-corrected SFA [73, 74] with the laser intensity of 0.8×10^{14} W/cm^2 and wavelength of 1850 nm, but only a half-cycle at the peak of a three-cycle pulse is allowed to ionize the molecules in order to have a definite orientation for the electric field. Furthermore, only electron emission along the laser direction is taken into account. To have a more quantitative idea, we integrate the yield over the azimuthal angle. The results are displayed in Fig. 5.7(b) and 5.7(c) for the HOMO and HOMO-1, respectively. Clearly, ionization from o-xylene is strongest with a dominant yield from the HOMO. For m-xylene and p-xylene, HOMO-1 yields are stronger than the HOMO. We note that for the HOMO, ionization yield peaks near $\theta = 50^\circ$ (and 130°) for o-xylene and near $\theta = 60^\circ$ (and 120°) for the other two isomers. This has strong consequences on the HHG yield, as we will see in the following. Interestingly, the total yield (i.e., with all electron emission directions included), HOMO and HOMO-1 are comparable for m-xylene, whereas HOMO is stronger than HOMO-1 in p-xylene.

As for photoionization (time-reversal of photo-recombination), the cross sections were calculated using ePolyScat package [77, 78]. Differential cross sections for the electron emission along the photon polarization for the three isomers are quite similar in both magnitude and shapes as functions of angles for any fixed energy below about 50 eV, considered in this paper. We therefore only show here in Fig. 5.8 the cross section from o-xylene at photon energy of 36 eV. For the main channel, we note that the cross section for the HOMO has a peak near $\theta = 30^\circ$ (and 150°). This peak position is quite stable with respect to photon energy.

According to the QRS, HHG yield depends on the overlap of ionization rate and pho-

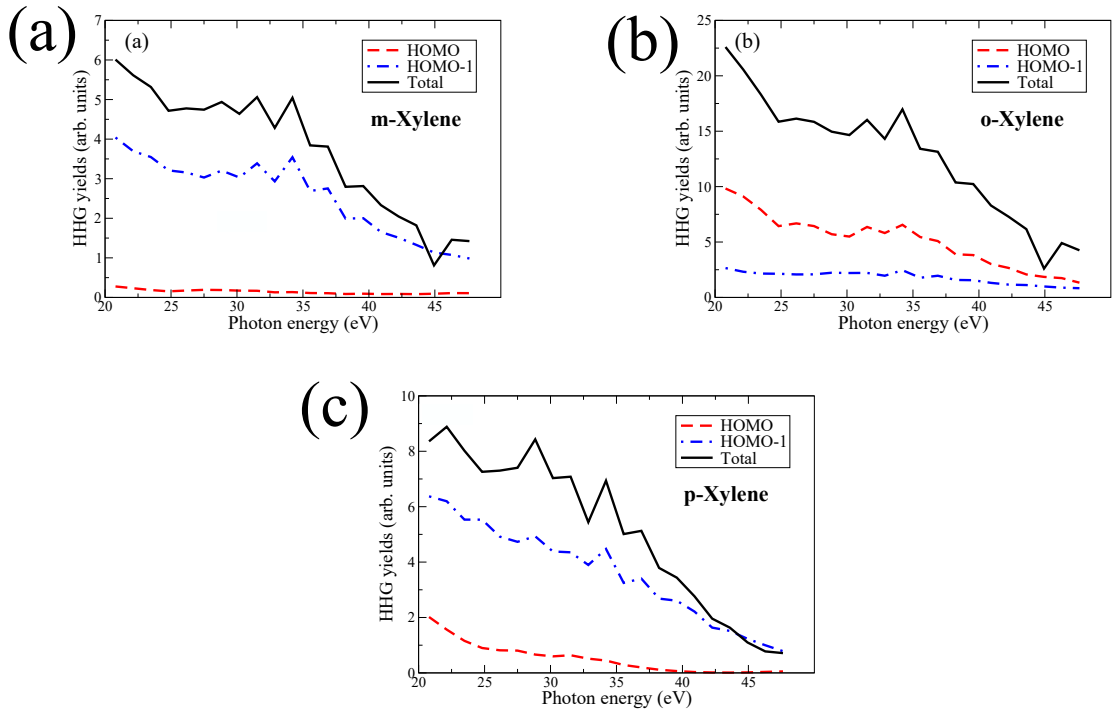

Figure 5.9: Calculated HHG spectra for HOMO (red), HOMO-1 (green) and total signal (blue) for all three molecules. A 10-cycle pulse with wavelength of 1850 nm and intensity of 0.8×10^{14} W/cm^2 is used in simulations.

toionization cross section, as functions of angles [70, 79]. From the above analysis, it is quite clear that for the HOMO, o-xylene not only has the strongest tunneling ionization, but it also has strong overlap between ionization and recombination, while the other two isomers have weaker overlap since their tunneling ionization peaks move further away from the photo-recombination peak position. The QRS results for HHG yields presented in Fig. 5.9 indeed confirm this expectation: HHG yield from HOMO in o-xylene is much stronger than that from the other two isomers. The results also reveal that for m-xylene and p-xylene, HHG from the HOMO-1 actually dominates HHG from the HOMO. Also, HHG yield is stronger in p-xylene as compared to m-xylene, mostly due to a stronger overlap between tunneling ionization and photo-recombination in p-xylene, although ionization

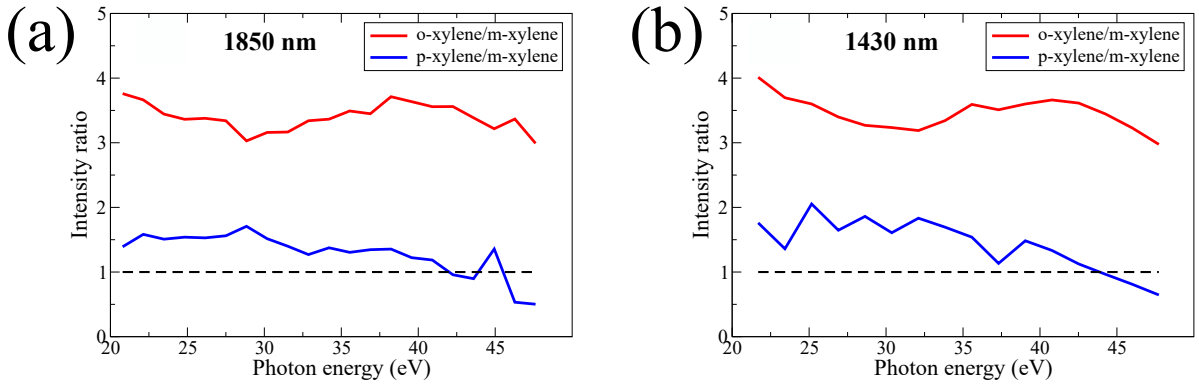

Figure 5.10: Calculated harmonic ratios of p-xylene to m-xylene (green) and o-xylene to m-xylene (blue). The laser wavelength is 1850 nm in (a) and 1430 nm in (b).

is slightly stronger in m-xylene. We remark that in order to mimic the effect of macroscopic propagation, our HHG results were obtained with laser intensity averaging [75, 76]. No depletion effect was taken into account in our calculations.

Total HHG induced dipole for each isomer is obtained by a coherent sum of contributions from the HOMO and HOMO-1. We found that the two contributions are mostly in phase for all isomers, see Fig. 5.9. The calculated ratio of o-xylene (p-xylene) to m-xylene is shown in Fig. 5.10(a) as red (blue) curve. These results reproduce qualitatively the experimentally obtained ratios at 1850 nm. We also found that these ratios remain nearly unchanged at the lower intensity of 0.4×10^{14} W/cm^2. We also present in Fig. 5.10(b) the theoretical ratios at laser wavelength of 1430 nm with intensity of 0.6×10^{14} W/cm^2. The ratios remain nearly the same as for 1850 nm case, whereas the experimental results show a stronger dependence on the laser wavelength, see Fig. 5.4. A possible reason is that the ionization calculation based on the SFA does not fully account for the laser wavelength dependence, especially since it neglects all excited states of the targets.

5.4 Conclusion

In this work, it was demonstrated that xylene isomers can behave differently even in transform-limited femtosecond pulses. This was demonstrated first by producing doubly charged ions of xylenes with intense femtosecond pulses at 800nm. At longer driving wavelengths, we also show subtle differences in the harmonic yields and their ellipticity dependence. The experimental results are supported by numerical calculations that reveal differences in both ionization and harmonic emission in Xylenes. Present work lays the foundation for future experiments on time-resolved dynamics of ring opening and ring permutation processes exhibited by these molecules as discussed more in chapter 8.

Chapter 6

Effects of Nodal Planes on Strong-field Ionization in Ring-type Molecules

With the growing interest in the strong field community to probe polyatomic molecules, it is extremely important to examine the validity of extending several beliefs regarding strong field ionization (SFI) that have shown success with simple systems to more complex molecules. A widely-accepted picture of SFI probability is that it scales with the electronic density of a molecular orbital along the laser polarization direction. As a result, ionization suppression is expected along nodal planes where the electronic density vanishes.

Owing to their unique symmetry, cyclic organic molecules are perfect targets to examine the influence of nodal planes on strong laser field processes. In this chapter, we investigate the effects of orbital nodal planes on the strong-field response of the ring-type molecules

furan (C_4H_4O), 2,3-dihydrofuran (C_4H_6O), and thiophene (C_4H_4S). The measured HHG signals from the different molecular species show different dependences on the ellipticity of the driving field. These differences imply that the continuum wave packets for each molecule have different lateral momentum distributions, hence different angular ionization dependence. Strikingly, and contrary to the conventional wisdom in the strong-field community, our TSDE-based computational results show that the observed differences can be attributed to the fact that for furan and thiophene the most probable orientation for SFI occurs when the electric field of the laser is aligned near a nodal plane of the corresponding ionizing orbital. On the other hand 2,3-dihydrofuran follows the standard expectation that the most probable orientation for SFI occurs when the electric field is aligned away from any nodal plane.

6.1 Background

Strong-field ionization (SFI) is a fundamental process that occurs during the interaction of intense laser fields with atoms and molecules [7, 80–82] and lies at the core of high-harmonic generation (HHG). The occupied orbitals in the multielectronic wave functions of molecules often possess rich nodal structures. These nodal structures can modulate the SFI rate [33, 83] as well as add non-atomic-like phase [84] and amplitude [85–88] modulations to the continuum electron wave packets when the electric field of the ionizing laser is aligned along certain directions relative to the molecular axis. Of particular relevance to this chapter, the conventional wisdom in the strong-field community maintains that ionization should be suppressed when the electric field of the laser points along, or near, nodal planes

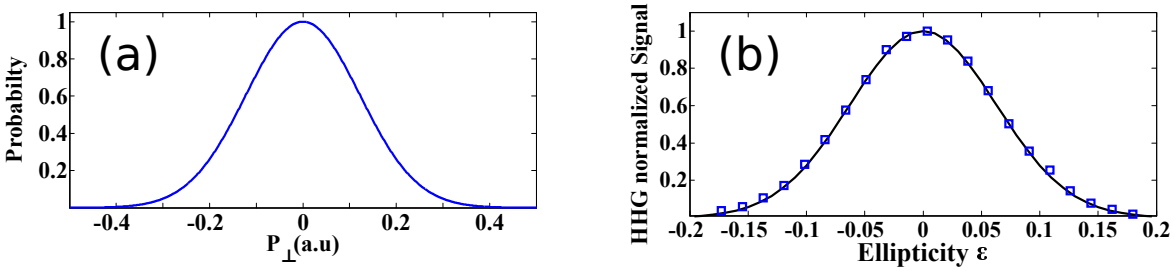

Figure 6.1: a) Initial lateral momentum distribution for an electron born at a laser phase corresponding to the emission of the 41st harmonic in Ar b) The measured ellipticity dependence of the 41st harmonic for Ar (blue squares). Analytical caculations based on the approach presented in section 2.1.4.2.1 are shown in solid curve. The laser intensity of 8×10^{13} W/cm^2 and a wavelength of 1800 nm.

of the orbitals. This expectation was first derived using the strong-field approximation for diatomics by Muth-Böhm, Becker, and Faisal [83], and has been experimentally confirmed for various small molecules [5, 27, 89] such as O_2 (see section 2.2.3). However, as larger molecules are being explored, this expectation may no longer apply [90].

6.2 HHG dependence on ellipticity and continuum wavefunction in atoms

When elliptically-polarized pulses are used to drive HHG, the continuum electron launched through SFI is deflected away from the parent ion. Hence increasing the ellipticity leads to a decrease in the recombination rate and the HHG signal [91, 92]. Since this decay depends on the lateral momentum spread of the ionizing wavefunction, its fingerprints can be obtained from the dependence of the intensity of harmonics on laser ellipticity. As discussed in section 2.1.4.2.1, a useful picture to approach this problem is by considering that the electron is born with initial transverse momentum defined by equation 2.6. In

Fig. 6.1(a), we show the probability corresponding to the short trajectory leading to the emission of the 41^{st} harmonic in Ar at 1800 nm and a laser intensity of 8×10^{13} W/cm^2. Taking this distribution into account, Fig. 6.1 shows how the calculated harmonic yield varies with laser ellipticity (solid line) based on equation 2.18. This is in a good agreement with the measured yield for the specific harmonic(blue squares).

To gain more insight into how the ellipticity dependence changes with harmonic order, the experimental data of the yield dependence on ellipticity were fitted with a Gaussian profile to extract the ellipticity width $\Delta\epsilon$. This quantity, defined as the ellipticity value at which the harmonic yield drops to 50% compared to the value at linear polarization, is plotted in Fig. 6.2(b) as a function of harmonic order. For Ar, $\Delta\epsilon$ decreases with increasing harmonic order, consistent with the fact that, for short trajectories, the travel time of the electron in the continuum is greater for higher harmonic orders leading to a larger relative displacement at recombination. The dashed lines shows the calculated $\Delta\epsilon$ using the semi-classical approach (balck) [17] and quantum orbit analysis (red). The calculated values are in good agreement with the experimental data.

6.3 HHG dependence on ellipticity in five-membered ring molecules

In general, mapping the harmonic yield variation with laser ellipticity on the momentum distribution of the ionizing wavefunction in complex molecules is not attainable with existing theoretical analysis. However, many qualitative results can be obtained from this

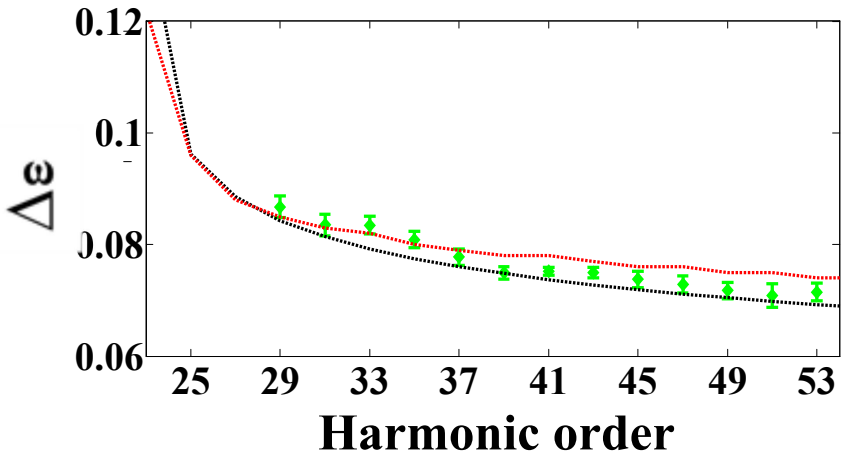

Figure 6.2: The ellipticity width $\Delta\epsilon$ as a function of harmonic order for Argon (green diamonds) at a laser intensity of 8×10^{13} W/cm^2. The calculated widths based on quantum orbit calculations (red dashed line) and equation 2.18 (black dashed line) are also shown.

dependence [5, 93]. For the current study on nodal planes effect, we selected three organic molecules sharing the same ring size: 2,3-dihydrofuran, furan, and thiophene. In contrast to the first molecule, furan and thiophene are aromatic molecules whose two highest occupied molecular orbitals are fully delocalized π orbitals with two nodal planes, along and perpendicular to the ring.

Fig. 6.3(a) show the yields of the 41$^{\text{st}}$ harmonic as a function of laser ellipticity ϵ, defined earlier, for 2,3-dihydrofuran compared to furan. Similarly, we compare the dependence of the 41$^{\text{st}}$ and 45$^{\text{th}}$ harmonics in 2,3-dihrofuran and thiophene in Fig. 6.3(b) and (c), respectively. Two interesting features can be observed. First, the response of the high harmonic yield to the ellipticity variation is weaker for both furan and thiophene as compared to 2,3-dihydrofuran. This suggests that the lateral momentum spread of the recollision wave packet is larger in furan and thiophene as compared to 2,3-dihydrofuran. Second, the dependence is slightly flatter around linear polarization in higher order harmonics in thiophene.

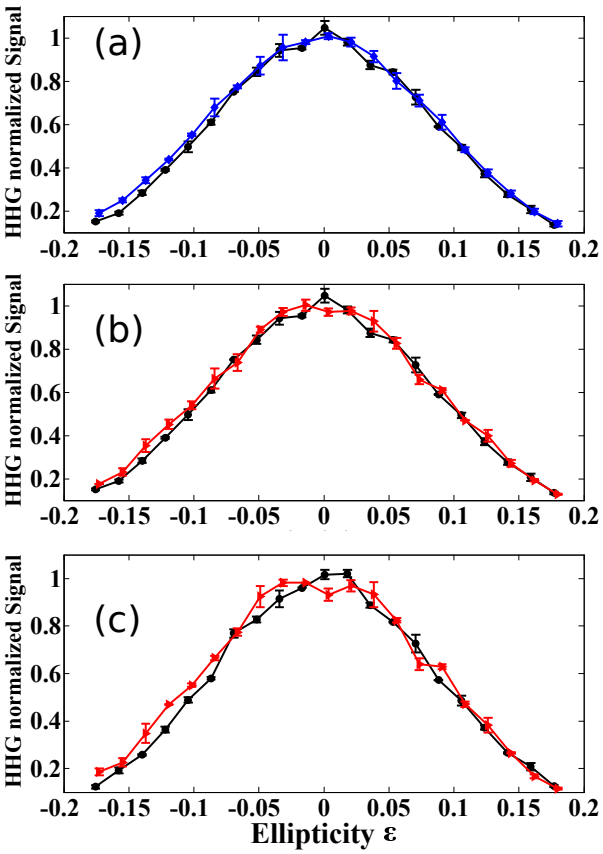

Figure 6.3: The ellipticity dependence of the 41st harmonic for 2,3-dihydrofuran (black circles) vs. (a) furan (blue squares) (b) thiophene (red triangles). (c) similar to (b) but for the 45th harmonic. The experiments were conducted at a laser intensity of 3 $\times 10^{13}$ W/cm^2 and a wavelength of 1800 nm.

The lateral momentum scales inversely with the ionization potential of atoms. In molecules, since the ionization potential is much lower than that of Ar, for a given intensity $\Delta\epsilon$ can be expected to be larger compared to Ar. Furthermore, the higher angular momentum components generally present in molecular orbitals leads to an additional increase in $\Delta\epsilon$ for molecular systems [85]. Fig. 6.4 shows $\Delta\epsilon$ as a function of harmonic order for the three molecules at a laser intensity of (a) 3×10^{13} W/cm^2 and (b) 4×10^{13} W/cm^2. The second set has a better statistical behaviour because of the higher harmonic flux. In general, $\Delta\epsilon$ is a decreasing function of harmonic order in 2,3-dihydrofuran, similar to that

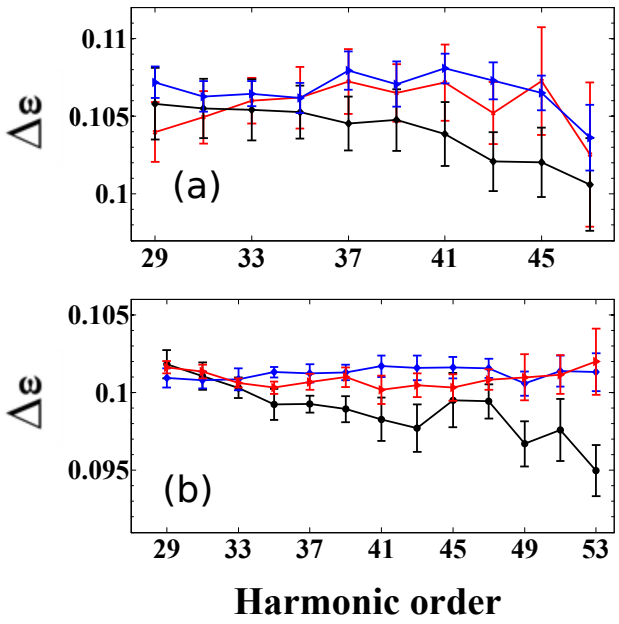

Figure 6.4: The ellipticity width $\Delta\epsilon$ as a function of harmonic order for 2,3-dihydrofuran (black circles), thiophene (red triangles) and furan (blue squares) at two different laser intensities 3×10^{13} W/cm^2 (a) and 4×10^{13} W/cm^2 (b) . The experiments were done with a laser wavelength of 1800 nm. The errors bars represent the 95% of the confidence interval of the Gaussian fits.

of Ar. In contrast, the ellipticity widths in furan and thiophene does not decrease with the harmonic order and, generally, have larger values suggesting that the lateral momentum spread in these two molecular systems share similar qualitative characteristics that are different from those of 2,3-dihydrofuran.

6.4 Angular ionization

In order to understand the experimental differences in the ellipticity dependence, we carry out time-dependent Schrödinger equation calculations of the ionization process using the time-dependent resolution-in-ionic-state (TD-RIS) method [59, 94]. The computational details of both the electronic structure and the ionization computations appear in Ref. [95]. In addition to the details specified in that paper, here we make use of an effective

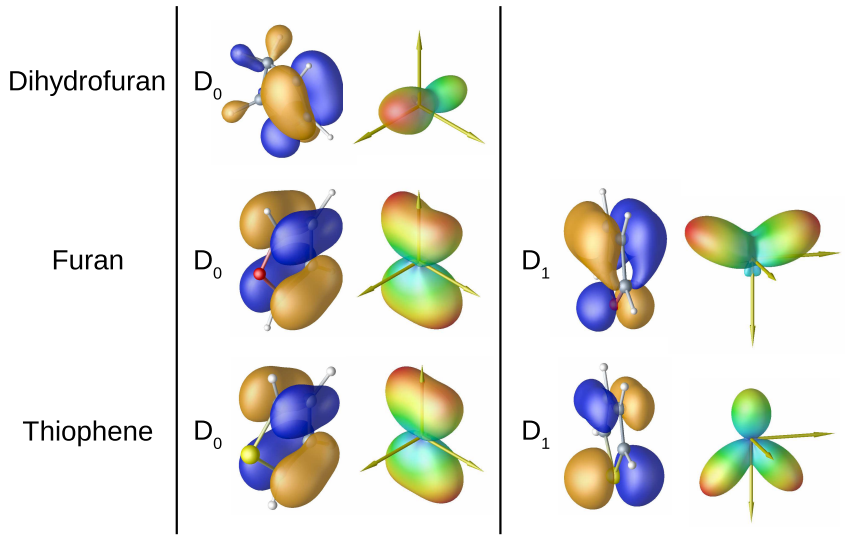

Figure 6.5: Dyson orbitals (orange/blue plots) and the corresponding orientation dependence of the strong-field ionization yields for the non-negligible ionization channels of the molecules considered in this study.

core potential [96] for the S atom in thiophene. We calculate the SFI probabilities using a single half-cycle of the 1800 nm laser field, which allows us to focus on the sub-cycle ionization probabilities that are relevant to HHG. Further, the use of a half-cycle pulse is also important to retain the directionality of the sub-cycle orientation-dependent SFI probability—running the computation for a full cycle and/or a multicycle pulse would necessarily lose the directional SFI information since it would include ionization for a given electric field direction as well as the opposite direction when the field changes sign on the following half-cycle.

In chapter 4, it was shown that only ionization to the ground state of the cation (D_0 channel) is important for 2,3-dihydrofuran, while for furan and thiophene both the D_0 and the D_1 channels contribute. The orientation-dependent SFI probabilities for these active channels are shown in Fig. 6.5. For 2,3-dihydrofuran, there are two lobes of strong ionization. The fact that these two lobes show slightly different peak ionization yields

reflects the fact that 2,3-dihydrofuran has a broken symmetry (it has C1 symmetry). These two lobes appear at angles that do not lie along nodal planes.

For furan and thiophene, the D_0 channel shows two broad lobes of high SFI probability centered along the plane of the molecule with the peak angle of SFI located at approximately 30° away from the the molecular plane. However, there is a very high probability (only about 10% lower than at 30°) for ionization directly along a plane that coincides with a nodal plane of the corresponding Dyson orbital for these two D_0 channels—there is no strong suppression of the SFI rate along these nodal planes. The D_1 channel in furan has peaks of the ionization yield pointing away from the nodal planes, while the D_1 channel in thiophene has three peaks in the ionization yield with two pointing away from the nodal plane and the third pointing directly along a nodal plane.

6.5 Electron wavefunction after SFI

We would now like to see the effect of the nodal planes in the ionized continuum electron wave packets. Consider first the continuum wave packets associated with the peaks in the orientation-dependent SFI yields. With the electric field of the laser polarized along the z-axis, we rotate each molecule such that it is oriented along the peak of the orientation dependence of the SFI probabilities shown in Fig. 6.5, and calculate the continuum wave packet using again the TD-RIS method. Note that the peak SFI probabilities for the D_0 and D_1 channels of both furan and thiophene are positioned at different angles, so we need to run the simulations at two different angles, one for the peak of the D_0 channel and a second angle corresponding to the peak of the D_1 channel.

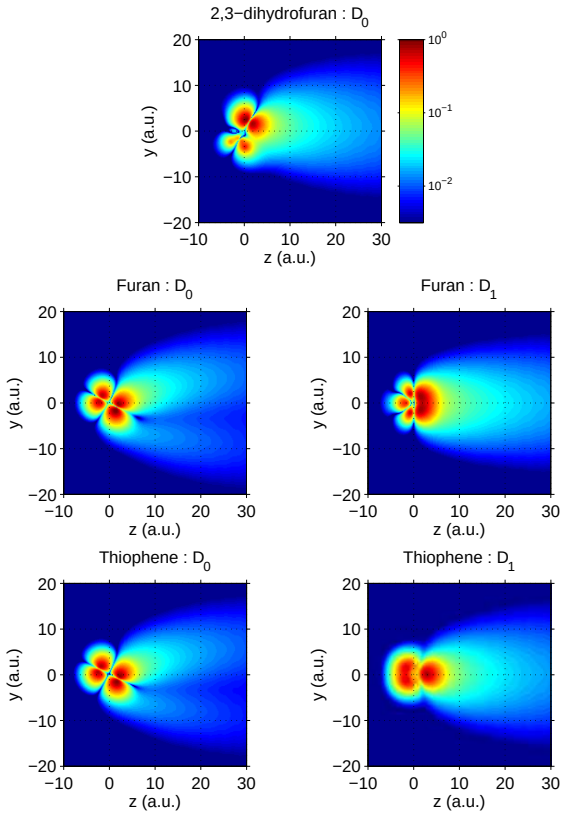

Figure 6.6: Cut along the continuum wavefunction at the time $t = 0.375\,\tau_0$, where $\tau_0 = 2\pi/\omega_0$ is the period of the carrier oscillations of the laser. In these simulations, the electric field of the laser points toward the -z direction, which pulls the negatively charged continuum electron toward the $+z$ direction.

Two-dimensional cuts through the computed three-dimensional continuum wave packets are plotted in Fig. 6.6. For these cuts, the electric field of the laser is aligned along the z axis, and the cuts are taken for a plane along $x = 0$ at the time $t = 0.375\tau_0$, where $\tau_0 = 2\pi/\omega_0$ is the period of the carrier oscillations of the laser. In these cuts, the center-of-mass of the molecules are positioned at the origin of coordinate system. For the cases where the peak of the orientation-dependent SFI yields lie away for the nodal planes (i.e. 2,3-dihydrofuran and the D_1 channels of furan and thiophene), the continuum wave packets exhibit a Gaussian-like distribution perpendicular to the electric field direction. For the D_0 channels of furan and thiophene, part of the nodal structure of the Dyson orbital is

seen to persist into the continuum.

Fig. 6.7 plots the corresponding transverse momentum distributions computed by taking the Fourier transform of the wave packet slice $\mathcal{D}(p_x, p_y) = |\mathcal{F}.\mathcal{T}.(\Psi_{cut})|^2$. To generate these tranverse momentum distributions, we first take a cut of the continuum wave packet in a plane perpendicular to the electric field direction (z-axis), $\Psi_{cut}(x, y) = \Psi(x, y, z_0)$, where z_0 sets the position of the chosen plane along the z-axis. In the following analysis, we use $z_0 = 15$ atomic units (a.u.) which lies comfortably away from the exponential tails of the Dyson orbitals but still close to the spatial point of birth of the continuum wave packet. Although there are quantitative differences when z_0 is varied, we checked that the conclusions of our analysis are independent of the particular choice of z_0 as long as it does not overlap with the tails of the initial bound orbital.

From these plots presented in Fig. 6.7, it is seen that $\mathcal{D}(p_x, p_y)$ is widest for the D_0 channels of furan and thiophene, the same two channels that had nodes in the continuum wave packets. Since the spatial and momentum representations of the wave function are related by the Fourier transform, the increased width seen in the momentum distributions are a direct consequence of the nodal structure in the continuum. Such an increase in the momentum width when ionizing along nodal directions has been noted in the literature [85–87]. The novel feature of our study is that these effects of the nodal planes occur for the particular orientations where SFI is most probable.

The momentum distributions of the continuum wave packet plotted in Fig. 6.7 explain the differences seen in the ellipticity measurements. Furan and thiophene both exhibit ionization channels with wide momentum spreads (the D_0 channels). For these species, the

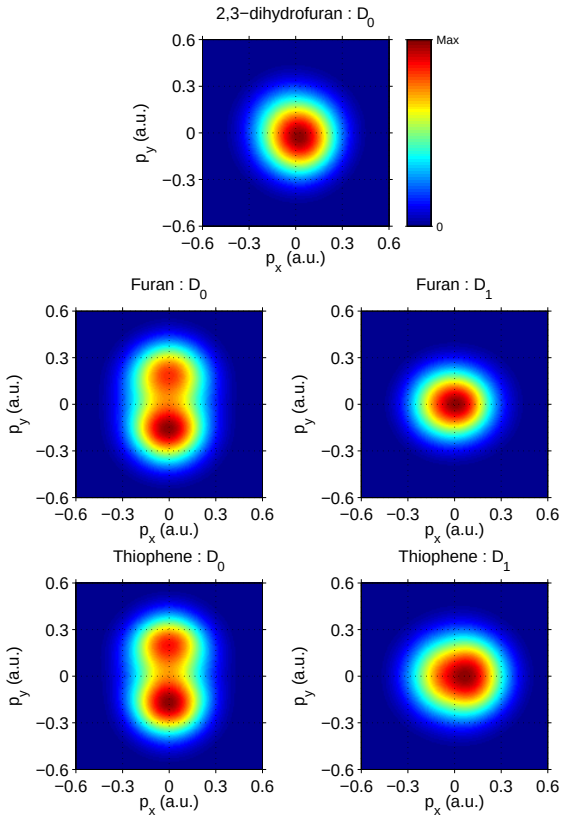

Figure 6.7: Perpendicular momentum-space cuts of the continuum electron wavefunctions taken at the peak of the field ($t = \tau_0/4$), and $z = 15$ a.u. ($|\psi(p_x, p_y, z = 15 \text{ a.u.})|^2$), where z is the direction of the electric field vector of the ionizing laser. The cuts are qualitatively similar when taken at other times and at other z positions. (a.u refers to atomic units)

large momentum spreads means that the recollision wave packet will be wider as compared to the 2,3-dihydrofuran case, and hence larger ellipticity is needed to deflect the recollision wave packet and suppress the HHG emission. Although the above analysis only considered orientations that correspond to the peak ionization rates, it is clear from Fig. 6.5 that when averaging over all the orientations, the D_0 channels of furan and thiophene will show strong effects of the nodes in the continuum wave packet for the majority of orientations since the averaging will now encompass orientations that lie even close to, and directly along, nodal planes. Our interpretation is then robust to orientational averaging.

6.6 Conclusion

In summary, the ellipticity dependence of HHG provides information on the liberated continuum electron wave packet as well as the orientation dependence of SFI, even in the case of randomly oriented molecules. When the most probable orientation for SFI is near a nodal plane (furan and thiophene), the node of the ionizing orbital persists into the continuum wave packet thereby increasing the lateral momentum distribution, which leads to the observed differences in the ellipticity dependence of HHG for the studied molecular species. These theoretical and experimental findings draw into question the standard expectation that suppression of SFI should occur for orientations that lie along or near nodal planes of the ionizing orbitals.

Chapter 7

HHG in Cyclohexadiene: Symmetry Effects

In this chapter, molecular high-order harmonic generation is employed to reveal structural and dynamical information from cyclohexadiene molecules. It is first shown that the harmonics from the two molecular isomers of partially π-bonded molecules, 1,3 and 1,4 cyclohexadiene C_6H_8 (1,3 and 1,4 CHD), have different characteristics. In particular, the harmonic spectra of 1,4 CHD are much weaker and have a pronounced minimum at a photon energy of approximately 30 eV whereas no spectral minimum is observed in 1,3 CHD. The spectral amplitude modulation can be attributed to a geometric origin leading to quantum interferences between the recolliding electron and the molecular wavefunctions. Due to the unique symmetry of this molecule, we show that this two-centre type interference can occur through three different configurations in HOMO and HOMO-1. In addition to the main driving field, a second weak probe of another colour is used to control electron

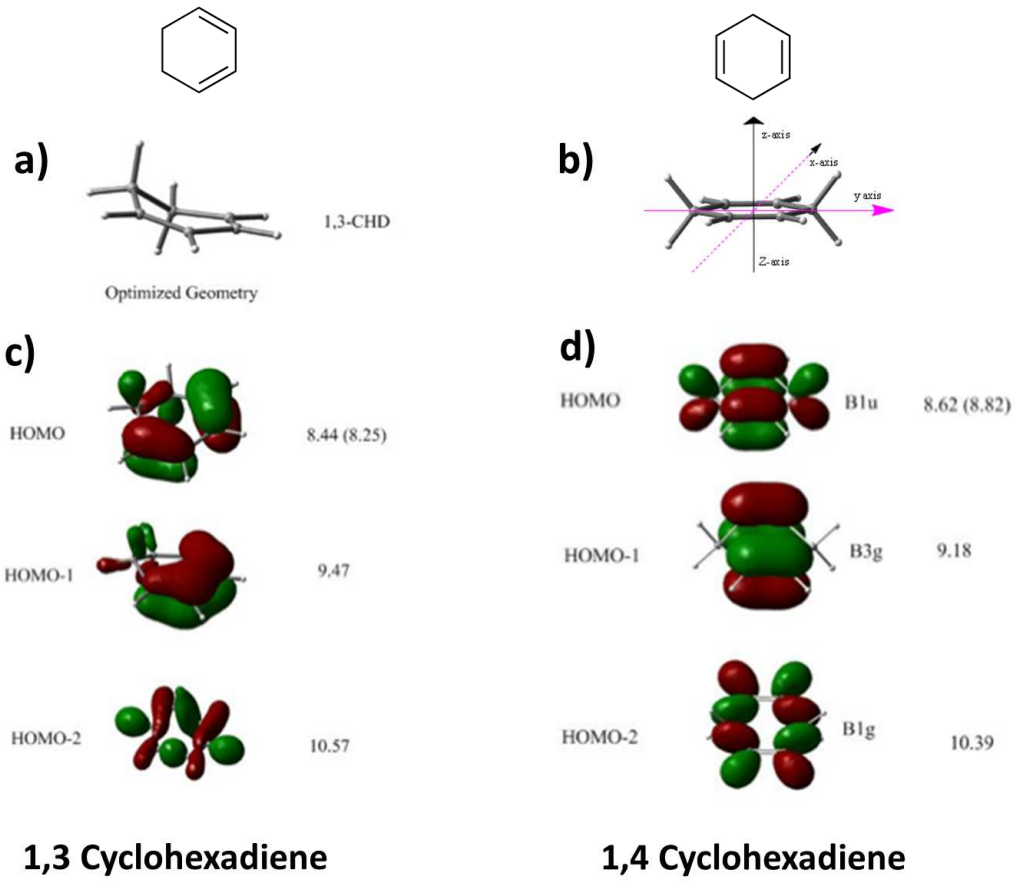

Figure 7.1: Geometrical structures of (a) 1,3 CHD and (b) 1,4 CHD. DFT/LB94 images and energies of the Kohn-Sham molecular orbitals of 1,3-CHD (c) and 1,4-CHD (d). Only the three highest occupied molecular orbitals, HOMO, HOMO-1 and HOMO-2 are shown with their absolute energies in eV.

trajectory. The two-colour HHG measurement suggests that the generation process may also involve hole dynamics. Real-Time-Dependent Density Functional (TDDFT) calculations show the importance of inner-shell ionization as a function of molecular orientation.

7.1 Background

1,3 and 1,4 CHD share the same atomic structure with a ring configuration containing two double bonds (upper panel in Fig. 7.1). However, while the double bonds in 1,3 CHD

are conjugated, they are uncoupled by the methylene groups in 1,4 CHD. The different bond arrangements translate into significant differences in geometry and electronic structure, which can be detected by various spectroscopic techniques. For example, Raman spectroscopy of both molecules indicated that the ring is permanently twisted in 1,3 CHD whereas it is planar in 1,4 CHD [97]. As a result, 1,4 CHD has a unique symmetry with the double bonds being parallel in the ring plane. This is similar to an ethylene (C_2H_4) dimer.

Similar to the discussion of molecular orbitals in benzene in section 4.1, we can treat the π systems in cyclohexadiene molecules separately from the σ framework. However, in this context, the two molecules differ from benzene in two main ways. First, there are two π orbitals below the bonding line instead of three because of the presence of only two double bonds. Second, besides the π character of the double bonds, HOMO and HOMO-1 could have contributions from the methylene groups in the ring. This simple analysis is confirmed by *ab intio* calculations based on the Kohn-Sham method [98] for the highest three molecular orbitals of both molecular isomers, presented in Fig. 7.1. Basic molecular orbital analysis predicts a different orbital ordering in 1,4 CHD, i.e., HOMO must lie below HOMO-1. However, the predicted lowest-energy π orbital on the double bonds is coupled with the C-H bonds that have the same symmetry as p atomic orbitals. This "through-bond coupling" [99] is strong enough to make the energy of this orbital higher than the energy of the other π orbital. As a result, the actual HOMO in 1,4 CHD shown in Fig. 7.1b has a unique symmetry featuring two parallel pairs of lobes.

This pair of molecules has been the subject of several comparative studies [100] including

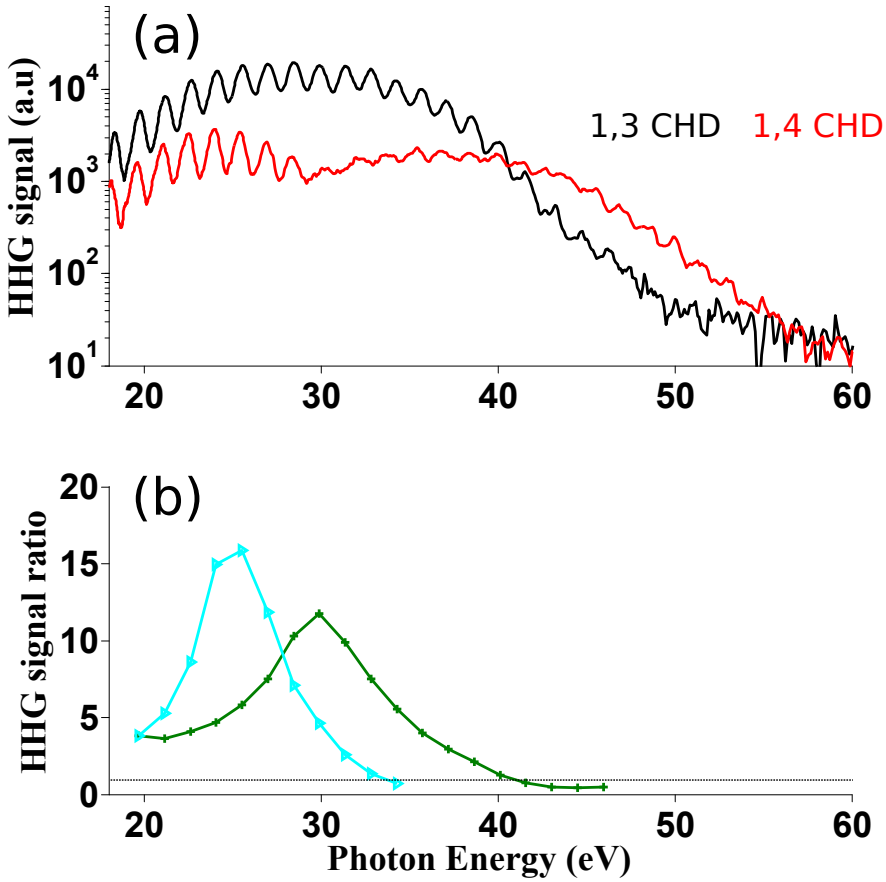

Figure 7.2: a) Harmonic spectra for 1,4 cyclohexadiene (red) and 1,3 cyclohexadiene (black) at an intensity of 6.5×10^{13} W/cm^2 with 20fs-1700nm pulses. (b) Ratio of the harmonic signal of 1,4 CHD to 1,3 CHD with 20fs-1700nm pulses and at intensities of 4.5×10^{13} W/cm^2 (cyan) and 6.8×10^{13} W/cm^2 (green)

their response to strong laser field. Harada *et. al.* [101] observed heavy fragmentation in 1,4 CHD irradiated by 800nm-120fs laser pulses at an intensity of 10^{14} W/cm^2. On the other hand, a significant yield of parent cations was detected in 1,3 CHD. These differences were explained by the presence of resonance excitation at 800 nm in the cation of 1,4 CHD while this resonance is not exhibited by its structural isomer, 1,3 CHD. As a result, to avoid this resonance effect, longer wavelengths must be utilized in order to explore these molecules using high-order harmonic spectroscopy.

7.2 Harmonic spectra

High-order harmonic spectra of 1,4 CHD and 1,3 CHD produced by 1700 nm, 20 fs pulses at an intensity of 6.5×10^{13} W/cm^2 are shown in Fig. 7.2a. Three major differences can be observed between the two molecules. (i) The yield of plateau harmonics for 1,3 CHD is higher by an order of magnitude compared to 1,4 CHD. (ii) The yield of cut-off harmonics in 1,4 CHD is higher than 1,3 CHD. Also, the harmonic cutoff in 1,4 CHD is higher by ∼3-4 eV although both molecules have comparable ionization potentials. iii) 1,4 CHD exhibits a spectral minimum at ∼ 30 eV. Figure 7b shows the ratio of 1,3 CHD harmonic signal to that of 1,4 CHD at two different intensities. A value of unity corresponds to equal harmonic yield from both molecules (represented by the dashed line in Fig. 7.2b). The two ratios appear similar but with different magnitudes. For both intensities the ratio is ∼ 4 for low-order harmonics and reaches a maximum of 11 and 16 respectively in the plateau region before they decline rapidly when approaching cut-off harmonics. In the cut-off region, the ratio is less than unity beyond 40 eV at high intensity where the harmonic yield from 1,4 CHD is higher than 1,3 CHD. Also, the harmonic order at which the ratio is maximum shifts by ∼4 eV between the two intensities. This shift occurs due to the movement of the harmonic cutoff and spectral minimum with laser intensity.

One of the main differences between 1,3 and 1,4 CHD is that the two double bonds in 1,3 CHD are conjugated, hence the two π-orbitals communicate with each other. The structure of the highest occupied orbitals in 1,3 CHD is, therefore, partially similar to that of a fully aromatic system. As established in chapter 4, aromatic systems are efficient HHG sources compared to non-aromatic systems. Similarly, it is reasonable to expect that

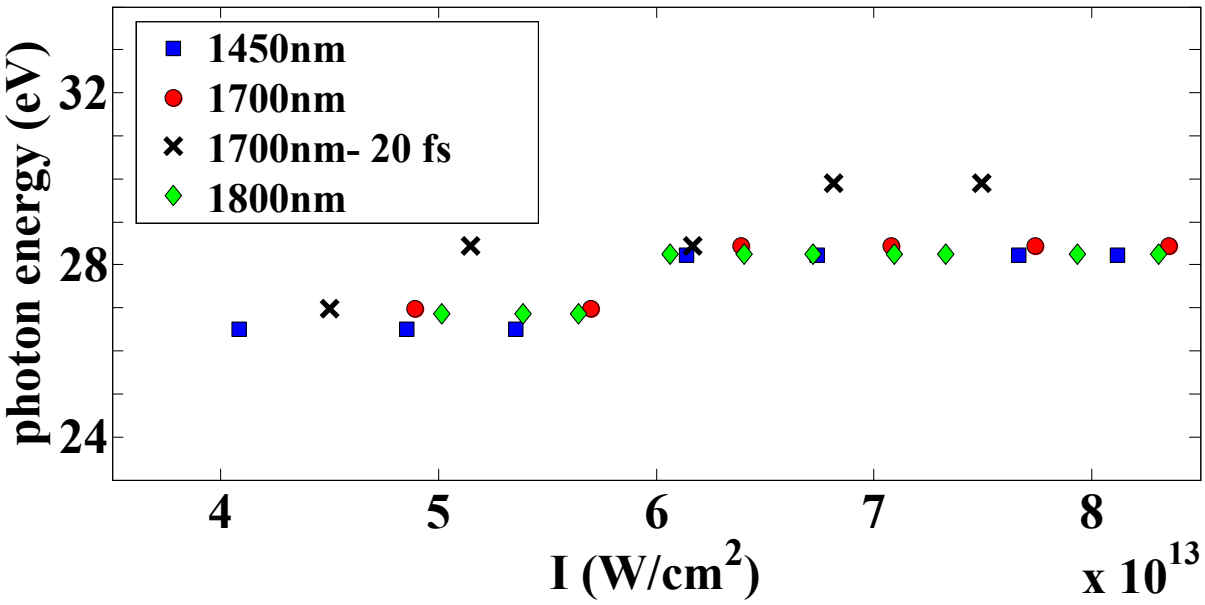

Figure 7.3: Position of the amplitude minimum in the harmonic spectrum of 1,4 CHD as a function of laser intensity for wavelengths of 1400 nm, 1700 nm and 1800 nm with pulse durations of 50-60 fs and 1700 nm with a pulse duration of 20 fs.

1,3 CHD generates brighter harmonics compared to 1,4 CHD where the two π-orbitals are decoupled.

The spectral minimum in the 1,4 cyclohexadiene harmonic spectrum is observed in different harmonic sources and under different laser parameters. Fig. 7.3 shows the position of observed minimum in HHG spectra of 1,4 cyclohexadiene for different wavelengths, intensities and pulse durations. It is clear that the amplitude minimum shows a slight upwards shift with increasing intensity and no dependence on wavelength.

7.3 Numerical calculations

To gain insight into the HHG process in 1,4 CHD, nonlinear real-time TDDFT calculations of ionization [102] are carried for all relevant molecular orbitals. Fig. 7.4 shows that HOMO

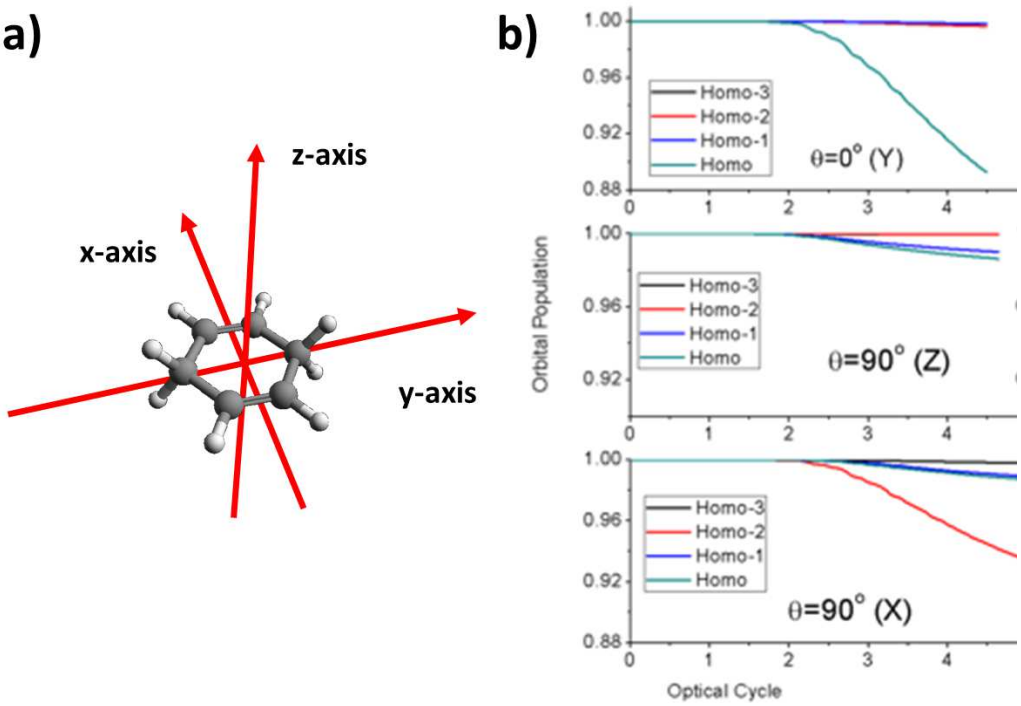

Figure 7.4: Orbital population, $N(t)$, of 1,4-CHD for angles, $\theta = 0^{o}$ (Y axis) , 90^{o} (X and Z) between the main molecular Y-axis and the laser polarization (Fig.1).The laser intensity is I= 1.2×10^{14} W/cm^2 and λ=1700 nm.

ionization is dominant for the y-direction, corresponding to the laser polarization parallel to the π-bonds. For x-axis ionization, the in-plane σ-orbitals (HOMO-2) are prevalent. Ionization perpendicular to the π-orbital molecular plane, i.e., the z-direction, is relatively weak in 1,4 CHD and comes evenly from both HOMO and HOMO-1.

7.4 Structural effect

In section 2.2.5, we learned that the returning electron wavepacket can experience a destructive interference when it recombines to a two-centre structure. A destructive interference can occur if: $R = n\lambda_B/(2\cos(\theta))$ where n is an odd (even) integer for a symmetric (anti-symmetric) orbital and θ is the angle between the laser polarization vector and molecular

a)

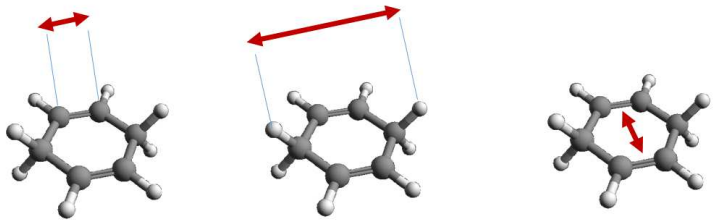

(1) (2) (3)

b)

#	Dimension	Orbital	Symmetry	R (A°)	Position of DI (eV)
1	Y	HOMO	π_u	1.32	30
2	Y	HOMO	π_u	4.31	27
3	X	HOMO-1	π_g	2.5	34

Figure 7.5: (a) Possible two-centre configurations in 1,4 CHD (b) Information on destructive interferences caused by these centres

axis. Here it is assumed that the molecular potential has no influence on the electron kinetic energy. There are three possible scenarios that result in destructive interferences during the recombination step which lead to the suppression for harmonics with photon energies at around the observed minimum:

1. The probability of ionization is maximum for HOMO when the laser polarization is parallel to the carbon double bonds. If we consider the lobes on the opposing H atoms in HOMO as a two-centre separated by ∼4.3 Å, then a destructive interference can occur for the electron trajectory that corresponds to emission of ∼27 eV photons (Fig. 7.5a1).

2. Also such two-centre interference can be represented by each two carbon atoms in each π bond in HOMO. The internuclear distance between each neighbouring carbon atoms is 1.32 Å that corresponds to a destructive interference leading to a spectral

minimum around 30 eV (Fig. 7.5a-2). In acetylene C_2H_2, Torres *et al.* observed a similar spectral minimum when the laser polarization was aligned along the molecular axis.

3. In addition to HOMO, the contribution from HOMO-1 could experience a destructive interference. The separating distance between the two π bonds is $\sim$2.5 Å with a corresponding expected minimum of approximately 34 eV (Fig. 7.5a-3).

In general, the positions of these predicted interferences in the harmonic spectra can be influenced by i) molecular vibration where R increases during the time between ionization and recombination (section 2.2.5) and ii) molecular orientation with respect to laser polarization. All above predicted minima (Fig. 7.5b), weighted by the significance of the corresponding channels to the HHG emission, contribute to the observed spectral minimum. As a result, the slight shift of the minimum with laser intensity observed in Fig. 7.3 reflects the variations in all different contributions as the intensity changes.

7.5 Dynamical effects

Probing hole dynamics is one of the fascinating applications of high-order harmonic spectroscopy. One way to track the population dynamics is by monitoring the presence of a spectral minimum due to a destructive interference between two different channels contributing to the generating process. In order to have an observable interference, two conditions must be satisfied: 1) The populations of the two channels are comparable, and 2) the relative phase $\Delta\varphi$ between the two channels is an odd multiple of π.

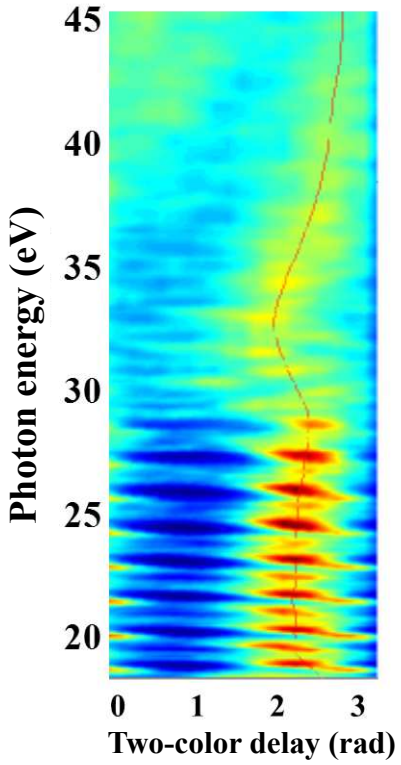

Figure 7.6: The variation of two-colour HHG signal in 1,4 CHD (colour scale) as a function of harmonic energy and phase delay between the two colours. For each photon energy, the signal was normalized with respect to the integrated signal for that specific photon energy over the two-colour delay. The intensity of the 48-fs,1750-nm fundamental field was $\sim 6\times 10^{13}$ W/cm^2.

It was shown in aligned CO_2 [38] that the presence of a structural interference in the HOMO can lead to the fulfilment of the first condition for observing hole dynamics in CO_2. This is due to the fact that the contribution of the dominating channel (HOMO) is weakened at around the structural minimum, hence a window into lower-lying orbitals is opened. In that particular case, the contributions to the HHG emission from two channels (HOMO and HOMO-2) become comparable along a certain orientation. It was, therefore, possible to observe hole dynamics within this window by tuning laser parameters.

To examine whether a similar phenomenon occurs in 1,4 CHD, a two-colour experiment was conducted. A 48-fs,1750-nm driving field with an intensity of $\sim 6\times 10^2$ W/cm^2 was

used along with its orthogonal second harmonic. The second harmonic was produced with a conversion efficiency of $\sim 5\%$ in energy as compared to the main driving field. Therefore, the second harmonic has no significant effect on the tunnelling rate [103]. Fig. 7.6 shows how odd and even harmonics vary with the delay between the two colours. For each photon energy, the signal was normalized by dividing by the integrated signal for that specific photon energy over the phase delay. The red line connects the maximal signals of different harmonics and is a guide to the eye. This line changes smoothly with phase delay except for photon energies at around the structural minimum where a phase shift can be observed. As discussed in detail in section 2.2.5, this behavior can be an indication of interference between two channels. This multi-orbital effect is expected to occur between the two channels corresponding to HOMO and HOMO-1 along the Z-direction where they have similar contributions. However, the observed phase modulation is less than $\pi/4$ and is, therefore, less pronounced than the phase jump ($\sim \pi/2$) reported for CO_2 [34]. This deviation can be attributed to the fact that 1,4 CHD is randomly oriented and there are other active channels that do not participate in the hole dynamics. In particular, HOMO-2 has noticeable ionization along x-direction which affects the strength of the modulation in the signal as a function of two colour delay.

Since the ionization along the Z direction is weak, the fingerprints of emission from this direction on the harmonic spectrum cannot generally be observed unless the molecular ring is aligned perpendicular to the laser field. However molecular alignment is hard for such a complex system. Fortunately, the presence of the structural effects along other directions around 30 eV allows for observable dynamical interactions along z-direction to be possible

within this window.

7.6 Conclusion

In summary, the HHG process in 1,3 CHD and 1,4 CHD demonstrates different signatures due to the differences in spatial and orbital structures of the molecular pair. The laser-induced recollision process of the freed electron displays the ability to extract information on the unique symmetry of 1,4 CHD through quantum interferences with the bound molecular state. The two-colour HHG shows an indication that these molecular-scale interferences provide a window for multi-orbital effects to be visible. However, to confirm the presence of observable multi-orbital effects in the HHG from 1,4 CHD, further theoretical analysis and experimental efforts have to be implemented. First, the conditions that lead to this effect at the current experimental conditions have to be determined. Then a series of different two-colour experiments at different laser intensities and wavelengths need to be conducted. If the experimental results follow the theoretical predictions for either the presence or absence of dynamical interferences for each experimental case, then this effect can be assured.

Chapter 8

Conclusions and future outlook

The molecules studied in this thesis are basic representatives of the class of five-membered and six-membered cyclic compounds. They are exceptionally important in science and technology because they feature unique chemical and physical properties; moreover they are considered to be building blocks for i) conducting polymers and ii) biologically relevant systems. The work described in this thesis comprises original research that has contributed to the spectroscopy of cyclic organic molecular systems. This has offered novel insights into the way these compounds respond to a strong laser field and how this response could be connected to electronic dynamics and structures. This chapter summarizes the main findings of this thesis along with a brief discussion concerning further investigations.

A part of this work related the aromaticity character of cyclic molecules to the high-order harmonic generation yields. Aromaticity, which is a manifestation of the specific electronic structure of the de-localized π-electrons in some cyclic organic molecules, is one of the most useful qualitative concepts in chemistry. Unfortunately, there is no universally

direct method to evaluate the aromaticity degree of a molecule. Moreover, all indirect measures introduced in the literature to measure aromaticity are inconclusive. From this fact stems the importance of discussing aromaticity in light of another dimension such as HHG.

Our work investigated the influence of cyclic electron delocalization associated with aromaticity on the high-order harmonic generation process in organic molecules. We showed that the aromatic molecules benzene (C_6H_6) and furan (C_4H_4O) produce high-order harmonics more efficiently than non-aromatic systems with the same ring structure. We also demonstrated that the relative strength of plateau harmonics is sensitive to the aromaticity in five-membered-ring molecules using furan, pyrrole (C_4H_4NH) and thiophene (C_4H_4S). Numerical time-dependent Schrödinger equation simulations of total orientation-averaged strong-field ionization (SFI) yields showed that the HHG from aromatic molecules comes predominantly from the two highest π molecular orbitals, which contribute to the aromatic character of the systems. In the presented work we focused on five membered ring molecules because they have already been extensively investigated both experimentally and numerically by other techniques to quantify aromaticity. The goal of this work was to show that HHG yield in aromatic molecules is directly related to π electrons and can be potentially a valuable measurement tool to quantify aromaticity.

This work is a first step in a bigger plan to address the connection of HHG to aromaticity. As previously stated there is no universal descriptor of aromaticity that can be applied to all cases and different measures are known to vary in their performance in quantifying aromaticity. We believe HHG will be no different. To fully characterize the performance

of HHG in this context, there is a need for a comprehensive systematic study that spans a series of aromatic molecules featuring different ring sizes and atomic structures, including six membered ring molecules such as pyridine, pyridazine, toluene, chlorobenzene, fluorobenznene and bromobenzne. This type of a broad study will be necessary to identify the areas of success and failure of the HHG and whether it correlates with specific measures of aromaticity.

Xylenes, cyclic molecular isomers, in a strong laser field were shown to behave differently even in transform-limited femtosecond pulses. We first discussed how the mechanisms of producing the doubly charged ions of these isomers clearly differ when interacting with 800 nm light. In addition, our experimental results supported by numerical calculations revealed differences in the three steps of the HHG from these molecules especially at 1850 nm.

During the last stage of my PhD, I started a two-colour set-up in order to control ionization and dissociation processes in molecules. Encouraged by the results presented in this thesis, xylene isomers have been identified as one of the potential targets for future experiments in this new direction. The presence of a second weak field adds new dimensions to the interaction processes, thereby leading to a better understanding of the role of electron recollection.

A major goal of applying HHG spectroscopy to xylene isomers is to open the path towards utilizing this tool featuring high spatial and temporal resolutions for studying isomeric effects in these molecules. For example, m-xylene can experience ring permutation upon photoexitation by UV light to form o-xylene through an intermediate [104]. In

principle, our study showed that this interesting isomeration process can be probed by HHG since the signals from the two isomers are distinguishable.

This thesis also showed a new effect that occurs in some of cyclic molecules when brought under a strong laser field. It is a widely accepted view that molecular ionization is greater when the laser polarization is along directions with higher electron density and is suppressed along nodal planes where the density vanishes. We showed that this cannot be regarded as a general rule in strong laser field ionization. In fact, maximum ionization was shown to occur along or near a nodal plane in some ring-type molecules. We used this result to explain the differences among these molecules in terms of the harmonic yield dependence on ellipticity. It is expected that this remarkable conclusion will have a significant influence on theoretical and experimental progress in this field. A future extension of this study could be achieved by shifting the focus to the angular distribution of generated photoelectrons. Also, more theoretical investigations need to be conducted in order to determine the full conditions that lead to the existence of this effect for a specific molecular orbital.

HHG was also demonstrated to be capable of probing the spatial symmetry of 1,4 cyclohexadiene molecule. Although it was randomly oriented, structural fingerprints of this system were observed in the harmonic spectra. Moreover, our two-colour phase map showed that hole dynamics could be tracked in this molecule. However, more $\omega/2\omega$ measurements at a different wavelength to confirm this result and to shed more light on the characteristics of the channels participating in this dynamics are required.

Future developments motivated by the presented work on cyclic molecules may also focus on other time-resolved dynamics of excited states. According to the conversion of the

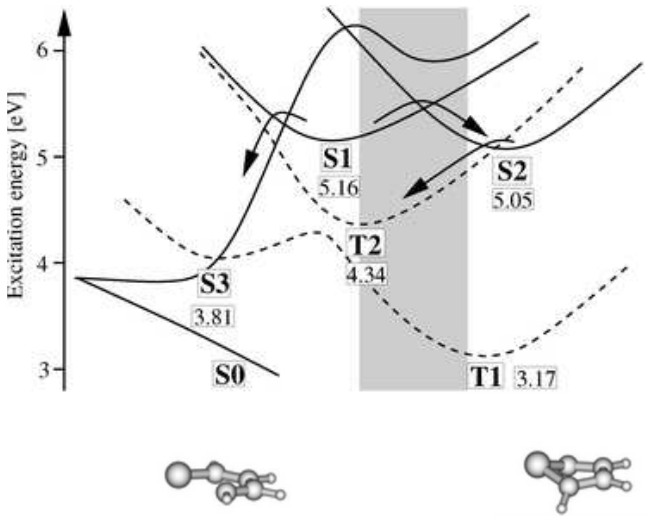

Figure 8.1: Schematic overview over nonradiative relaxation pathways in thiophene after photoexcitation to S1. The gray bar indicates the Franck-Condon range. From [105].

spin state, there are two important radiationless relaxation methods occurring in molecules after photo-excitation: internal conversion and intersystem crossing. For example, after being excited by 400 nm photons, o-xylene experiences internal conversion on sub-100fs time scale [106]. On the other hand there are very interesting and complex dynamics, involving two different intersystem crossing pathways and ring-opening, appear in thiophene after being irradiated by UV light (Fig. 8.1)[105]. Both systems are good targets for pump-probe experiments based on high harmonic spectroscopy where high time resolution can be reached.

Laser wavelengths in the range of 1.4μm to 1.8μm have enabled extension of high-order harmonic spectroscopy to complex molecules. Employing longer wavelengths on the order of 3 μm for HHG is very promising but yet also challenging. The difficulty is mainly due to the wavelength scaling of the HHG yield that goes with $\sim \lambda^{-5.5}$. However by designing better gas sources and with a careful choice of molecular targets, this problem could be overcame. There are several future directions that could exploit the features

associated with this particular wavelength. First, the magnetic field component of the laser field is more significant, therefore implying the breakdown of dipole approximation which could motivate a series of fundamental studies. From an applied viewpoint, this property would lead to better identification of chiral molecules. Second, the extended cutoff of harmonics produced at this wavelength offers a larger window for observing more signatures of molecular dynamics and structures. Moreover, the longer time that an electron takes in the continuum enables more hole dynamics to occur before the recombination event transpires. This will offer a larger window to observe dynamics on attoescond time scale like what was observed in propylene oxide. Finally the fact that the first few harmonics of 3μm are in the range of IR to UV offers a great advantage for studying below threshold harmonics from complex molecules even in free space. These harmonics cannot be explained by the basic three-step model since their energies are less than the I_p of the target. However, the generating mechanisms are still under ongoing investigations which involve aspects of multiphoton and multiple rescattering trajectories. The target potential has a key role in the production process. This effect is expected to be dramatic in the case of polyatomic molecules due to the complexity of their orbital symmetries and structures.

Appendix A

High-order Harmonic Spectroscopy of Cooper Minimum in Molecules

It is known that high-harmonic spectra from Ar [107][108] and Kr [109] atoms display spectral minima that are independent of both intensity and wavelength around 50 eV and 85 eV respectively. Both minima were attributed to the photo-recombination step which experiences a Cooper minimum (CM) at a particular energy. In this study, we show that HHG in randomly oriented molecules containing S and Cl atoms can exhibit a CM. We also investigate the effect of molecular environment on the position of the minimum.

CM was first observed in photoionization, the inverse process of the third step of HHG. In atoms, if an orbital has a radial node, the dipole matrix element describing the transition from initial ground state to final continuum state can change sign as a function of photon energy. The photo-ionization cross section PICS undergoes a Cooper minimum at the photon energy coinciding with the sign change [110]. Though CM is an atomic phe-

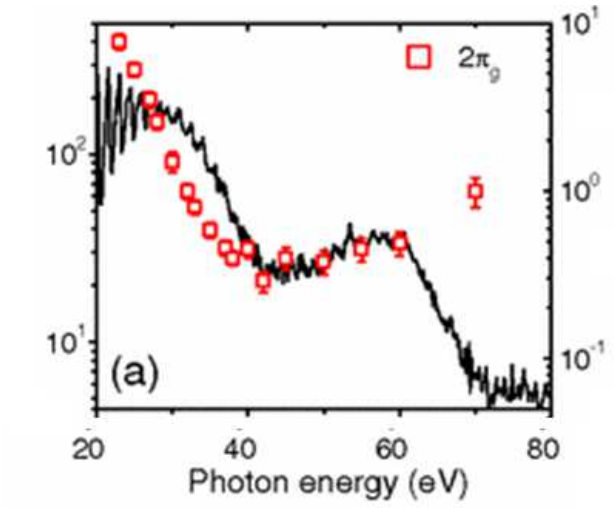

Figure A.1: HHG spectra using λ=1800nm wavelength light with intensity $\sim 910^{13}$W/cm^2 along with experimental (open symbols) partial PICS for CS_2.

nomenon, it persists in the photoionization of molecules containing atoms whose orbitals exhibit a radial node [111].

Fig. A.1 shows experimental high harmonic spectra of CS_2 (I_p=10.07eV) obtained with 1800nm light at an intensity of $\sim 9\times 10^{13}$ W/cm^2. For comparison, we also show the published PICS for lone-pair orbitals of CS2 ($2\pi_g$) obtained by angle-resolved photoelectron spectroscopy. Since lone-pair orbitals can be associated with a particular nucleus or atom, the observed minimum in the experimental PICS of these orbitals is analogous to photoionization of the 3p orbital of S atoms, which are known to exhibit a CM at $\sim$42.

The observed local minimum in the harmonic spectrum of CS_2 at $\sim$ 42eV coincides well with the minimum in the PICS. The relative harmonic amplitudes are in good agreement with the known PICS in the energy range of $\sim$30 - 60eV. They differ at high energies due to a sudden drop in the harmonic signal in the cutoff region and at low energies due to poor phase matching as well as reabsorption of generated harmonics.

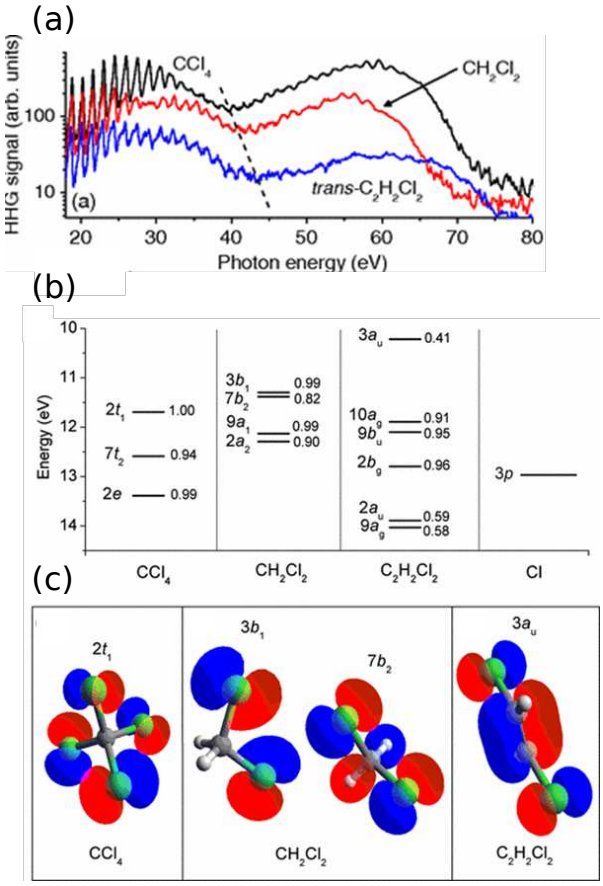

Figure A.2: (a) Harmonic spectra generated in CCl_4, CH_2Cl_2, and trans- $C_2H_2Cl_2$ using λ=1800nm and intensity $\sim 9\times10^{13}$W/cm^2. The dashed line emphasizes the shift of the minimum between different molecules. (b) Binding energies and corresponding Mulliken atomic populations on Cl for molecular orbitals of these three molecules as well as atomic Cl [2,33,34]. (c) Highest occupied molecular orbitals of CCl_4 (left), CH_2Cl_2 (middle), and trans- $C_2H_2Cl_2$ (right).

The degree of atomic character in molecular orbitals influences the position of the CM, which can vary for either (a) different orbitals of a given molecule or (b) different molecular environments. Thus, the CM can be used to probe the atomic nature of molecular orbitals. In fact, calculations of PICS for the 2π and 5σ bands in HCl [112] indicate a variation of the CM position by a few eV. However, this would be difficult to study using high harmonic spectroscopy due to the lack of selectivity of a specific orbital. Here, we study the case where the CM can be affected by the molecular environment and therefore can vary for different molecules even when their molecular orbitals originate from the same atomic

subshell (for example, the 3π orbital of Cl).

Fig. A.2(a) shows the harmonic spectra of three Cl-containing molecules using λ=1800nm light with intensity $\sim 9\times10^{13}$W/cm^2. Each harmonic spectrum exhibits a deep local minimum at 40.4±0.5eV (CCl_4, I_p=11.47eV), 42.1±0.4eV (CH_2Cl_2, I_p=11.32eV), and 43.2±0.4eV (trans- $C_2H_2Cl_2$, I_p=9.64eV). The dashed line indicates the noted shift of the minimum between different molecules. The positions of the amplitude minima in the harmonic spectra for all three molecules are independent of laser intensity and gas pressure, which suggests that they arise due to CM. This interpretation is also confirmed from the theoretical calculations. Minima arising through dynamical interference from multiorbital contributions to ionization [33] depend strongly on the laser parameters (intensity and wavelength) and can therefore be excluded. In addition, any minima arising from structural interference due to multicenter recombination [32] in unaligned molecules are expected to be very weak. A local minimum is reported to be present in PICS measurements for at least one orbital in CH_2Cl_2, but the position has not been published [113]. To our knowledge, PICS for trans- $C_2H_2Cl_2$ are not available for a direct comparison of the position of the CM, but the intensity-independent minimum in the harmonic spectrum is strong evidence that a CM must be present in the PICS.

The variation of CM in the three molecules is then a measure of the extent to which molecular orbitals retain part of their atomic character. To quantify the degree to which the 3p subshell of Cl exerts its influence on the molecular orbitals, we compare Mulliken atomic populations on Cl for each molecule. We performed ab initio calculations of the molecular orbitals at Hartree-Fock level using GAMESS [114]. In Fig. A.2(b), we show the

binding energies as well as the Mulliken atomic populations on Cl for all low-lying molecular orbitals of the three molecules in addition to the 3p subshell of Cl. All molecular orbitals within the 1114 eV range have lone-pair character and, consequently, have high Mulliken atomic populations on Cl. However, the highest occupied molecular orbital (HOMO) of trans- $C_2H_2Cl_2$ has bonding character from the C-Cl bond with some contribution from the 3p orbital of Cl [115]. Such bonding orbitals are also known to exhibit a minimum in their PICS known as a partial CM (for example, the 6a1 band in CCl_4 [111]).

The Mulliken atomic populations on Cl are 1.0, 0.9, and 0.4 for the HOMOs of CCl_4, CH2Cl2, and trans- $C_2H_2Cl_2$, respectively. Thus, the influence of the 3p subshell of Cl is more significant in CCl_4 and less so in trans- $C_2H_2Cl_2$ This is apparent from the molecular orbitals shown in Fig. A.2(c) and consistent with results from photoelectron spectroscopy where the visibility of the CM, represented by the depth in the angular distribution parameter, decreased as Cl atoms were replaced by H atoms in CCl_4 [113].

References

[1] J. Itatani, J. Levesque, D. Zeidler, H. Niikura, H. Pepin, J. Kieffer, P. Corkum, and D. Villeneuve, "Tomographic imaging of molecular orbitals," *Nature*, vol. 432, pp. 867–871, 2004.

[2] T. Kanai, S. Minemoto, and H. Sakai, "Ellipticity dependence of high-order harmonic generation from aligned molecules," *Phys. Rev. Lett.*, vol. 98, pp. 53002–053005, 2007.

[3] S. Baker, J. S. Robinson, C. A. Haworth, H. Teng, R. A. Smith, C. C. Chirilă, M. Lein, J. W. G. Tisch, and J. P. Marangos, "Probing proton dynamics in molecules on an attosecond time scale," *Science*, vol. 312, pp. 424–427, 2006.

[4] C. Vozzi, R. Torres, M. Negro, L. Brugnera, T. Siegel, C. Altucci, R. Velotta, F. Frassetto, L. Poletto, P. Villoresi, S. De Silvestri, S. Stagira, and J. P. Marangos, "High harmonic generation spectroscopy of hydrocarbons," *Appl. Phys. Lett.*, vol. 97, pp. 241103–241105, 2010.

[5] M. C. H. Wong, J.-P. Brichta, and V. R. Bhardwaj, "Signatures of symmetry and electronic structure in high-order harmonic generation in polyatomic molecules," *Phys. Rev. A*, vol. 81, pp. 61402–61405, 2010.

[6] M. Awasthi, "Molecules in strong laser fields in depth study of h_2 molecule," 2009.

[7] L. V. Keldysh, "Ionization in the field of a strong electromagnetic wave," *Soviet Physics JETP*, vol. 20, pp. 1307–1314, 1965.

[8] S. Augst, D. Strickland, D. D. Meyerhofer, S. L. Chin, and J. H. Eberly, "Tunneling ionization of noble gases in a high-intensity laser field," *Phys. Rev. Lett.*, vol. 63, pp. 2212–2215, 1989.

[9] M. V. Ammosov, N. B. Delone, and K. V. P., "Tunnel ionization of complex atoms and of atomic ions in an alternating electromagnetic field," *Soviet Physics JETP*, vol. 64, p. 1991, 1986.

[10] N. B. Delone and V. P. Krainov, "Energy and angular electron spectra for the tunnel ionization of atoms by strong low-frequency radiation," *J. Opt. Soc. Am. B*, vol. 8, pp. 1207–1211, 1991.

[11] P. B. Corkum, "Plasma perspective on strong-field multiphoton ionization," *Phys. Rev. Lett.*, vol. 71, pp. 1994–1997, 1993.

[12] A. McPherson, G. Gibson, H. Jara, U. Johann, T. S. Luk, I. A. McIntyre, K. Boyer, and C. K. Rhodes, "Studies of multiphoton production of vacuum-ultraviolet radiation in the rare gases," *J. Opt. Soc. Am. B*, vol. 4, pp. 595–601, 1987.

[13] T. Zuo, A. Bandrauk, and P. Corkum, "Laser-induced electron diffraction: a new tool for probing ultrafast molecular dynamics," *Chem. Phys. Lett.*, vol. 259, pp. 313 – 320, 1996.

[14] M. Meckel, D. Comtois, D. Zeidler, A. Staudte, D. Pavičić, H. C. Bandulet, H. Pépin, J. C. Kieffer, R. Dörner, D. M. Villeneuve, and P. B. Corkum, "Laser-induced electron tunneling and diffraction," *Science*, vol. 320, pp. 1478–1482, 2008.

[15]

[16] M. Möller, Y. Cheng, S. D. Khan, B. Zhao, K. Zhao, M. Chini, G. G. Paulus, and Z. Chang, "Dependence of high-order-harmonic-generation yield on driving-laser ellipticity," *Phys. Rev. A*, vol. 86, pp. 011401–011405, 2012.

[17] V. Strelkov, M. Khokhlova, A. Gonoskov, I. Gonoskov, and M. Ryabikin, "High-order harmonic generation by atoms in an elliptically polarized laser field: harmonic polarization properties and laser threshold ellipticity," *Phys. Rev. A*, vol. 86, pp. 13404–13413, 2012.

[18] Y. Li, X. Zhu, Q. Zhang, M. Qin, and P. Lu, "Quantum-orbit analysis for yield and ellipticity of high order harmonic generation with elliptically polarized laser field," *Opt. Express*, vol. 21, pp. 4896–4907, 2013.

[19] Y. Zheng, Z. Zeng, P. Zou, L. Zhang, X. Li, P. Liu, R. Li, and Z. Xu, "Dynamic chirp control and pulse compression for attosecond high-order harmonic emission," *Phys. Rev. Lett.*, vol. 103, pp. 43904–43907, 2009.

[20] L. Brugnera, D. Hoffmann, T. Siegel, F. Frank, A. Zaïr, J. Tisch, and J. Marangos, "Trajectory selection in high harmonic generation by controlling the phase between orthogonal two-color fields," *Phys. Rev. Lett.*, vol. 107, pp. 153902–153905, 2011.

[21] D. Shafir, Y. Mairesse, D. M. Villeneuve, P. B. Corkum, and N. Dudovich, "Atomic wavefunctions probed through strong-field light-matter interaction," *Nat. Phys.*, vol. 5, pp. 412 – 416, 2009.

[22] E. Takahashi, Y. Nabekawa, T. Otsuka, M. Obara, and K. Midorikawa, "Generation of highly coherent submicrojoule soft x rays by high-order harmonics," *Phys. Rev. A*, vol. 66, pp. 21802–21805, Aug 2002.

[23] M. Schnürer, Z. Cheng, M. Hentschel, G. Tempea, P. Kálmán, T. Brabec, and F. Krausz, "Absorption-limited generation of coherent ultrashort soft-x-ray pulses," *Phys. Rev. Lett.*, vol. 83, pp. 722–725, 1999.

[24] J.-P. Brichta, M. C. H. Wong, J. B. Bertrand, H.-C. Bandulet, D. M. Rayner, and V. R. Bhardwaj, "Comparison and real-time monitoring of high-order harmonic generation in different sources," *Phys. Rev. A*, vol. 79, p. 033404, 2009.

[25] E. Constant, D. Garzella, P. Breger, E. Mével, C. Dorrer, C. Le Blanc, F. Salin, and P. Agostini, "Optimizing high harmonic generation in absorbing gases: Model and experiment," *Phys. Rev. Lett.*, vol. 82, pp. 1668–1671, Feb 1999.

[26] M.W.Schmidt, K.K.Baldridge, J.A.Boatz, S.T.Elbert, M.S.Gordon, J.H.Jensen, S.Koseki, N.Matsunaga, K.A.Nguyen, S.Su, T.L.Windus, M.Dupuis, J.A.Montgomery J., "General atomic and molecular electronic structure system," *J. Comput. Chem.*, vol. 14, p. 1347, 1993.

[27] D. Pavičić, K. Lee, D. Rayner, P. Corkum, and D. Villeneuve, "Direct measurement

of the angular dependence of ionization for n_2, o_2, and co_2 in intense laser fields," *Phys. Rev. Lett.*, vol. 98, pp. 243001–243004, 2007.

[28] X. M. Tong, Z. X. Zhao, and C. D. Lin, "Theory of molecular tunneling ionization," *Phys. Rev. A*, vol. 66, pp. 33402–33412, 2002.

[29] K. Schafer, *Numerical Methods in Strong Field Physics*. New York: Springer New York, 2009.

[30] M. DeWitt and R. Levis, "Observing the transition from a multiphoton-dominated to a field-mediated ionization process for polyatomic molecules in intense laser fields," *Phys. Rev. Lett.*, vol. 81, pp. 5101–5104, 1998.

[31] N. Hay, M. Castillejo, R. de Nalda, E. Springate, K. Mendham, and J. Marangos, "High-order harmonic generation in cyclic organic molecules," *Phys. Rev. A*, vol. 61, p. 053810, 2000.

[32] M. Lein, N. Hay, R. Velotta, J. P. Marangos, and P. L. Knight, "Interference effects in high-order harmonic generation with molecules," *Phys. Rev. A*, vol. 66, pp. 23805–23810, 2002.

[33] O. Smirnova, Y. Mairesse, S. Patchkovskii, N. Dudovich, D. Villeneuve, P. Corkum, and M. Ivanov, "High harmonic interferometry of multi-electron dynamics in molecules.," *Nature*, vol. 460, pp. 972–977, 2009.

[34] D. Shafir, H. Soifer, B. Bruner, M. Dagan, Y. Mairesse, S. Patchkovskii, M. Ivanov, O. Smirnova, and N. Dudovich, "Resolving the time when an electron exits a tunnelling barrier," *Nature*, vol. 485, pp. 343–346, 2012.

[35] R. Cireasa, A. E. Boguslavskiy, B. Pons, M. C. H. Wong, D. Descamps, S. Petit, H. Ruf, N. Thiré, J. S. A. Ferré, . J. Higuet, B. E. Schmidt, A. F. Alharbi, F. Legaré, V. Blanchet, . B. Fabre, S. Patchkovskii, O. Smirnova, Y. Mairesse, and V. R. Bhardwaj, "Probing molecular chirality on a sub-femtosecond timescale," *Nat. Phys.*, vol. 11, pp. 654–658, 2015.

[36] M. Lein, "Attosecond probing of vibrational dynamics with high-harmonic generation," *Phys. Rev. Lett.*, vol. 94, pp. 53004–53007, 2005.

[37] H. Ahmadi, A. Maghari, H. Sabzyan, A. R. Niknam, and M. Vafaee, "Effect of nuclear motion on high-order-harmonic generation of $h_2{}^+$ in intense ultrashort laser pulses," *Phys. Rev. A*, vol. 90, pp. 43411–43417, 2014.

[38] R. Torres, T. Siegel, L. Brugnera, I. Procino, J. G. Underwood, C. Altucci, R. Velotta, E. Springate, C. Froud, I. C. E. Turcu, S. Patchkovskii, M. Y. Ivanov, O. Smirnova, and J. P. Marangos, "Revealing molecular structure and dynamics through high-order harmonic generation driven by mid-IR fields," *Phys. Rev. A*, vol. 81, pp. 51802–051805, 2010.

[39] M. C. H. Wong, A.-T. Le, A. F. Alharbi, a. E. Boguslavskiy, R. R. Lucchese, J.-P. Brichta, C. D. Lin, and V. R. Bhardwaj, "High harmonic spectroscopy of the Cooper minimum in molecules," *Phys. Rev. Lett.*, vol. 110, pp. 33006–033009, 2013.

[40] T. Popmintchev, M. Chen, O. Cohen, M. Grisham, J. Rocca, M. Murnane, and H. Kapteyn, "Extended phase matching of high harmonics driven by mid-infrared light," *Opt. Lett.*, vol. 33, pp. 2128–2130, 2008.

[41] N. Thiré, S. Beaulieu, V. Cardin, A. Larame, V. Wanie, B. Schmidt, and F. Lgar, "10 mj 5-cycle pulses at 1.8 μm through optical parametric amplification," *Appl. Phys. Lett.*, vol. 106, pp. 91110–91112, 2015.

[42] W. C. Wiley and I. H. McLaren, "Time-of-flight mass spectrometer with improved resolution," *Rev. Sci. Instr.*, vol. 26, pp. 1150–1157, 1955.

[43] E. Hückel, "Quantentheoretische Beiträge zum Benzolproblem," *Zeitschrift fur Physik*, vol. 70, pp. 204–286, 1931.

[44] P. W. Atkins and S. F. Ronald, *Molecular Quantum Mechanics*. New York: Oxford University Press, 2011.

[45] Z. Chen, C. S. Wannere, C. Corminboeuf, R. Puchta, and P. Schleyer, "Nucleus-independent chemical shifts (NICS) as an aromaticity criterion.," *Chem. Rev.*, vol. 105, pp. 3842–3888, 2005.

[46] F. Feixas, E. Matito, J. Poater, and M. Sola, "Quantifying aromaticity with electron delocalisation measures," *Chem. Soc. Rev.*, pp. 6434–6451, 2015.

[47] P. V. R. Schleyer, C. Maerker, A. Dransfeld, H. Jiao, N. J. R. V. E. Hommes, D. Erlangen, and R. V. February, "Nucleus-Independent Chemical Shifts : A Simple and Efficient Aromaticity Probe," *J. Am. Chem. Soc.*, vol. 7863, pp. 6317–6318, 1996.

[48] P. V. R. Schleyer, M. Manoharan, Z. Wang, B. Kiran, H. Jiao, R. Puchta, and N. Hommes, "Dissected nucleus-independent chemical shift analysis of π-aromaticity and antiaromaticity," *Org. Lett.*, vol. 3, pp. 2465–2468, 2001. PMID: 11483036.

[49] J. Aihara, "Circuit resonance energy: a key quantity that links energetic and magnetic criteria of aromaticity.," *J. Am. Chem. Soc.*, vol. 128, pp. 2873–2879, 2006.

[50] J. Kruszewski and T. Krygowski, "Definition of aromaticity basing on the harmonic oscillator model," *Tetrahedron Lett.*, vol. 13, pp. 3839–3842, 1972.

[51] T. Krygowski, "Crystallographic studies of inter- and intramolecular interactions reflected in aromatic character of .pi.-electron systems," *J. Chem. Inf. Comput. Sci.*, vol. 33, pp. 70–78, 1993.

[52] W. Hehre, R. McIver, J. Pople, and P. Schleyer, "Alkyl Substituent effects on the stability of protonated benzene," *J. Am. Chem. Soc.*, vol. 6901, pp. 7162–7163, 1974.

[53] P. Lazzeretti, "Assessment of aromaticity via molecular response properties," *Phys. Chem. Chem. Phys.*, vol. 6, pp. 217–223, 2004.

[54] J. Poater, I. Garcia-Cruz, F. Illas, and M. Sola, "Discrepancy between common local aromaticity measures in a series of carbazole derivatives," *Phys. Chem. Chem. Phys.*, vol. 6, pp. 314–318, 2004.

[55] K. Najmidin, A. Kerim, P. Abdirishit, H. Kalam, and T. Tawar, "A comparative study of the aromaticity of pyrrole, furan, thiophene, and their aza-derivatives.," *J. Mol. Modeling*, vol. 19, pp. 3529–3535, 2013.

[56] M. Alonso and B. Herradón, "A universal scale of aromaticity for π-organic compounds," *J. Comput. Chem.*, vol. 31, pp. 917–928, 2010.

[57] K. Kimura, S. Katsumata, Y. Achiba, T. Yamazaki, and S. Iwata, *Handbook of HeI*

Photoelectron Spectra of Fundamental Organic Molecules. New York: Halsted Press, 1981.

[58] P. Linstrom and W. Mallard, *NIST Chemistry WebBook, NIST Standard Reference Database Number 69*. Gaithersburg MD, 20899: National Institute of Standards and Technology, retrieved April 26, 2015. http://webbook.nist.gov.

[59] M. Spanner and S. Patchkovskii, "One-electron ionization of multielectron systems in strong nonresonant laser fields," *Phys. Rev. A*, vol. 80, pp. 63411–63421, 2009.

[60] S. Hankin, D. Villeneuve, P. Corkum, and D. Rayner, "Intense-field laser ionization rates in atoms and molecules," *Phys. Rev. A*, vol. 64, pp. 13405–13416, 2001.

[61] M. DeWitt and R. Levis

[62] J. Eland, "Photoelectron spectra of conjugated hydrocarbons and heteromolecules," *Int. J. Mass Spectrom. Ion Phys.*, vol. 2, pp. 471 – 484, 1969.

[63] K. Horner and P. Karadakov, "Chemical bonding and aromaticity in furan, pyrrole, and thiophene: a magnetic shielding study.," *J. Org. Chem.*, vol. 78, pp. 8037–43, 2013.

[64] S. Pierrefixe and F. Bickelhaupt, "Aromaticity: Molecular-orbital picture of an intuitive concept," *Chem. Eur. J.*, vol. 13, pp. 6321–6328, 2007.

[65] J. Dela Cruz, V. Lozovoy, and M. Dantus, "Quantitative mass spectrometric identification of isomers applying coherent laser control," *J. Phys. Chem. A*, vol. 109, pp. 8447–8450, 2005.

[66] G. Urbasch, H. Breunig, and K. Weitzel, "Distinction of ortho- and para-xylene by femtosecond-laser mass spectrometry," *ChemPhysChem*, vol. 8, pp. 2185–2188, 2007.

[67] M. Suresh, J. McKenna, B. Srigengan, I. Williams, E. English, S. Stebbings, W. Bryan, W. Newell, E. Divall, C. Hooker, and A. Langley, "Multiple ionization of ions and atoms by intense ultrafast laser pulses," *Nucl. Instr. Meth. in Phys. Res. B*, vol. 235, pp. 216 – 220, 2005.

[68] M. Murakami, M. Tanaka, T. Yatsuhashi, and N. Nakashima, "Enhancement of anthracene fragmentation by circularly polarized intense femtosecond laser pulse," *J. Chem. Phys.*, vol. 126, pp. 104304–104307, 2007.

[69] M. C. H. Wong, J.-P. Brichta, M. Spanner, S. Patchkovskii, and V. R. Bhardwaj, "High-harmonic spectroscopy of molecular isomers," *Phys. Rev. A*, vol. 84, pp. 51403–51406, 2011.

[70] A.-T. Le, R. R. Lucchese, and C. D. Lin, "High-order-harmonic generation from molecular isomers with midinfrared intense laser pulses," *Phys. Rev. A*, vol. 88, pp. 21402–21406, 2013.

[71] M. J. Frisch, G. W. Trucks, H. B. Schlegel, G. E. Scuseria, M. A. Robb, J. R. Cheeseman, J. A. Montgomery, Jr., T. Vreven, K. N. Kudin, J. C. Burant, J. M. Millam, S. S. Iyengar, J. Tomasi, V. Barone, B. Mennucci, M. Cossi, G. Scalmani, N. Rega, G. A. Petersson, H. Nakatsuji, M. Hada, M. Ehara, K. Toyota, R. Fukuda, J. Hasegawa, M. Ishida, T. Nakajima, Y. Honda, O. Kitao, H. Nakai, M. Klene, X. Li, J. E. Knox, H. P. Hratchian, J. B. Cross, V. Bakken, C. Adamo, J. Jaramillo,

R. Gomperts, R. E. Stratmann, O. Yazyev, A. J. Austin, R. Cammi, C. Pomelli, J. W. Ochterski, P. Y. Ayala, K. Morokuma, G. A. Voth, P. Salvador, J. J. Dannenberg, V. G. Zakrzewski, S. Dapprich, A. D. Daniels, M. C. Strain, O. Farkas, D. K. Malick, A. D. Rabuck, K. Raghavachari, J. B. Foresman, J. V. Ortiz, Q. Cui, A. G. Baboul, S. Clifford, J. Cioslowski, B. B. Stefanov, G. Liu, A. Liashenko, P. Piskorz, I. Komaromi, R. L. Martin, D. J. Fox, T. Keith, M. A. Al-Laham, C. Y. Peng, A. Nanayakkara, M. Challacombe, P. M. W. Gill, B. Johnson, W. Chen, M. W. Wong, C. Gonzalez, and J. A. Pople, "Gaussian 03, Revision C.02." Gaussian, Inc., Wallingford, CT, 2004.

[72] M. Lewenstein, P. Balcou, M. Y. Ivanov, A. L'Huillier, and P. B. Corkum, "Theory of high-harmonic generation by low-frequency laser fields," *Phys. Rev. A*, vol. 49, pp. 2117–2132, 1994.

[73] H. Li, D. Ray, S. De, I. Znakovskaya, W. Cao, G. Laurent, Z. Wang, M. F. Kling, A. T. Le, and C. L. Cocke, "Orientation dependence of the ionization of co and no in an intense femtosecond two-color laser field," *Phys. Rev. A*, vol. 84, pp. 43429–43435, 2011.

[74] L. Holmegaard, J. Hansen, L. Kalhøj, S. Kragh, H. Stapelfeldt, F. Filsinger, J. Küpper, G. Meijer, D. Dimitrovski, M. Abu-Samha, *et al.*, "Photoelectron angular distributions from strong-field ionization of oriented molecules," *Nat. Phys.*, vol. 6, pp. 428–432, 2010.

[75] A.-T. Le, R. R. Lucchese, S. Tonzani, T. Morishita, and C. D. Lin, "Quantitative

rescattering theory for high-order harmonic generation from molecules," *Phys. Rev. A*, vol. 80, pp. 13401–13423, 2009.

[76] T. Morishita, A.-T. Le, Z. Chen, and C. D. Lin, "Accurate retrieval of structural information from laser-induced photoelectron and high-order harmonic spectra by few-cycle laser pulses," *Phys. Rev. Lett.*, vol. 100, pp. 13903–13906, 2008.

[77] F. A. Gianturco, R. R. Lucchese, and N. Sanna, "Calculation of low-energy elastic cross sections for electron-cf_4 scattering," *J. Chem. Phys.*, vol. 100, pp. 6464 – 6471, 1994.

[78] A. Natalense and R. Lucchese, "Cross section and asymmetry parameter calculation for sulfur 1s photoionization of sf6," *J. Chem. Phys.*, vol. 111, pp. 5344 – 5348, 1999.

[79] A.-T. Le, R. R. Lucchese, and C. D. Lin, "Quantitative rescattering theory of high-order harmonic generation for polyatomic molecules," *Phys. Rev. A*, vol. 87, pp. 63406–63414, 2013.

[80] R. Freeman and P. Bucksbaum, "Investigations of above-threshold ionization using subpicosecond laser pulses," *J. Phys. B*, vol. 24, pp. 325–347, 1991.

[81] B. Sheehy and L. DiMauro, "Atomic and molecular dynamics in intense optical fields," *Annu. Rev. Phys. Chem.*, vol. 47, pp. 463–494, 1996.

[82] V. Popov, "Tunnel and multiphoton ionization of atoms and ions in a strong laser field (keldysh theory)," *Phy. Usp.*, vol. 47, pp. 855–885, 2004.

[83] J. Muth-Böhm, A. Becker, and F. Faisal, "Suppressed molecular ionization for a class

of diatomics in intense femtosecond laser fields," *Phys. Rev. Lett.*, vol. 85, pp. 2280–2283, 2000.

[84] M. Meckel, A. Staudte, S. Patchkovskii, D. Villeneuve, P. Corkum, R. Dörner, and M. Spanner, "Signatures of the continuum electron phase in molecular strong-field photoelectron holography," *Nat. Phys.*, vol. 10, pp. 594–600, 2014.

[85] T. Brabec, M. Côté, P. Boulanger, and L. Ramunno, "Theory of tunnel ionization in complex systems," *Phys. Rev. Lett.*, vol. 95, pp. 073001–073004, 2005.

[86] L. Holmegaard, J. Hansen, L. Kalhøj, S. Kragh, H. Stapelfeldt, F. Filsinger, J. Küpper, G. Meijer, D. Dimitrovski, M. Abu-samha, C. Martiny, and L. Madsen, "Photoelectron angular distributions from strong-field ionization of oriented molecules," *Nat. Phys.*, vol. 6, pp. 428–432, 2010.

[87] I. Petersen, J. Henkel, and M. Lein, "Signatures of molecular orbital structure in lateral electron momentum distributions from strong-field ionization," *Phys. Rev. Lett.*, vol. 114, pp. 103004–103008, Mar 2015.

[88] D. Dimitrovski, J. Maurer, H. Stapelfeldt, and L. B. Madsen, "Strong-field ionization of three-dimensionally aligned naphthalene molecules: orbital modification and imprints of orbital nodal planes," *J. Phys. B*, vol. 48, pp. 245601–245608, 2015.

[89] I. Thomann, R. Lock, V. Sharma, E. Gagnon, S. Pratt, H. Kapteyn, M. Murnane, and W. Li, "Direct measurement of the angular dependence of the single-photon ionization of aligned n_2 and co_2," *J. Phys. Chem. A*, vol. 112, pp. 9382–9386, 2008.

[90] J. Mikosch, A. Boguslavskiy, I. Wilkinson, M. Spanner, S. Patchkovskii, and A. Stolow, "Channel-and angle-resolved above threshold ionization in the molecular frame," *Phys. Rev. Lett.*, vol. 110, pp. 23004–23007, 2013.

[91] K. S. Budil, P. Salières, A. L'Huillier, T. Ditmire, and M. D. Perry, "Influence of ellipticity on harmonic generation," *Phys. Rev. A*, vol. 48, pp. R3437–R3440, Nov 1993.

[92] P. Dietrich, N. H. Burnett, M. Ivanov, and P. B. Corkum, "High-harmonic generation and correlated two-electron multiphoton ionization with elliptically polarized light," *Phys. Rev. A*, vol. 50, pp. R3585–R3588, 1994.

[93] A. Ferr *et al.*, "Multi-channel electronic and vibrational dynamics in polyatomic resonant high-order harmonic generation," *Nat. Commun.*, vol. 6, pp. 5952–5961, 2015.

[94] M. Spanner and S. Patchkovskii, "Molecular strong field ionization and high harmonic generation: A selection of computational illustrations," *Chem. Phys.*, vol. 414, pp. 10 – 19, 2013.

[95] A. F. Alharbi, A. E. Boguslavskiy, N. Thiré, B. E. Schmidt, F. Légaré, T. Brabec, M. Spanner, and V. R. Bhardwaj, "Sensitivity of high-order-harmonic generation to aromaticity," *Phys. Rev. A*, vol. 92, pp. 41801–41806, 2015.

[96] A. Bergner, M. Dolg, W. Küchle, H. Stoll, and H. Preuß, "Ab-initio energy-adjusted pseudopotentials for elements of groups," *Mol. Phys.*, vol. 80, pp. 1431–1441, 1993.

[97] L. A. Carreira, R. O. Carter, and J. R. Durig, "Raman spectra of gases. vii. barriers to planarity in 1,4- and 1,3-cyclohexadiene," *J. Chem. Phys.*, vol. 59, pp. 812–816, 1973.

[98] W. Kohn and L. J. Sham, "Self-consistent equations including exchange and correlation effects," *Phys. Rev.*, vol. 140, pp. A1133–A1138, 1965.

[99] E. V. Anslyn and D. A. Dougherty, *Modern physical organic chemistry.* USA: University Science, 2006.

[100] N. Kuthirummal and P. Weber, "Rydberg states: sensitive probes of molecular structure," *Chem. Phys. Lett.*, vol. 378, pp. 647 – 653, 2003.

[101] H. Harada, S. Shimizu, T. Yatsuhashi, S. Sakabe, Y. Izawa, and N. Nakashima, "A key factor in parent and fragment ion formation on irradiation with an intense femtosecond laser pulse," *Chem. Phys. Lett.*, vol. 342, pp. 563 – 570, 2001.

[102] E. Fowe and A. Bandrauk, "Nonlinear time-dependent density-functional-theory study of ionization and harmonic generation in co_2 by ultrashort intense laser pulses: Orientational effects," *Phys. Rev. A*, vol. 81, pp. 23411–23418, 2010.

[103] C. Hutchison, S. Houver, N. Lin, D. Hoffmann, F. McGrath, T. Siegel, D. Austin, A. Zar, P. Salires, and J. Marangos, "Electron trajectory control of odd and even order harmonics in high harmonic generation using an orthogonally polarised second harmonic field," *J. Mod. Opt.*, vol. 61, pp. 608–614, 2014.

[104] C. Ni, C. Tseng, M. Lin, and Y. Dyakov, "Photodissociation dynamics of small

aromatic molecules studied by multimass ion imaging," *J. of Phys. Chem. B*, vol. 111, pp. 12631–12642, 2007.

[105] S. Salzmann, M. Kleinschmidt, J. Tatchen, R. Weinkauf, and C. Marian, "Excited states of thiophene: ring opening as deactivation mechanism," *Phys. Chem. Chem. Phys.*, vol. 10, pp. 380–392, 2008.

[106] Y. Liu, B. Tang, H. Shen, S. Zhang, and B. Zhang, "Probing ultrafast internal conversion of o-xylene via femtosecond time-resolved photoelectron imaging," *Opt. Express*, vol. 18, pp. 5791–5801, 2010.

[107] J. Zhou, J. Peatross, M. M. Murnane, H. C. Kapteyn, and I. P. Christov, "Enhanced high-harmonic generation using 25 fs laser pulses," *Phys. Rev. Lett.*, vol. 76, pp. 752–755, 1996.

[108] J. Higuet, H. Ruf, N. Thiré, R. Cireasa, E. Constant, E. Cormier, D. Descamps, E. Mével, S. Petit, B. Pons, Y. Mairesse, and B. Fabre, "High-order harmonic spectroscopy of the cooper minimum in argon: Experimental and theoretical study," *Phys. Rev. A*, vol. 83, pp. 53401–53412, 2011.

[109] A. Shiner, B. Schmidt, C. Trallero-Herrero, P. Corkum, J. Kieffer, F. Légaré, and D. Villeneuve, "Observation of Cooper minimum in krypton using high harmonic spectroscopy," *J. Phys. B*, vol. 45, no. 7, pp. 74010–74013, 2012.

[110] J. W. Cooper, "Photoionization from outer atomic subshells. a model study," *Phys. Rev.*, vol. 128, pp. 681–693, 1962.

[111] T. Carlson, M. Krause, F. Grimm, P. Keller, and J. Taylor, "Angle-resolved photoelectron spectroscopy of ccl_4: the cooper minimum in molecules," *J. Chem. Phys.*, vol. 77, pp. 5340–5347, 1982.

[112] T. Carlson, M. Krause, A. Fahlman, P. Keller, J. Taylor, T. Whitley, and F. Grimm, "Angle-resolved photoelectron spectroscopy of hcl from a photon energy of 16 to 80 ev," *J. Chem. Phys.*, vol. 79, pp. 2157–2162, 1983.

[113] T. A. Carlson, M. O. Krause, W. A. Svensson, P. Gerard, F. A. Grimm, T. A. Whitley, and B. P. Pullen, "Photoelectron dynamics of the cooper minimum in free molecules," *Zeitschrift für Physik D*, vol. 2, pp. 309–318, 1986.

[114] M. Schmidt, K. Baldridge, J. Boatz, S. Elbert, M. Gordon, J. Jensen, S. Koseki, N. Matsunaga, K. Nguyen, S. Su, T. Windus, M. Dupuis, and J. Montgomery, "General atomic and molecular electronic structure system," *J. Comput. Chem.*, vol. 14, pp. 1347–1363, 1993.

[115] L. Mei, M. Chuaqui, C. Mathers, J. Ying, and K. Leung, "Experimental momentum-space orbital density study of valence-shell electronic structure and many-body effects of trans-dichloroethylene by symmetric noncoplanar (e, 2e) spectroscopy," *Chem. Phys.*, vol. 188, pp. 347 – 365, 1994.